Characterisation of III-Nitrides in The Scanning Electron Microscope

Aeshah Alasmari
University of Strathclyde

A PhD thesis submitted to
the Department of Physics
University of Strathclyde
for the degree of
Doctor of Philosophy
February 28, 2021

Declaration of author’s right

This thesis is the result of the author's original research. It has been composed by the author and has not been previously submitted for examination which has led to the award of a degree.

The copyright of this thesis belongs to the author under the terms of the United Kingdom Copyright Acts as qualified by University of Strathclyde Regulation 3.50. Due acknowledgement must always be made of the use of any material contained in, or derived from, this thesis.

Signed: Date:

Abstract

This thesis presents research on the characterisation of group III-nitrides using scanning electron microscope (SEM) techniques. In particular structural and morphological properties were investigated by electron channelling contrast imaging (ECCI) and electron backscatter diffraction (EBSD). ECCI reveals threading dislocations (TDs), sub-grains, atomic steps and step bunches in the material under study, while EBSD provides quantitative data on sub-grain misorientation.

ECCI was also correlated with atomic force microscopy (AFM) to reveal and identify TDs in an epitaxially laterally overgrown GaN film, where the pattern for overgrowth comprised of stripes parallel to the GaN $[1\bar{1}00]$ direction. ECCI revealed both vertically threading and inclined dislocations. Each dislocation was identified, using complementary information provided by AFM and ECCI, as either *a*-type or *c*/(*a*+*c*)-type dislocations.

To extend ECCI to the study of insulating samples, ECCI micrographs were acquired in a variable pressure scanning electron microscope (VP-SEM) at pressures ranging from 0.3 mbar to 0.8 mbar using gaseous secondary electron detectors (GSEDs). ECCI micrographs are produced by detecting a gas-amplified secondary electron signal, indicating that the intensity of the detected secondary electrons is modulated as a result of diffraction of the incident electron beam. The influence of pressure, detector bias, sample tilt and working distance on the quality of ECCI micrographs were investigated.

Aluminum nitride (AlN) samples grown on nano-patterned (nano-pillars) sapphire substrate (nPSS) were investigated. The miscut of the substrate and the size of the nano-pillars were shown to influence the surface morphology and TD density. The analysis of these AlN/nPSS samples showed a dependence of the density of step bunches with the density of TDs, the higher the density of step bunches, the lower the TD density. EBSD was used to measure the misorientations of sub-grains in the AlN/nPSS and the misorientation was observed to increase as the density of TDs increased.

Acknowledgments

I would like to express my gratitude to all the people who helped and guided me throughout my PhD. First to my supervisor, Dr. Carol Trager-Cowan, for her helpful feedback and direction during this project. I could not have finished my research without her motivation, support, patience and knowledge. I would also like to thank Prof. Robert Martin, my second supervisor, for his effective direction and instruction. I am thankful to Dr. Naresh Kumar for his guidance in the lab and his help explaining tricky concepts. Thank you to Dr. Jochen Bruckbauer for allowing me to use his pre-tilted stage for EBSD and CL maps. Dr. Paul Edwards helped me in the microscope and was always available to solve technical problems. Also, thank you to Dr. Gunnar Kusch for help in obtaining the EBSD map and ECCI micrographs for sample A in chapter 6. I am grateful for the contributions of Dr. Tom O'Hanlon and Dr. Rachel Oliver who provided me with the AFM data in Chapter 4 beside the sample used in this chapter. An extreme thankful to Ferdinand-Braun-Institut, Leibniz-Institut fuer Hoechstfrequenztechnik (FBH) from Berlin and University of Bath for the great collaboration for provided me with AlN thin films for chapter 6 and needed information about samples. I appreciate the support of Dr. Aimo Winkelmann for his help with the EBSD pattern matching in Chapter 6, Dr. Gergely Ferenczi for teaching me how to use the MTEX software , Ryan McDermott for providing me with the normalised graphs in Chapter 6 and Kieran Hiller for also provide me with the EBSD map in chapter 6. I would also like to give sincere thanks to my friends during this PhD journey Dr. Brooke Matat Jablon and Catherine Brasser. Thank you for being great mates.

I am indebted to my sponsor, the University of Bisha, for their financial support. Thank you for giving me the opportunity to study at such a great university and acquire a depth of experimental knowledge. The University of Bisha assists and encourages their employees to complete their higher education around the world. This thesis would not have come to fruition without their continuing support.

I am extremely grateful to my family in Saudi Arabia for their care. I wish that my father could be here on this day to share this great achievement with me. For a long

time he dreamt and prayed for this goal. As happy as I am to finish this project, I feel that something is missing without him by my side to see it's completion. To my mum, you gave me strength and hope when I was ready to give up. Thank you for all your prayers and love since the day I was born. To my siblings; Noura, Saad, Thanwa, Mohammed, Nasser and Ali, you are the best cheerleaders. You cared and stood by me throughout my years of higher education and this support means a lot to me.

My little family deserves an acknowledgment as well. My daughters; Lana, Tala and Jori shared each moment with me as I worked to complete this project. Thank you for understanding that these last few months were a critical phase in my studies and for tolerating the hardships over this last year, in particular staying in a foreign country with me during this ongoing COVID-19 pandemic. Thank you, my lovely angels, for being supportive helpers. Thank you to my soul mate Ahmad Alamri who helped me reach this moment. This success is yours too. I would not have been able to realize this accomplishment without your support. Thank you for your patience, care and, prayers. You are the shoulder that I lean on for support over and over again.

List of Publications

1. **Advances in electron channelling contrast imaging and electron backscatter diffraction for imaging and analysis of structural defects in the scanning electron microscope**

   C. Trager-Cowan; **A. Alasmari**; W. Avis; J. Bruckbauer; P. R. Edwards; B. Hourahine;S. Kraeusel; G. Kusch; R. Johnston; G. Naresh-Kumar; R. W. Martin,1 M. Nouf-Allehiani; E. Pascal; L. Spasevski; D. Thomson; S. Vespucci; P. J. Parbrook; M. D. Smith; J. Enslin; F. Mehnke; M. Kneissl; C. Kuhn; T. Wernicke; S. Hagedorn; A. Knsuer; V. Kueller;S. Walde; M. Weyers; P.-M. Coulon; P. A. Shields; Y. Zhang; L. Jiu; Y. Gong; R. M. Smith; T. Wang; and A. Winkelmann.

   In: Photonics Research, Vol. 7, No. 11 , 361722, 2019.

2. **Structural and luminescence imaging and characterisation of semiconductors in the scanning electron microscope**

   C. Trager-Cowan; **A. Alasmari**; W. Avis; J. Bruckbauer; P. R. Edwards; G. Ferenczi; B. Hourahine; A. Kotzai; S. Kraeusel; G. Kusch; R. W. Martin; R. McDermott; G. Naresh-Kumar; M. Nouf-Allehiani; E. Pascal; D. Thomson; S. Vespucci; M. D. Smith; P. J. Parbrook; J. Enslin; F. Mehnke; C. Kuhn; T. Wernicke; M. Kneissl; S. Hagedorn; A. Knauer; S. Walde; M. Weyers; P.-M. Coulon; P. A. Shields; J. Bai; Y. Gong; L. Jiu; Y Zhang; R. M. Smith; T. Wang and A. Winkelmann.

   In: Semiconductor Science and Technology, Vol. 35, No. 11, 054001, 2020.

3. **Metrology of crystal defects through intensity variations in secondary electrons from the diffraction of primary electrons in a scanning electron microscope**

   G. Naresh-Kumar; **A. Alasmari**; G. Kusch; P. R. Edwards; R. W. Martin; K.P. Mingard and C. Trager-Cowan.

   In: Ultramicroscopy, Vol. 213, No. 9, 112977, 2020.

4. **AlN overgrowth of nano-pillar-patterned sapphire with different offcut angle by metalorganic vapor phase epitaxy**

   S. Walde; S. Hagedorn; P.-M. Coulon; A. Mogilatenko; C. Netzel; J. Weinrich; N. Susilo; E. Ziffer; L. Matiwe; C. Hartmann; G. Kusch; **A. Alasmari**; G. Naresh-Kumar; C. Trager-Cowan; T. Wernicke; T. Straubinger; M. Bickermann; R.W. Martin; P.A. Shields; M. Kneissl and M. Weyers.

   In: Journal of Crystal Growth, Vol. 531, No. 7 125343, 2020.

5. **Visualization of defects in nitride semiconductors by electron channeling (Conference Presentation)**

   C. Trager-Cowan; **A. Alasmari**; W. Avis; J. Bruckbauer; P. R. Edwards; B. Hourahine; A. Kotzai; G. Kusch; R. W. Martin; R. McDermott; G. Naresh-Kumar; M. Nouf-Allehiani; E. Pascal; D. Thomson; D. Waters; P. J. Parbrook; A. Vilalta-Clemente; A. J. Wilkinson: K.P. Mingard and A. Winkelmann.

   In: Conference: Gallium Nitride Materials and Devices XV, 2020.

6. **Coincident Electron Channelling Contrast Imaging and Atomic Force Microscopy of threading dislocations in Epitaxial Lateral Overgrown GaN**

   Aeshah Alasmari; T. O'Hanlon; G. Naresh-Kumar; R. Oliver and C. Trager- Cowan.

   Manuscript in preparation

7. **Characterization of AlN/nPSS thin films by SEM**

   Aeshah Alasmari; G. Naresh-Kumar; G. Kusch; S. Hagedorn; P.-M. Coulon; A. Mogilatenko; C. Netzel; J. Weinrich; N. Susilo; E. Ziffer; L. Matiwe; C. Hartmann;; J. Bruckbauer; P. R. Edwards; B. Hourahine; R. W. Martin; R. McDermott; S. Walde; A. Winkelmann and C. Trager-Cowan.

   Manuscript in preparation

List of Abbreviations

AFM	Atomic force microscope
B-W	Black-white
BSE	Backscatter electron
CL	Cathodoluminescence
EBSD	Electron backscatter diffraction
EBSP	Electron backscatter pattern
ECCI	Electron channeling contrast imaging
ECP	Electron channeling contrast pattern
ELOG	Epitaxial lateral overgrowth
ESE	Environmental secondary electron
FSD	Forescatter detector
GROD	Grain reference orientation deviation
GND	Geometrically necessary dislocation
GSED	Gaseous secondary electron detector
HVPE	Hydride vapour phase epitaxy
LFD	Large field detector
MBE	Molecular-beam epitaxy
MOVPE	Metalorganic vapour-phase epitaxy
nPSS	Nano patterned sapphire substrate
PE	Primary electron beam
PSS	Patterned sapphire substrates
PLA	Pressure limited aperture
SE	Secondary electron
SEM	Scanning electron microscope
TEM	Transmission electron microscope
TD	Threading dislocation

WD	Working distance
XRD	X-ray diffraction

Table of Contents

Abstract ***2***

Acknowledgments ***3***

List of Publications ***5***

List of Abbreviations ***7***

1* Introduction** ***11

2* Background** ***15

2.1 Properties of III-nitrides: 15
2.1.1 The crystal structure: 16
2.1.2 The optical properties: 18
2.1.3 Applications of III-nitrides: 19

2.2 Growth methods for III-nitrides: 20
2.2.1 Molecular beam epitaxy (MBE): 20
2.2.2 Metalorganic vapour phase epitaxy (MOVPE): 21
2.2.3 Hydride vapour phase epitaxy (HVPE): 22
2.2.4 Substrates 23

2.3 Defects in III-nitrides: 26
2.3.1 Point defects 26
2.3.2 Line defect: threading dislocations (TDs) 27
2.3.3 Surface defects 28

2.4 Reduction mechanisms of dislocations in III-nitrides 30
2.4.1 Epitaxial lateral overgrowth (ELOG) 31
2.4.2 Nano-patterned sapphire substrates (NPSS) 33
2.4.3 The miscut substrate 35

2.5 Characterisation of structural properties 37

3* Methodology** ***43

3.1 The principle and operation of scanning electron microscopy (SEM) 43
3.1.1 Electron-sample interaction 46
3.1.2 The generated signals 48
3.1.3 The detection system in a conventional scanning electron microscope 50

3.2 Electron channelling contrast imaging (ECCI) 52

3.3 Electron backscattered diffraction (EBSD) 62

3.4 Atomic force microscope (AFM) 67

4* Coincident ECCI and AFM of threading dislocations in ELOG GaN** ***73

4.1 Introduction: 73

4.2 The sample fabrication: 74

4.3 The experimental methods 75

4.4 Results and discussion 76

4.4.1 The AFM result ... 76
4.4.2 The ECCI result ... 77

4.5 Coincident ECCI and AFM measurements ... 81

4.6 Summary ... 89

5 ECCI in the gaseous environment for characterization of insulating samples 90

5.1 Introduction: ... 90

5.2 The principle of the variable pressure SEM (VP-SEM) ... 92

5.3 ECCI technique as a new approach in VP-SEM ... 99

5.4 The effective parameters on ECC imaging in VP-SEM ... 102
5.4.1 Effect of detector bias ... 102
5.4.2 Effect of gas pressure ... 105
5.4.3 Effect of scan rate ... 107
5.4.4 Effect of working distance ... 108
5.4.5 Effect of sample geometry ... 111

5.5 Summary: ... 112

6 Characterization of AlN/nPSS thin films by SEM 113

6.1 Introduction ... 113

6.2 Sample fabrication ... 115

6.3 The experimental methods ... 117

6.4 The influence of substrate miscut on AlN/nPSS thin films epilayer ... 118
6.4.1 The ECCI results ... 118
6.4.2 Identification of TDs ... 122
6.4.3 The impact of step bunches on TDD ... 123

6.5 The influence of pattern dimension on AlN/nPSS thin films epilayer ... 124

6.6 Measurement of misorientations in AlN/ nPSS thin films using EBSD ... 127

6.7 Summary ... 135

7 Conclusions and future work 137

7.1 Techniques and samples: ... 137

7.2 Coincident ECCI and AFM of threading dislocations in ELOG GaN ... 138

7.3 ECCI in the gaseous environment for characterization of insulating samples ... 138

7.4 Characterisation of AlN/nPSS thin films by SEM ... 139

7.5 Future work: ... 140

List of figures 142

List of Tables 147

References 148

Chapter 1

Introduction

The most prominent event of 2020 has been the COVID-19 pandemic. This virus has led the whole world to focus on sterilization and handwashing. Handwashing, a potentially life-saving practice, is a privilege in countries without access to clean water sources (tap water or safe well water). In places that lack clean water, hand washing is not a priority. In developing countries, home water filters can be placed at the water source to ensure safe drinking water.

According to the World Health Organisation (WHO) [1], as of 2019, there were two billion people drinking contaminated water by faeces and 435 million people using water from unprotected wells, surface water and spring sources. Several potentially life-threatening diseases are transmitted by contaminated water including diarrhoea, cholera, dysentery, typhoid, and polio. Each year around 485,000 people die from cases of diarrhoea that are linked to contaminated water sources. The lack of clean water is leading to reinfection from diarrhoea related illnesses. During the COVID-19 pandemic, failure to wash hands has led to the spread of the virus. In affected countries this puts health care providers at risk of infection by these diseases from their patients in the absence of hygiene services. Around 15% of patients get infected during their staying at the hospital. [1, 2]

Climate change and the related growth in worldwide population means that most of the earth's population will live in water stressed regions by 2025. [1] Finding alternative strategies for recycling waste water with adequate sterilization will be crucial to the health of billions of people. This water can then be used for irrigation which will increase food production. This would mark an improvement to the current situation where countries are using wastewater for irrigation. In some countries, agricultural land irrigated by waster water represents 7% of irrigated land. [1]

The most common technique used for water purification is exposure to UV light which is effective at destroying the DNA or RNA of the most common bacteria found in water by making them unable to reproduce. [3] A dose of UV radiation as low as 40 mJ cm^{-2} is enough to inactivate most bacteria, spores and viruses. [3]

A conventional source of UV light is the mercury lamp which today is recognized as unfriendly to the environment as it is energy consuming and contains mercury gas, a known toxic gas. It emits UV light at a wavelength of 254 nm. While mercury lamps are known to kill pathogens, there are many disadvantages associated with their use, including their size, fragility, start-up time, emission wavelengths and toxic components. An alternative source for water sterilization is UV-LEDs based on III-nitrides. There are numerous advantages to using group-III-nitride-based UV LEDs which operate at moderate dc voltages, have long lifetimes and are environmentally friendly. In addition, their emission wavelength can be engineered by varying the material composition. UV LEDs are used in a number of applications that require UV curing, like coatings, inks, adhesives, composites and stereolithography while ultraviolet-C (UV–C) light emitting diodes (LEDs) are used for water disinfection. The advantage of UV-LEDs, in comparison to traditional disinfection sources, is a reduction in energy consumption and heat generation.

UV-LEDs are also used for skin treatments and by dentists to disinfect their tools.

Despite these advantages, UV-LEDs still suffer a numbers of drawbacks. UV-LEDs grown on GaN/sapphire [4] or AlN/sapphire templates have a high density of threading dislocations due to lattice mismatch between the substrate and epilayer (GaN or AlN). Those defects act as non-radiative recombination centres which negatively affect the internal and external efficiencies of UV-LEDs and degrade their output power. These defects can be examined in AlN using scanning electron microscope techniques such as electron channelling contrast imaging ECCI and electron backscattered diffraction EBSD.

Researchers in academia and industry are trying to overcome these limitations and enhance the properties of UV-LEDs. One direction used to improve the properties is revising growth techniques to ensure a high quality of material with low TDs density. Another direction is the improvement and development of post-fabrication

investigative techniques. This thesis is my contribution to the field of III-nitride characterisation for semiconductors destined for use in deep UV-LEDs.

In the present thesis, the scanning electron microscope (SEM) techniques of electron channelling contrast imaging (ECCI) and electron backscattered diffraction (EBSD) are used to investigate the structural properties of a range of UV-emitting nitrides (GaN and AlN). UV materials present challenges in that their wide bandgap means that they can be electrically insulating and thus charge under the electron beam. Future chapters will reveal the development of new methodologies to mitigate charging of insulating samples.

Chapter 1 is the introduction chapter that demonstrate the motivations behind this thesis. In addition it provides the overview of all chapters that in this thesis.

Chapter 2, provides an overview on III-nitride materials, summarising their structural and optical properties and outlining their applications. The main growth methods are introduced as are the substrates utilised to produce heteroepitaxial III-nitride thin films. Structural defects which can exist in crystalline materials are described, in particular threading dislocations (TDs). These are discussed further throughout this thesis. The advanced growth methods used to reduce TD density are also reviewed. Finally, the standard characterisation techniques commonly used to study the structural properties and defects in crystalline materials, such as transmission electron microscopy (TEM), Cathodoluminescence spectroscopy (CL), and X-ray diffraction are briefly presented.

Chapter 3 provides an overview of the two microscopy techniques, atomic force microscopy (AFM) and scanning electron microscopy (SEM) used to investigate III-nitrides in this thesis. The SEM techniques of electron channelling contrast imaging (ECCI) and electron backscatter diffraction (EBSD) are also introduced as they are used to study the structural properties of the materials investigated.

In chapter 4, I report the study of a GaN sample grown using the epitaxial lateral overgrowth technique. In this chapter I combine two major characterization techniques, namely atomic force microscopy AFM and electron channelling contrast imaging ECCI to investigate the material and explore the behaviour of defects.

In chapter 5, I describe and demonstrate the use of ECCI in a gaseous environment and the use of a gaseous detector, off-axis gaseous secondary electron detector (off-axis GSED), to acquired ECCI micrographs. Imaging in a gaseous environment radically

reduces charging of insulating samples and has opened up the use of ECCI to the characterisation of AlN.

In chapter 6 “Characterization of AlN/nPSS thin films by SEM”, I present results on AlN grown on nano-patterned sapphire substrates (nPSS) and show the influence of the substrate miscut angle on the structural properties (e. g. density of TDs, step bunches density, and mis-orientation angles) of AlN layers. I also discuss the influence of the pattern configuration on the structural properties of AlN samples.

Chapter 7 presents conclusions on this thesis which used electron channelling contrast imaging (ECCI), electron backscatter diffraction (EBSD) and atomic force microscopy (AFM) to study GaN and AlN samples. Research on ELOG GaN showed the ability of ECCI to resolve inclined dislocations. To examine insulating samples such AlN a gaseous secondary detector was used to obtain ECCI micrographs instead of a traditional backscattered detector. This technique was applied to four AlN samples as a proof of concept. Finally, AlN/nPSS thin films were studied. Also, it provides the future experimental work as extension for the present thesis.

Chapter 2

Background

In this chapter I provide an overview on III-nitride materials, summarising their structural and optical properties and outlining their applications. I describe the main growth methods and the substrates utilised to produce heteroepitaxial III-nitride thin films. I introduce the structural defects which can exist in crystalline materials, in particular threading dislocations (TDs) which are the main defects investigated in this thesis. The advanced growth methods used to reduce TD density are also reviewed. Finally, the standard characterisation techniques used in the study of the structural properties and defects in crystalline materials, that is transmission electron microscopy (TEM), Cathodoluminescence (CL), and X-ray diffraction (XRD) are briefly described. The characterisation techniques used in my research, that is the scanning electron microscopy techniques of electron channelling contrast imaging and electron backscatter diffraction; and atomic force microscopy, will be described in detail in the next chapter.

2.1 Properties of III-nitrides:

III-nitrides refers to the compounds which form from elements from group III of the periodic table (Ga, Al, In) and nitrogen to produce InN, GaN and AlN alloys. Their bandgaps cover the spectrum from the ultraviolet region, 6.2 eV (200 nm) for AlN, to the infrared region, 0.7 eV (1771 nm) for InN and thus cover the full visible spectrum. Figure 2.1 illustrates the relationship between the lattice constant and the bandgap energy. Numerous applications require the ternary alloys, for example, AlGaN, InGaN, AlInN, and even the quaternary AlInGaN. Their bandgap energy is tuneable depending upon the composition of In, Ga or Al in the alloy system. [5]

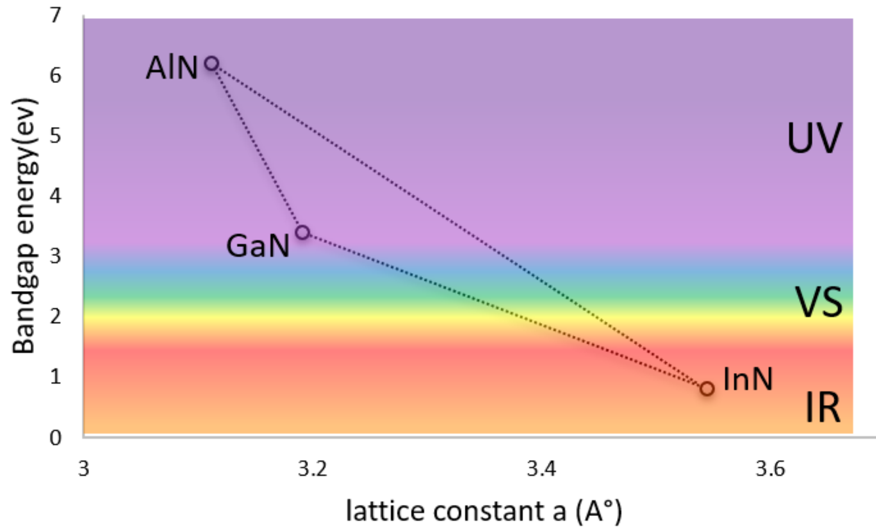

Figure 2. 1: Bandgap energy (E_g) versus lattice constant (a) of wurtzite III-nitrides c ≈1.6 a. [6] ,The figure is adapted from [7, 8]

2.1.1 The crystal structure:

III-nitrides can be formed in two main structures; wurtzite (hexagonal) and zincblende (cubic), however, under high pressure during the growth and the use of a suitable substrate, the rock salt (NaCl) structure can also be achieved. Thermodynamically, the wurtzite structure is the most stable structure for AlN, GaN and InN, while the zincblende is classified as a metastable structure.[9]

In the present work, the wurtzite structure is the main focus. The wurtzite structure is the hexagonal lattice which contains two hexagonal closed pack of elements in group III (red sphere) and N atoms (blue sphere) see figure 2.2.a. Each group III atom is surrounded by four atoms of nitrogen and reciprocally, each nitrogen atom is surrounded by four atoms of the group III atoms. The stacking sequence of the wurtzite structure along *c*- axis is ABAB see figure 2.2.a.

The hexagonal lattice is described by four main axes. Three axes lie in the basal planes a_1, a_2 and a_3 with an angle between them of 120° and the *c* axis is normal to the basal plane and denoted by [0001]. Any point in the lattice can be represented by four indices

[*hkil*] where *hki* are the intercept of the points with the basal planes axes and *l* is the intercept with the *c*-plane. Four main planes are important in the wurtzite III-nitride crystals; *c*-plane (0001), *a*-plane ($11\bar{2}0$), *m*-plane ($1\bar{1}00$) and *r*-plane ($11\bar{2}2$).There are two main lattice constants parameters; *a* and *c*, where *a* is the length of the sides of the hexagon in the basal plane and *c* is the height of the hexagon (see figure 2.2.a). The lattice parameters for GaN and AlN are listed in Table. 2.1.

Due to the strong chemical bond in III-nitrides (covalent bond) they have a high melting point which means that the III-nitride materials have thermal and chemical stability in addition to mechanical strength. [10]

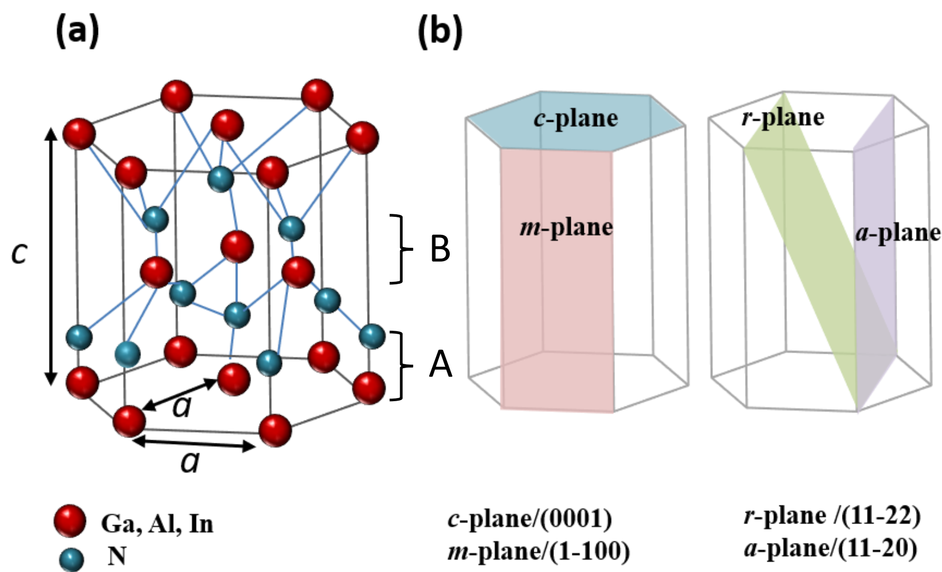

Figure 2. 2: a) The wurtzite structure of AlN, GaN and InN at room temperature adapted from [11], b) Illustrates the planes of the wurtzite crystal *c*-plane (0001), *a*-plane ($11\bar{2}0$), *m*-plane ($1\bar{1}00$) and *r*-plane ($11\bar{2}2$).

2.1.2 The optical properties:

LED lighting (solid-state lighting) now dominates the lighting market, it has created a notable revolution in the lighting market since the beginning of this century. Globally, it achieved 63 billion dollars in 2018 and possibly will be worth around 127 billion dollars by 2023. The direct and wide bandgap makes III-nitrides materials good candidates for optical applications.[12]

Any semiconductor material has two types of charge carriers: electrons and holes. In general, the electrons are located within the conduction band while the holes are located within the valence band. The emission of light in direct bandgap semiconductor materials occurs after direct recombination, when an electron from the conduction band meets a hole from the valence band. In semiconductor materials which contain a low concentration of defects, band to band recombination dominates figure 2.3.a. Electrons and holes can be bound under the electrostatic Coulombic force at room temperature (excitons) and this will lead to radiative recombination see figure 2.3.b. Figure 2.3.c,d,e shows the radiative emission that can be achieved through recombination of electron and holes at donor and acceptors states. In the case of a high density of defects, considerable non-radiative recombination occurs. Figure2.3.f shows the non-radiative recombination through a defect which induces an energy level within the bandgap.[6] The optical properties of III-nitride thin films can be obtained using cathodoluminescence (CL) or photoluminescence (PL) techniques. [5]

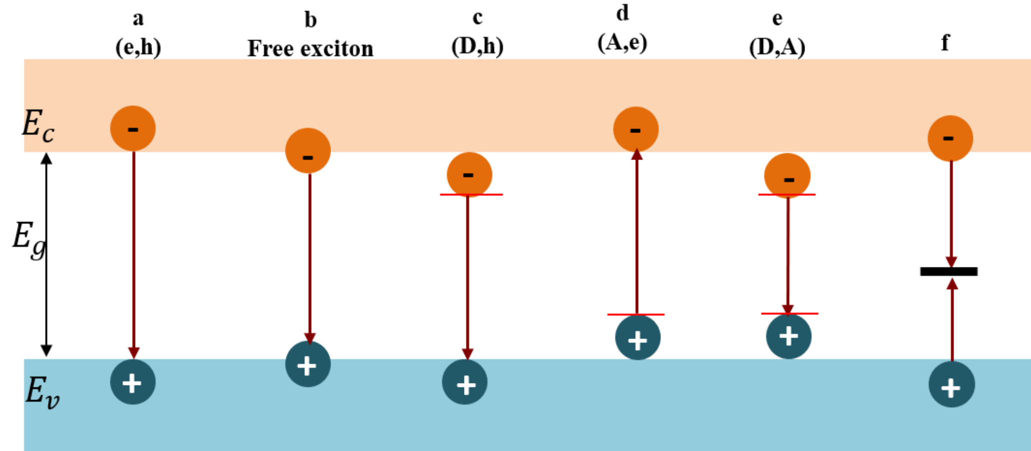

Figure 2. 3: Schematic shows the possible radiative and non-radiative recombination in semiconductor materials. a. free electron-hole, b. free exciton, c. donor-hole, d. acceptor-electron, e. donor-acceptor. f. nonradiative recombination via a defect. Adapted from [6]

2.1.3 Applications of III-nitrides:

As mentioned previously, the large and direct bandgap of III-nitrides makes them the preferable candidate materials for electronic and optoelectronic applications. III-nitrides led a significant revolution in the photonic industry via the production of light-emitting diodes (LEDs), photodiodes, UV detectors, and laser diodes (LDs). Nowadays, III-nitride can be seen widely in traffic lights, automobile lights, illuminated advertisement panels, indicator lights, mobiles, TV screens and in general lighting. Commercially, blue and green LEDs are widely spread.[9] Nitrides are also used in the manufacture of electronic devices such as high-power/ high-frequency field-effect transistors (FETs) and high mobility electron transistor (HEMT). [8]
An important application relevant to this thesis is the considerable contribution of UV-LEDs in the medical field such as in the medical diagnostics, UV treatment, and medical tool sterilization. [3, 9] Recently, many reports show the ability of UV-LEDs to eliminate COVID-19, either by being directed toward surfaces, tools, foods. Also, the use of UV-LEDs in the water purification is a mature process nowadays.[3]

It is worth mentioning that a lot of work has been carried out recently on the use of III-nitrides in the domain of nuclear detection, gas detection and on thermo-dynamical devices to transfer the waste energy to electrical power. The low bandgap energy of InN makes it ideal for the solar cells manufactured in combination with GaN to produce ternary InGaN where cover the band energy from 0.7eV to 3.5 eV. [8, 9, 13]

2.2 Growth methods for III-nitrides:

In 1907 AlN was reported and three years later, InN was synthesised and became available.[14] In the 1930s, the first polycrystalline gallium nitride (GaN) was produced using a chemical process analogous to molecular-beam epitaxy (MBE).[15] The growth of III-nitrides is commonly performed on foreign substrates (heteroepitaxy) unlike conventional III-V semiconductors such as GaAs and InP, which are always grown on a native substrate (homoepitaxy). This is due to the difficulty of producing bulk nitride crystals.[15]. In the case of heteroepitaxy, the lattice mismatch between the nitride layer and the foreign substrate and the difference in thermal coefficient, are contributing to a huge number of extended defects in the material such as threading dislocations (TDs).
Numerous growth techniques are used to grow epitaxial III-nitrides thin films. For the sake of simplicity, I will only discuss three main techniques; metalorganic vapour phase epitaxy (MOVPE), molecular beam epitaxy (MBE) and hydride vapour phase epitaxy (HVPE). MOVPE and HVPE are the growth methods which were used to produce the samples studied in this thesis.

2.2.1 Molecular beam epitaxy (MBE):

The basis of molecular beam epitaxy (MBE) is the reaction of atomic beams on a heated substrate. The group III-elements are provided from metal sources, while the nitrogen is supplied to the reactor in a gas source, where they react on a heated substrates surface. The requirements for this technique are an ultra-high vacuum reactor and a high temperature but much less than in the MOVPE technique. In comparison to other techniques, MBE is expensive, and the growth rate is very low (≈1μm/hr). [15]

2.2.2 Metalorganic vapour phase epitaxy (MOVPE):

The metal-organic vapour-phase epitaxy (MOVPE) method is widely used to fabricate III-nitride devices, like LEDs, LDs and transistors. It started being used in the 1960s. [16]

In general, the source of nitrogen in this process is NH_3 and the source for Ga, Al and In is Trimethyl-(Gallium, Aluminium, Indium) (Ga, Al, In $(CH_3)_3$ /(TM (Ga, Al, In)), or Triethyl-(Gallium, Aluminium, Indium) (Ga, Al, In $(C_2H_5)_3$/ (TE (Ga, Al, In)). [17]

In the MOVPE reactor, the metalorganic vapours are transferred from bubblers by a carrier gas H_2 or N_2 to the heated substrate (800°C -1000°C) where the chemical reaction between the compounds takes place as follows:

$$Ga(CH_3)_3\ \text{(vapour)} + NH_3 \rightarrow \text{GaN (s)} + 3CH_4\text{(vapour)(liquid)}$$

This technique requires a high temperature and a very high flow rate of the sources (V/III ratio). Also, it requires a chamber designed to ensure no premature reactions between the ammonia and the III- group sources occur. The production of epitaxial GaN requires a temperature of ≈1050°C while for AlN is higher, ≈ 1200°C. Lower temperatures are required for material containing higher In concentration. (500 - 600°C). [7, 18]

The production of ternary compounds, for instance, AlGaN and InGaN, can be achieved by combining TMAl or TMIn synchronously with TMGa as described in the equation:

$$\text{x}(CH_3)_3\,\text{Al} + (1-\text{x})\,(CH_3)_3\text{Ga} + NH_3 \rightarrow \text{Al}_X\text{Ga}(1-\text{x})\text{N} + \cdots$$

Doping in the MOVPE reactor is possible using silicon (Si), Germanium (Ge) or selenium (Se) for n-type doping and magnesium (Mg) or zinc (Zn) for p-type doping. The most common compounds used for doping in MOVPE reactors are SiH_4 and CP_2Mg for n-type and p-type respectively. Figure 2.4 is a schematic diagram showing the basics of the MOVPE reactor. [17]

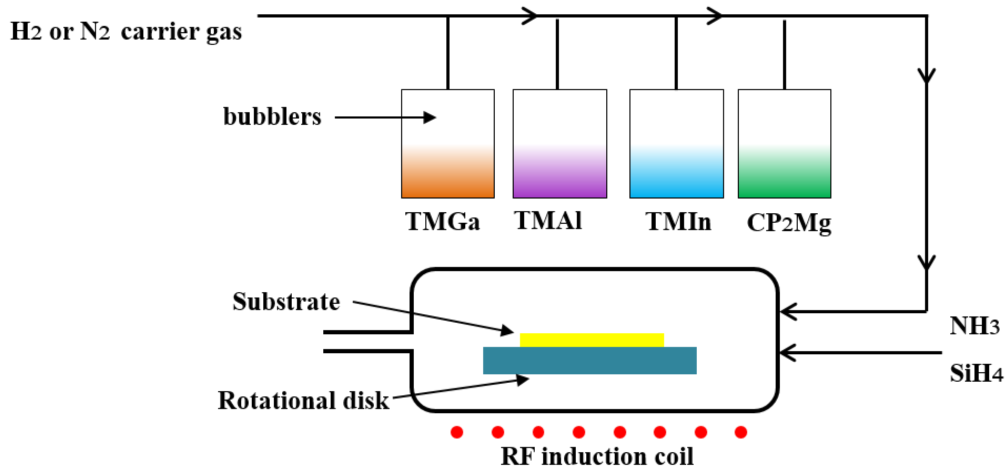

Figure 2. 4 Schematic of the MOVPE reactor adapted from [17].

2.2.3 Hydride vapour phase epitaxy (HVPE):

The most attractive feature about this growth technique is the high growth rate which is approximately (1µm/min) for a sample with a diameter of 2 inches with thicknesses reaching several millimeters for GaN. [19] It is commonly used to produce high-quality thick samples (free-standing) where the substrate on which it has been grown is removed. Freestanding HVPE wafers can be used as a native substrate for III-nitrides. In HVPE, the group V elements are supplied by hydrides (AsH_3, NH_3 etc.), and the supply of the group III elements are chlorides such as GaCl, AlCl etc. The reactor contains two zones: a source zone and a growth zone.

The growth zone starts with the reaction of HCl gas fluxes over melting metallic Ga, In and Al sources in the source zone at temperature 850°C:

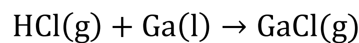

$$\mathrm{HCl(g) + Ga(l) \rightarrow GaCl(g)}$$

On a heated substrate, the output GaCl will react with NH_3 gas in the growth zone with a temperature of 950°C-1050°C by the following reaction:

$$\mathrm{GaCl\ (g) + NH_3(g) \rightarrow GaN\ (g) + HCl\ (g) + H_2}$$

N_2 is used as a carrier gas for both HCl and NH_3 gas fluxes. [14, 17, 19] Figure 2.5 shows the schematic of the HVPE reactor:

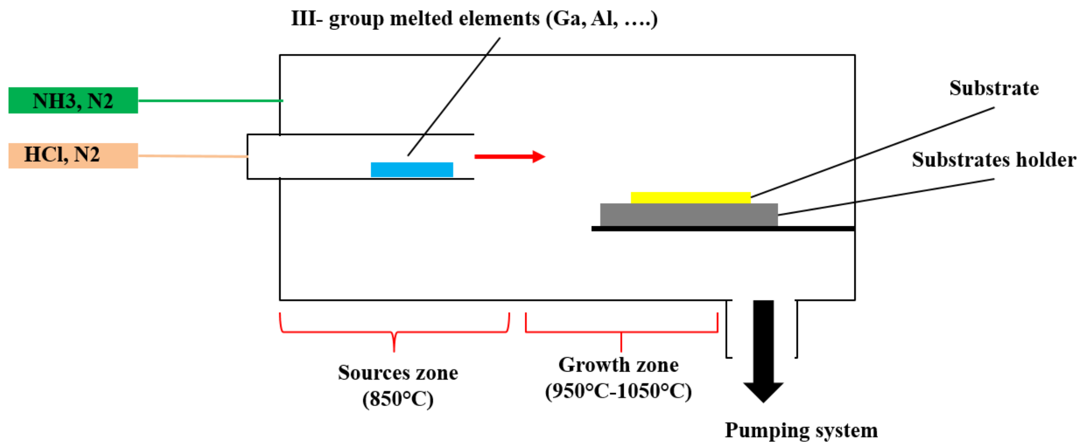

Figure 2. 5: Schematic of the basic idea of the HVPE reactor adapted from [17] .

2.2.4 Substrates

Substrates play a significant role in the field of semiconductor growth. The high quality of semiconductor materials was obtained by growing on the native-substrates (eg. GaN/GaN, AlN /AlN etc). It is worth noting that the performance of devices grown on a native substrate is significantly better than those grown on foreign substrates.

The advantages of growing on native substrates are as follows;

i. Lower density of defects and a smooth surface.
ii. Good thermal conductivity.
iii. Good electrical conductivity and simple design. [19]

Despite all of these advantages, III-nitride bulk native substrates are not widely available for homo-epitaxial growth due to the high prices of GaN and AlN substrates and their limited size. As a consequence of this, researchers were forced to find alternative substrates to grow III-nitrides and ensure a high quality of materials. Numerous parameters are taken into consideration in choosing any substrate, such as lattice constant mismatch, thermal expansion coefficient mismatch, thermal and chemical stability, conductivity, the availability, cost and the wafer size.

The foreign substrates which are commonly used to grow III-nitrides are Al_2O_3 (sapphire), Si and SiC. The mismatch in lattice constant and thermal expansion coefficients between the substrate and the epilayer of III-nitride leads to critical impacts on the quality of the grown device.

Sapphire is widely used to grow III-nitride samples. Around 80% of the growth of GaN is dominated by sapphire. All of the samples which have been studied to present in this thesis were grown on sapphire. Sapphire substrates are commonly used due to their wider availability, low cost and the fact that they are chemically and thermally stable during the growth.

Materials	Lattice constant a (A°)	Lattice constant c (A°)	Thermal expansion coefficient α_a 10^{-6}[K^{-1}]	Thermal expansion coefficient α_c 10^{-6}[K^{-1}]	Lattice mismatch to GaN (%)	Lattice mismatch to AlN (%)
Al_2O_3	4.758	12.991	7.5	8.5	14.8	12.5
6H-SiC	3.081	15.117	4.2	4.7	3.4	-0.96
Si	5.431	5.431	3.59	3.59	16.9	22.3
GaN	3.189	5.185	3.17	5.59	0	-2.4
AlN	3.111	4.982	5.3	4.2	-2.45	0

Table 2. 1: The properties of GaN, AlN and the foreign substrates utilized in the growth of III-nitride devices. [20, 21]

In 1969, the first GaN thin film on sapphire (0001) substrate was grown by Maruska et al. in an HVPE reactor.[22] The growth of GaN directly on sapphire leads to enormous issues in thin films such as cracks, bowing of the wafer, generation of dislocations and stacking faults as a result of the lattice and thermal expansion coefficients mismatch between two layers (≈ 14%) (see Table 2.1), which introduce stress to the GaN epilayer. To eliminate this problem, Amano et. al.[23], reported a high-quality GaN crystal with smooth surface morphology by depositing a thin buffer layer of AlN between the substrate and the GaN to relax the strained epilayer in MOVPE and MBE. The lattice mismatch between GaN and AlN is 2.45% (see Table 2.1).

Nakamura reported for the first time (1991) high quality of a GaN thin film created by utilizing a thin GaN buffer layer grown at a lower temperature (thickness ≈ 20 nm). The thin film had smooth morphology and a flat wafer. Below I briefly summarise the process used to reduce the mismatch between a GaN layer and a substrate using either AlN or GaN as a buffer layer. This is called the two-step growth process. [24]

First, the growth start on heated substrate of ≈ 1050°, high temperature is required for cleaning purpose. Then, the gas sources, Trimethylgallium (TMGa) is used as the Ga source and and NH_3 gas is used as the source of N,were directed to the substrate at lower temperatures between 450°C and 600°C to grow the GaN buffer layer (in the case where AlN is desired as a buffer layer the trimethylaluminum (TMAl) is used as the Al source instead of Trimethylgallium (TMGa)) with a thickness of no more than 120 nm. Finally, the growth temperature was increased to ≈ 1030°C to continue the growth of the GaN epilayer. Currently, the production of III-nitride based light-emitting diodes (LEDs) has been mainly done using sapphire substrates and using GaN as a buffer layer. [15, 24, 25]

2.3 Defects in III-nitrides:

As a result of heteroepitaxial growth of III-nitrides, the generation of defects is inevitable during the growth. The presence of defects in nitrides have a detrimental impact on the device performance. Thus, I will briefly review the defects in III-nitrides, which can be classified depending on their geometry in the crystal as follows:

2.3.1 Point defects

All crystals contain different kinds of defects which modify their structure from the ideal one. Point defects can be associated with a vacancy, interstitial atom and substitutional atom. A vacancy is produced when an atom is missing from its position in the lattice. A pair of two vacancies is known as the Schottky defect. An interstitial atom is an atom that localizes in a lattice position that should not contain any atom. A defect pair comprising an interstitial and a vacancy is known as the Frenkel defect. The balance of the charges in the crystal can be affected by a single point defect so that pairs of defects can resolve this problem by neutralising the charge. There is also an anti-site defect where an atom A is located in the B atom position. The substitutional atom is an external atom that is introduced to the lattice it does not belong to and replaces the original atom. [21, 26, 27] Figure 2.6 demonstrates all point defects types.

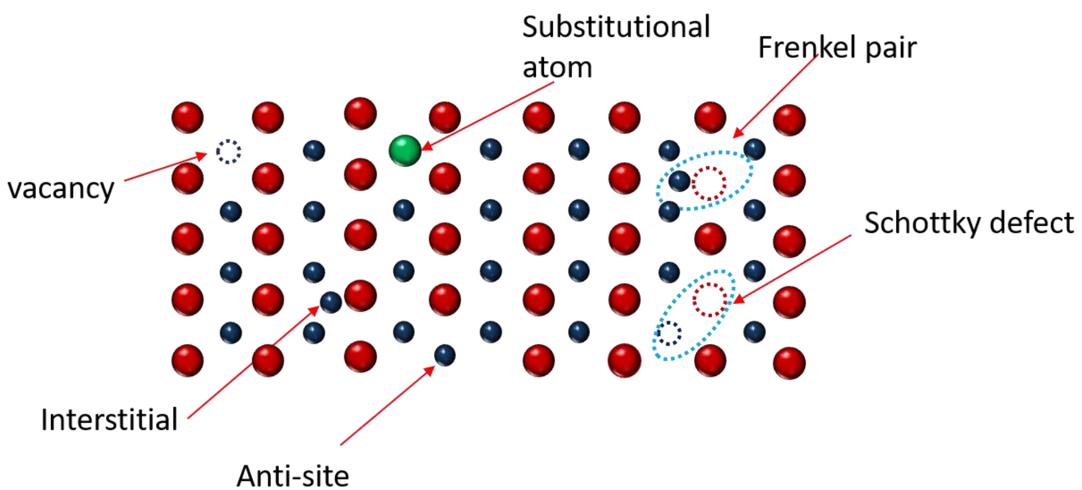

Figure 2. 6: Shows the various point defects that can be formed in a crystal adopted from [27].

2.3.2 Line defect: threading dislocations (TDs)

The atomic arrangement deviates from the ideal shape under an external force leading to dislocations. Dislocation is a line defect which can be described by two main vectors *u*, the dislocation line, and *b*, the Burgers vector. In *c*-plane nitride semiconductors, where growth is along < 0001>, the dominant dislocations are edge, screw and mixed dislocations. For the edge dislocations *u* and *b* are perpendicular to each other and are <0001> and $\frac{1}{3}$ <11$\bar{2}$0> respectively. A dislocation with a Burgers vector of $\frac{1}{3}$ <11$\bar{2}$0> is also referred to as an *a*-type dislocation. For screw dislocations *u* and *b* are parallel to each other and are <0001>. A dislocation with a Burgers vector of <0001> is also referred to as a *c*-type dislocation. For mixed dislocations *b*= $\frac{1}{3}$<11$\bar{2}$3> and the dislocation line is typically a few degrees from the <0001> direction, it can referred to as (*a*+*c*)-type.[28] Advanced growth techniques used to reduce dislocations, for example epitaxial lateral overgrowth (discussed in section 2.4) or silicon doping, can lead to dislocations bending. [29] If an edge dislocation bends away from the [0001] direction it can no longer be referred to as an edge dislocation, but as long as its Burgers vector does not change it can still be referred to as an *a*-type dislocation. Similarly if a screw dislocation bends away from the <0001> direction it can be no longer referred to as a screw dislocation, but as long as its Burgers vector does not change, it can still be referred to as a *c*-type dislocation. If two dislocations of opposite Burgers vectors meet they will be eliminated.

An edge dislocation is introduced into the atomic structure by inserting a half plan to the crystal see figure 2.7.a. A screw dislocation results when one side of the crystal is sheared with respect to the other side (see figure 2.7.b). A mixed dislocation or (*a*+*c*)-type is a combination of edge and screw dislocations, the dislocation line *u* and the Burger vector *b* are neither perpendicular or parallel to each other with *b*= 1/3[11$\bar{2}$3]. Edge, screw, mixed dislocations can be threading dislocations. The definition of a threading dislocation is one which cannot end inside the material, but threads up to the free surface. [30] In the III-nitrides, threading dislocations TDs are introduced to the crystal during the growth. The origin of TDs in III-nitrides is still not completely understood. Many studies believe that TDs form at the coalescence boundaries of

misoriented islands during film growth. This leads to a structure with sub-grains that are tilted and twisted with respect to each other. The closely spaced arrays of TDs are assumed to have formed at grain boundaries. [31, 32] Similarly, arrays of TDs can be seen in coalescence areas in samples that are grown on patterned masks (selective area growth/ELOG). [33] Other model believe that TDs form in the low temperature buffer layer, followed by TD movement at higher temperatures. Research shows that the highest (*a* +*c*)-type TD densities were found in the buffer layer, these decrease with TD loop formation (helped by grains facets) and reaction producing *a*-type TDs. [34]

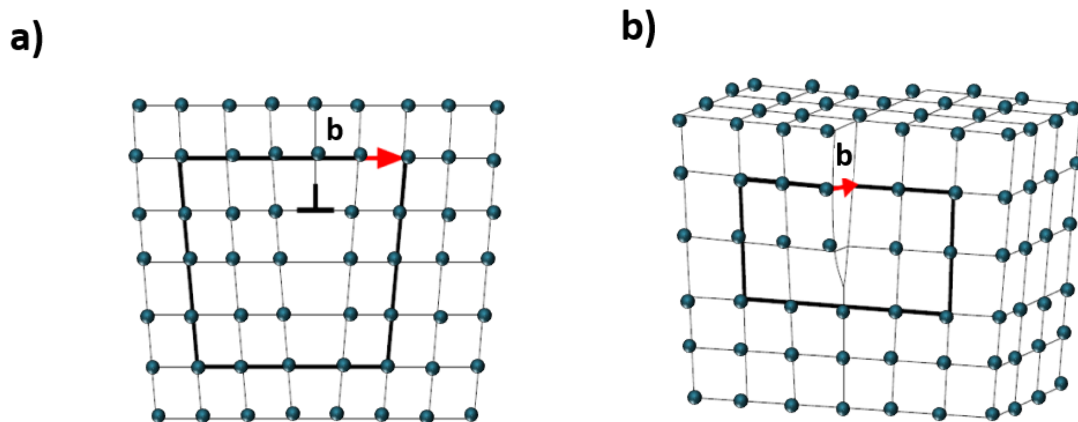

Figure 2. 7: a) Edge dislocation as an inserted half plan to the crystal and b) The screw dislocation as the side of the crystal is sheared respect the other side in both images b indicate to Burger vector adapted from [28].

2.3.3 Surface defects

Two-dimensional defects introduced to the crystal are known as surface or planar defects, examples are grain boundaries and stacking faults. A fault in the stacking sequence of bulk layers is known as a stacking fault. It is associated with an additional (same or different type of the crystal material) or a missing layer. For example, if we consider that the stacking sequence of a crystal to be ABABABAB, the stacking fault is introduced as ABABBABA.[35]

Low angle grain boundaries are interfacial surfaces located between two misaligned grains. Arrays of aligned dislocations will lie along a grain boundary.[36] Where a low angle boundary results from an in-plane rotation, edge dislocations will be aligned along the boundary, where a low angle boundary is a result of an out-of-plane rotation, then screw dislocations will be aligned along the boundary. The density of dislocations will increase as the misalignment angle increases. [36, 37] Low angle grain boundaries are common in III-nitrides.[38] For example, both low tilt and twist boundaries measured to be 0.3° and 0.11° respectively, in the case of grown GaN using ELOG method (ELOG is explained in the following section). [39]

Banal et al. [40] reported that the formation of the low angle grain boundaries in AlN/sapphire sample raised at the initial stage of growth . In the absence of those features, an enhancement in the light emission is achieved. These defects can be eliminated by using the two-step growth method, which is described previously in section 2.2.3. Figure 2.8 shows misorientated grains in different coloured arrows which indicating to different orientation directions.

There is also a defect known as a volume defect or bulk defect. This defect is a 3D defect as obvious from the name. It includes voids, cracks and foreign phases, that may be introduced to the crystal during the growth process.[41]

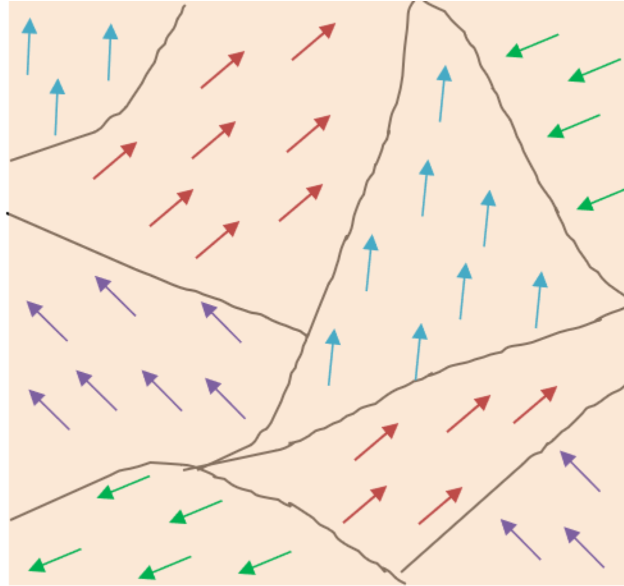

Figure 2. 8: The sub-grain boundaries with different coloured arrows represent the different directions of grain orientation.

2.4 Reduction mechanisms of dislocations in III-nitrides

The growth of III-nitride on foreign substrates leads to a high density of TDs with densities range from $\approx 10^{8}$-10^{11} cm^{-2}. Since in nitride thin films dislocations have a detrimental impact on the performance of the III-nitride based devices, significant effort has been invested on improving the growth techniques to reduce TD densities. Lee, K. and Auh, K. [42] estimated that the growth of thicker GaN samples leads to a reduction in TDs density. For samples with a thickness of 3 µm, 300 µm,500 µm and 750 µm the density of TDs was estimated to be 9×10^{9} cm^{-2}, 1×10^{7} cm^{-2}, 5×10^{6} cm^{-2}, and $\approx 2\times10^{6}$ cm^{-2} respectively. However, increasing the thickness of a sample can result in stress relaxation mechanisms such as cracking.[43, 44] Hence, the growth of a thicker layer cannot always be a successful strategy, alternative techniques are required.

2.4.1 Epitaxial lateral overgrowth (ELOG)

Epitaxial lateral overgrowth (ELOG) is an advanced growth technique that can be performed either in MOVPE or HVPE and achieves a considerable reduction in the TD density (TDD). The basic idea of this technique is based on filtering TDs, reducing their density in a certain area of the samples. In addition, it takes advantage of the dislocations bending behavior on overgrowth, leading to the interaction and annihilation of TDs with each other in ELOG samples. It was originally used in the growth of conventional semiconductors material (GaAs). [45] Then, Kato et al. were the first to propose this technology to the field of III-nitrides growth, by growth by selective epitaxy of GaN on a sapphire substrate by MOVPE. [28] The first successful application of this technology in III-nitrides was by Nakamura et al.[46] He was able to produce a blue laser with a lifetime greater than 10000h using an ELOG substrate. For standard growth of GaN on sapphire TDD are typically around 6×10^{8} cm^{-2} whereas for ELOG, the TDD is estimated to be 5×10^{6} cm^{-2} .[47]

The basics of this technique starts first with a thin layer of standard GaN which is grown on a suitable substrate by MOVPE or HVPE as the nucleation layer. A dielectric mask of SiO_2 or SiN_x is then deposited on the GaN layer and etched to make periodic stripes (opened and closed regions) using photolithography. The periodic open and closed areas are referred to as the window and wing regions respectively. Subsequent growth results, ingrowth through the unmasked regions and lateral epitaxial overgrowth extend over the mask. Dislocations under the mask cannot propagate into the lateral epitaxial layer. Also, dislocations which pass through the window near the edge of the mask bend about 90°(see figure 2.9) toward the basal plane and interact with other bending dislocations and annihilate each other. Therefore, the wing region has a lower density of TDs except those dislocations located on the coalescence boundaries in the middle of the wing region. Consequently, the production of efficient devices will be based on the wing regions, where the lower TDs density located.

Numerous factors are crucial in ELOG growth such the mask direction, size, and the growth conditions (pressure, the temperature, and the time) and the utilized substrate. [47] [28] For example, for the dielectric mask aligned along [1-100] the epilayer morphology depends on the growth conditions. The morphology of the sample changes from a rectangular shape to a pyramidal shape as a result of increasing the

reactor pressure with a reduction of the growth temperature. While increasing the growth time, the pyramidal shape dominates in the case of the mask oriented toward [11-20], the initial morphology of the sample shows the formation of a pyramidal shape independent of the growth conditions.

To achieve a full coalescence on samples epilayer by using ELOG method; we can classify ELOG into one- step (1S-ELOG) or two- steps (2S-ELOG). In 1S-ELOG, the growth conditions remain unchanged and the regrowth is completed in one step. In 2S-ELOG, after starting the growth as in one-step, the growth conditions such temperature, the pressure and the III/V ratio to complete the regrowth process and achieve the full coalescence across the sample surface. The 2S-ELOG can be also achieved by depositing a dielectric mask above the previous opening area to prevent the dislocations generated in this area from propagating to the sample epilayer. This method is not favoured due to the cost and complexity.[28, 45, 47-49] Figure 2.9 illustrates the TD's behaviour where the bending behaviour is the key to TDs reduction in such a growth method.

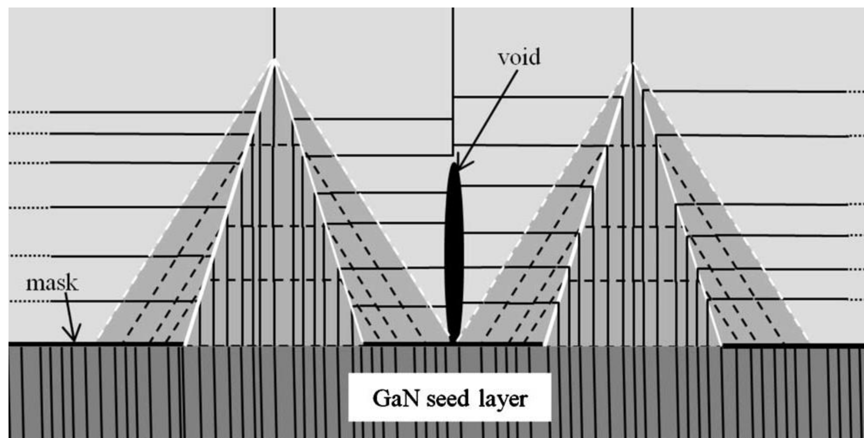

Figure 2. 9: Shows a schematic of the behaviour of TDs in ELOG process adapted from [50].

2.4.2 Nano patterned sapphire substrates (nPSS)

Nano-patterned sapphire substrates (nPSS) is an advanced technique derived from ELOG and patterned sapphire substrates PSS (PSS). The basic idea of this technique is the transfer of the desired pattern into the sapphire substrate rather than on the mask as in ELOG (maskless technique). The first proposal of PSS in nanoscale level was in 2000 by Ashby et. al.[51], where he assumed the growth on sub-micron PSS will lead to an improvement in the materials' quality and enhance their electrical and optical properties. Chen et. al.[52] demonstrated that nano-scale PSS (nPSS) provides a huge reduction in TDs density compared to micro-scale PSS in the epitaxial growth of GaN. The density of TDs for GaN grown on a conventional sapphire substrate is estimated to be about 1×10^{9} cm^{-2}, while for the GaN grown on the nPSS, the density of the TDs is estimated to be less than 1×10^{7} cm^{-2}.[53] Recently, this technique has attracted a lot of attention from the growers due to the capability of decreasing the density of TDs which in turn enhance the light output power consequently producing high performance of III-nitride-based devices (e.g. LEDs). [54-56]

The pattern configuration on the sapphire substrates surface can be holes, stripes, or hexagons with nanometre dimensions. Starting with depositing some dielectric and resists layers on a sapphire layer. Then, a metal layer deposited on the top and start preparing the desirable patterned mask. Lift-off to create the metal nano dots pattern on the III-nitrides layer. Final stage dry etching by chlorine transfer the nano pattern to the III-nitride layer.[57]

Analogous to ELOG, this technique utilises bending of TDs as a TD reduction mechanism. The propagation of TDs which arise at the III-nitride/sapphire interface above the unetched area, then either propagate vertically or bend toward the voids sidewalls for those which located near the voids and terminate there, see figure 2.10. Also, dislocations arise in the coalescence zone surrounding grain boundaries. The density of TDs is dependent on the area of the coalescence zone. TDs in nPSS techniques can be classified depending on their behaviour during the growth and are summarised in figure 2.10. The first category is the TDs (edge, screw or mixed) that arise at the interface of the nitride thin films with the sapphire in the unetched region due to the large lattice mismatch. The second class is those TDs that are located near the void and tend to bend towards the void sidewalls by image forces [58] and

terminate at the inner surface. This process contributes to the reduction of TDD in the epilayer. The third class is those TDs that are generated as a result of the coalescence and form grains with different orientations to each other. [58]

Table 2.2 lists the advantage of ELOG and nPSS growth processes and highlights their differences with respect to the growth steps, cost, the residual mask, the TDs density, and their availability.

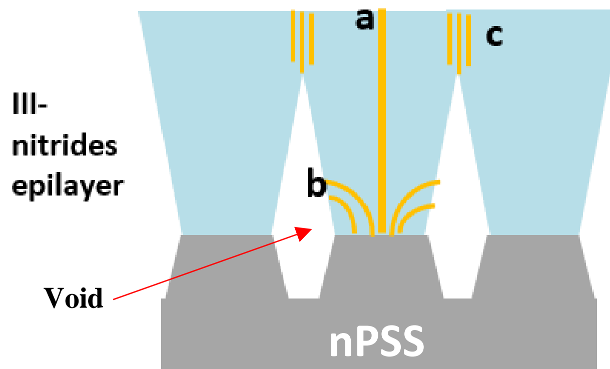

Figure 2. 10: Illustrates the behaviour of TDs in material grown on nPSS, a is the vertical dislocation above the unetched region, b is the bending dislocation near the voids toward the voids sidewall, and c is the dislocations at the coalescence zone, adapted from [58].

Items	nPSS	ELOG
Growth	Single growth step without a mask	More than two growth processes and the mask is essential
Cost	Cost is cheaper since the growth time is short	Higher cost due to multi-growth steps
Mask	Maskless	Contain a mask
TDs density	Reach 10^8 cm^{-2}	It can achieve lower than 10^7 cm^{-2}
Availability	Used in GaN-LEDs	Used on GaN Substrate of LDs
Advantage	Increase IQE, LEE, EQE and reduce TDs density	Reduced TDs density

Table 2. 2:Shows the comparison between the ELOG and nPSS on GaN.[47] [56] [53]

2.4.3 The miscut substrate

The growth of III-nitride thin films on miscut substrates, deviation away from the vertical direction (in the case of sapphire [0001] direction) toward other direction, can be used as a TDs reduction mechanism. Growth on miscut substrates can lead to a significant impact on the sample morphology, the formation of step bunches is one consequence, see figure 2.11. The step bunches is morphology features common in III-nitrides, contain bunches of monoatomic steps and are several monoatomic steps high. [59, 60].

The reduction of the dislocation density in the presence of step bunches is discussed in references [59, 61] where AlN and GaN samples were investigated using cross-sectional TEM. It based on the mechanism of bending dislocations, similar to the dislocation reduction mechanism discussed in previous sections 2.4.1 and 2.4.2.

References 54 and 56 show that the step bunches introduce new free surfaces to the growth, thus TDs tend to approach the nearest free surface or void. [62] When the free surface and the image force of the side face is larger than the top face (growth direction) this leads dislocations to bend and line up at the step bunches (confirmed by the etching method image in ref.[63], as the dislocations lined up at the step bunches) and in figure 6.4 in chapter 6. The image forces of faces (top or side) depend on various conditions like the height of the step bunches and the side face orientations. The reduction mechanism takes place when the inclined dislocations interact with the vertical ones and either form dislocations loops, annihilate each other or forming a new TD aligning at the step bunches see figure 2.11.

Increasing the miscut angle results in increasing of the step bunch density, or in other words the distance between the step bunches is decreased. [64-68] The direction of the miscut substrate influences the morphology of the sample. Shen et al. [67] found that a miscut in the direction toward the *a* plane of the sapphire substrate resulted in step bunches with a straight edge, also step bunches formed in GaN epilayer at the miscut angle of 2° step bunches formed in GaN epilayer. Someya et al.[69] reported GaN smooth surface morphology, which has grown on a sapphire substrate with offcut of 0.25° toward *a* plane. Also, in the case of the sample coalescence Kueller et al.[70] reported that faster coalescence could be achieved in the case of ELOG AlN sample grown on sapphire substrate with miscut of 0.25° toward the *m* plane compared the one grown on the substrate with 0.25° miscut toward *a* plane. Also, Gunnar et al. [71] demonstrated the influence of small changes in substrate miscut on the surface and the optical properties of the AlGaN thin film. Two samples were investigated in their study, sample A with 0.1° miscut angle of the substrate and sample B of 0.4° miscut angle.

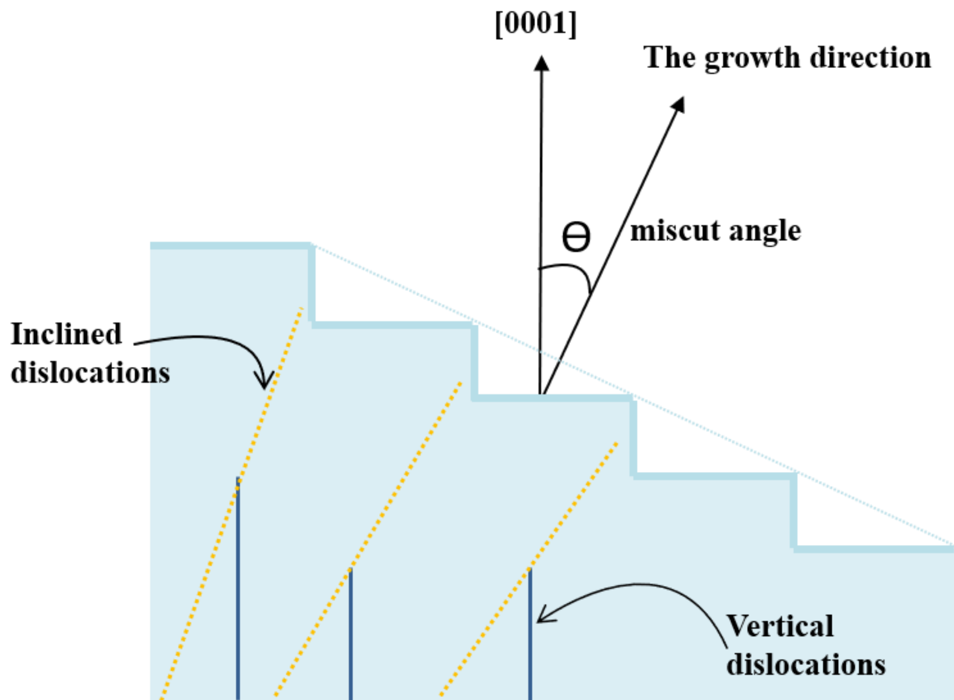

Figure 2. 11: Schematic illustrates the mechanism of TDs reduction by their inclination toward step bunches and interact with other vertical TDs to annihilate each other and forming a dislocation loops.

2.5 Characterisation of structural properties

A wide range of techniques can be used to investigate structural defects such as TDs and sub-grains in crystalline material. Diffraction is the main phenomenon that is used in X-ray diffraction (XRD), transmission electron microscopy (TEM), electron channelling contrast imaging (ECCI) and electron backscatter diffraction (EBSD). Defects can also be investigated using atomic force microscope (AFM) and cathodoluminescence (CL) imaging. Chemical pit etching techniques may also be used, where chemical solutions are used to treat the surface of the sample, opening pits where TDs are located. The sample can then be examined using AFM or the SEMto image the pits and the TDs and their types can be identified. Here I provide an overview of TEM, XRD, and CL. ECCI, EBSD, and AFM are the main techniques used in this thesis and will be discussed in detail in chapter 3.

1. Transmission electron microscope (TEM)

To date, the TEM is the best and most reliable technique used to identify threading dislocations in III-nitrides. A thin sample (≈100 nm- 1000 nm) and high electron energy (≈100 kV) are required to obtain a TEM image. It is worth noting that TEM investigations can be either cross-sectional where the inner construction of the sample can be investigated (cross-sectional TEM) or in plan-view geometry, by placing the sample perpendicular to the incident e-beam (plan-view TEM). Both methods can be used to reveal and identify TDs, Figure 2.12 shows TEM image from both methods. The planes surrounding dislocations are distorted compared to those far away from the location of dislocations. Under diffraction conditions, these can be seen in a TEM image as a reduction in the signal intensity of the transmitted beam and thus dislocations produce contrast.

The invisibility criteria ($\boldsymbol{g} \cdot \boldsymbol{b} = \mathbf{0}$) and ($\boldsymbol{g} \cdot \boldsymbol{b} \times \boldsymbol{u} = \mathbf{0}$) are used to classify TDs types, where g is the diffraction vector, b is the Burger vector and u is the dislocation line. The basic principle of these criteria is that the sample is imaged under different diffraction conditions where the type of dislocation will be visible under one condition and invisible in another condition. The criterion will be achieved when the $\boldsymbol{b}$ and $\boldsymbol{g}$ are perpendicular to each other and where the contrast will be maximized when $\boldsymbol{g}$ and $\boldsymbol{b}$ are parallel to each other. In the case of an edge dislocation, both criteria should be satisfied. In the case of a screw dislocation only ($\boldsymbol{g} \cdot \boldsymbol{b}$) need be applied. For example, in *c*-plane III-nitrides as mentioned before the Burgers vector $\boldsymbol{b}$ for edge dislocation is $1/3<11\bar{2}0>$ then the $\boldsymbol{g}$ vector (0002) fulfils the invisibility criteria for edge. In the case of a screw dislocation(*c*-type) where $\boldsymbol{b}= <0001>$ then the $\boldsymbol{g}$ vector $(11\bar{2}0)$ will meet the invisibility criteria for screw. A mixed dislocation will be visible for conditions where screw and edge dislocations are invisible. [36] [28] However, in the case of plane-view TEM, these invisibility criteria cannot be met for *c*-plane III-nitrides as will be discussed in next chapter (section 3.2).

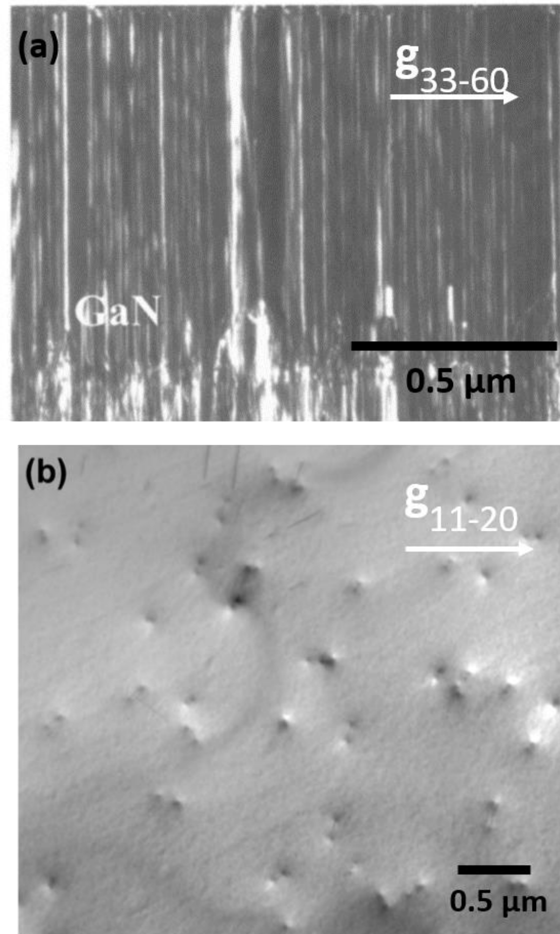

Figure 2. 12: a) Cross-sectional TEM image from GaN sample shows TDs appear as vertical lines, the image is taken from ref. [61] , b) Plan-view TEM image from GaN sample TDs appear as dots with black and white contrast, this image is from ref. [72]. Note both images are from different samples.

2. Cathodoluminescence (CL)

This technique is based on the phenomenon of light emission as a result of the sample excitation by the incident high energy electron beam. CL intensity is influenced by the crystal composition, the structure as well as the surface morphology.[73] This technique can be used with other complementary techniques (e.g. ECCI, AFM, etc.) to explore the influence of structural properties and the surface morphology on the light emission.

CL provide us with light emission information from the sample. Dislocations threading up to the surface of the sample appear as black dots in the CL map as they centers of non-radiative recombination. Figure 2.13 show a CL intensity map acquired from a GaN sample with density of black dots (TDs) of around 5×10^{8} cm^{-2}. [74] and the spatial distribution of the defects through the sample can be determined. The CL method is a reliable method used to image the optoelectronic devices on both the micro and nanoscale with a spatial resolution of tens of nanometers. [75, 76] In comparison to TEM, CL allow exploration of samples with the advantage of a large field of view however, CL does not resolve TDs types .

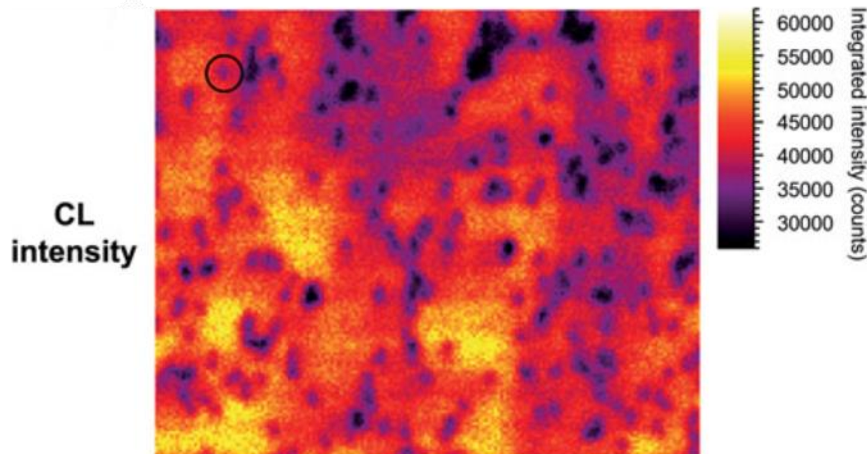

Figure 2. 13: Shows a CL intensity map from GaN sample from ref.[74].TDs appear as black dots and their density estimated to be $\approx 5\times10^{8}$ cm^{-2}.

3. X-ray diffraction (XRD)

X-ray diffraction XRD is a popular technique used in the field of III-nitride characterization as it is useful for quantifying the presence of strain, dislocations, misorientation, and composition. It is based on the phenomenon of elastic scattering of X-rays by the atoms located within the periodic lattice of a crystal. As X-rays generated from an X-ray cathode tube impinge on a sample, both the sample and the X-ray detector are rotated to satisfy the Bragg condition $n\lambda=2d \sin \theta$. Here n is an integer known as the order of reflection, λ is the wavelength of the X-ray, d is the distance between the crystal planes of a given sample, and θ is the angle between the incident beam and the reflecting plane. At certain angles constructive interference takes place and a peak in intensity occurs at the angle 2θ. The relationship between the X-ray intensity versus 2θ is shown as a plot of Gaussian peaks see figure 2.14 . The measurement of crystal structure using the X-ray peaks is not straightforward as dislocations in a crystal expand the width diffraction peaks. The density of dislocations $= \frac{1}{D^2}$. [77]

where D is the crystal size and its value calculated from Scherrer equation:

$$D = \frac{k\lambda}{\beta \cos \theta}$$

Where λ is the wave length , β is the width at half maximum (FWHM) see figure 2.14, k is the shape factor its value ≈ 0.9, and θ the Bragg angle (peak position).

Many materials have distinguishing X-ray diffraction patterns; which helps users identify samples of unknown composition. More about this technique found in references[78, 79].

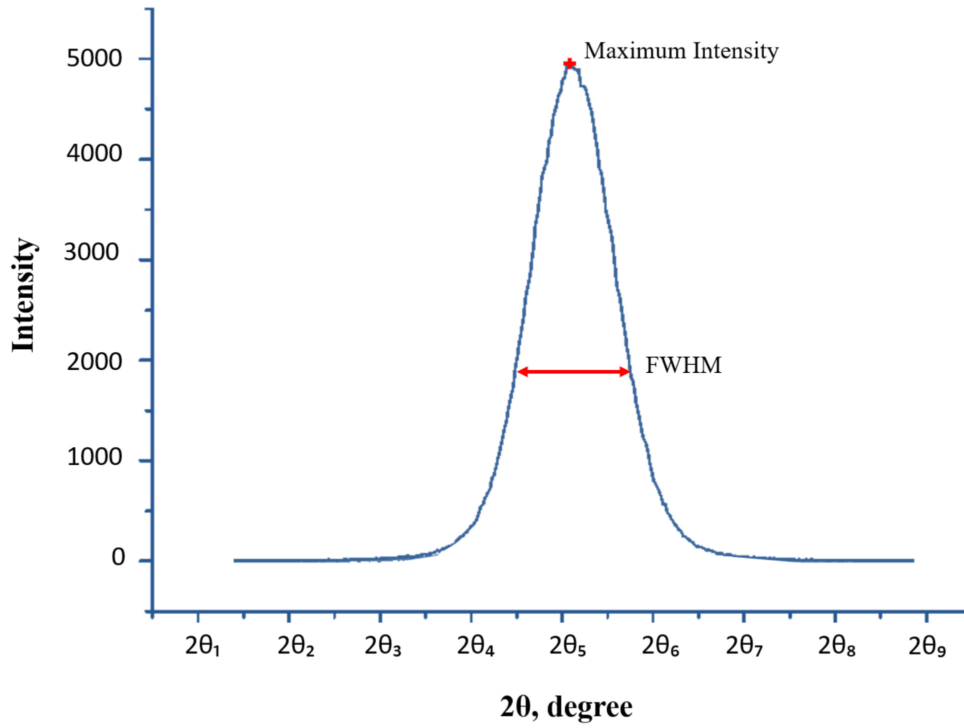

Figure 2. 14: Shows the X-ray Gaussian peak at 2θ and the width at half maximum FWHM and the maximum intensity.

Chapter 3

Methodology

This chapter provides an overview of two microscopies, atomic force microscopy (AFM) and scanning electron microscopy (SEM), as they are the key techniques used to investigate III-nitrides in this thesis. I will also describe the SEM techniques of electron channelling contrast imaging (ECCI) and electron backscatter diffraction (EBSD) used to characterise the structural properties of the materials investigated.

3.1 The principle and operation of scanning electron microscope (SEM)

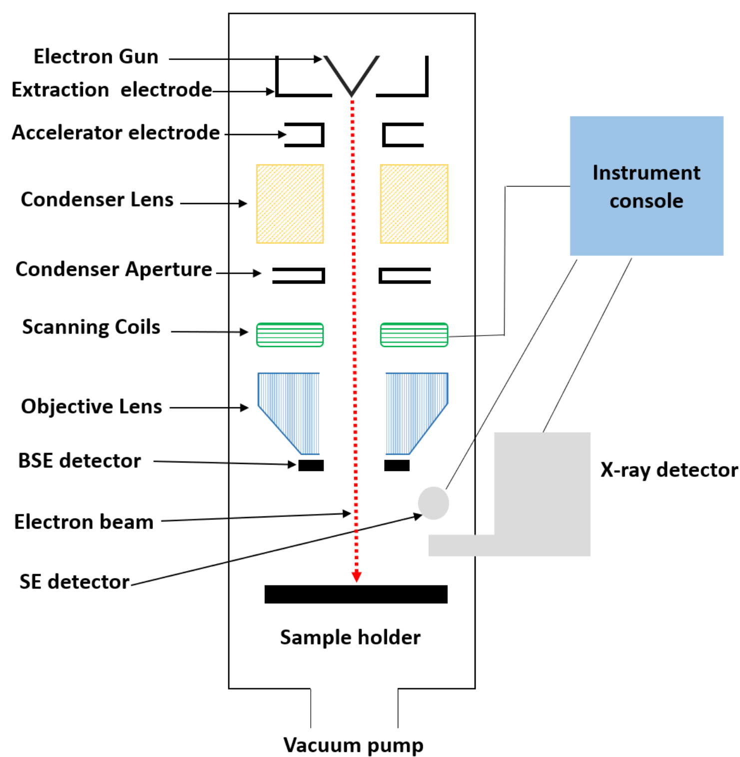

Figure 3. 1: Schematic diagram of the main parts of the scanning electron microscope.

The first scanning electron microscope was built in the 1930s and became commercially available in the 1940s. [80, 81] While visible light is the probe used in optical microscopes, an accelerated electron beam is used for imaging materials in a scanning electron microscope. The shorter wavelength of the electron means that a scanning electron microscope can distinguish between very small features in a sample. The resolution in an scanning electron microscope is significantly increased in comparison to the light microscope, in a scanning electron microscope a resolution of 1 nm is achievable.[82]

Figure 3.1 illustrates the conventional scanning electron microscope components which can be classified into two main parts [80, 82]:

1. **the microscope column**

   i. The **electron gun,** which is located at the top of the scanning electron microscope column, is used as the source of accelerated electrons with an energy typically between 0.2 keV to 30 keV. Different types of guns are used to produce an electron beam such as; the field-emission electron gun (FEG) and thermionic electron gun. For high-resolution imaging a FEG is used. A field emission gun, which is held under an ultra-high vacuum of about 10^{-7} pa (~10^{-9} mbar), contains a cathode which is a tungsten wire with a sharp tip on the order 10 nm in size. A high positive electric field is applied to a metal plate (called the extraction electrode) placed below the wire. As a result of this applied positive electric field, tunnelling occurs and electrons are emitted from the tip. Electrons flow through a hole located at the centre of the extraction electrode. By applying a positive voltage to another electrode, known as the accelerator electrode, as shown in figure 3.1, the electrons will be accelerated to their final energy.

      In the present work, the scanning electron microscope utilised a Schottky field emission gun which is based on Schottky effect phenomenon. In this gun, the extraction of electrons can be achieved by the combination of thermionic emission and electric field. Applying an electric field to the tungsten tip, which is coated with ZrO_2 layer, provides a reduction in the electron work function that contribute to liberation of electrons from the

heated tip. Such a gun is used for high-resolution measurements due to its ability to provide a beam diameter on the sample surface as low as 1 nm.

ii. The two types of **electromagnetic lenses**, the condenser and objective lenses, are located below the electron source and are used to focus the path of electrons down to the sample and control the electron beam diameter together with the beam current. Thus a spot size of 1 nm can be achieved as the lenses demagnify the emitted electrons' beam crossover diameter,

iii. The beam scanning process over the sample is carried out by pairs of **beam deflection coils** that are mounted above the objective lens, see figure 3.1. The focused beam passes through the coils which are used to deflect the beam in the X and Y axes so it scans over a rectangle area of the sample in a raster fashion.

iv. A series of **apertures** are located between the lenses and are made of a thin metal plate which has a small hole, see the schematic of an SEM in figure 3.1. The main function of the apertures is to control the number of electrons that will reach the sample as well as controlling the convergence angle of the beam to ensure that a focused beam reaches the sample.

v. Finally, located at the end of the microscope column is **the sample chamber**, which contains the sample holder and signal detectors (X-ray, SE, BSE detectors), as seen in figure 3.1. The chamber can be held under high vacuum to reduce the electron-gas interaction or low vacuum (the environmental SEM). When imaging insulating samples, the ions produced from some gas in the chamber (typically water vapour or nitrogen), can help to eliminate the charging effect. The chamber has a flexible sample stage that can move in the X, Y and Z directions in addition to tilting T and rotating R the sample. In high vacuum conditions, the sample chamber is held around ~10^{-4} Pa (~10^{-6} mbar). In low vacuum conditions the chamber is held around ~1-2500 Pa (~ 0.01–26 mbar). [83]

In this thesis, two types of scanning electron microscopes have been utilised; an FEI Quanta Schottky FEG 250, which can be operated at both high and low vacuum, and an FEI Sirion 200 Schottky FEG–SEM operated in high vacuum.

2. **The control system**

The control system contains the electronics necessary to control the accelerating voltage, the lenses, scan coils, one or more computer screens for monitoring and displaying acquired images, an amplifier unit to amplify the generated signals (secondary electrons SEs and backscattered electrons (BSEs) and a vacuum system that ensure the pressures required for all parts of the SEM. Moreover, the environmental SEM can be used in high vacuum mode or the low vacuum depend on the examined material. The variable pressure SEM (low vacuum mode) is described in detail in Chapter 5, where its application is a key main topic of discussion .

3.1.1 Electron-sample interaction

In the scanning electron microscope the incident high energy electrons bombard a sample, and as a result, various signals are produced as demonstrated in figure 3.2. Consequently, information on morphology, chemical composition, and the microstructure of the material can be acquired.

Two main categories of interactions can be introduced in an SEM: elastic interactions and inelastic interactions. When undergoing elastic interaction, an electron can be scattered by the atoms' electric field. Therefore, the electron alters its trajectory by an angle $\emptyset$ while its kinetic energy is conserved. The probability of scattering $P(\emptyset)$ is proportional to the square of the atomic number (Z^2) and inversely proportional to the square of the incident electron energy (E^2_{PE}) as follows:

$$P(\emptyset) \propto \frac{Z^2}{E_{PE}^2 \cot^2(\frac{\emptyset}{2})} \qquad (3.1)$$

Where $\emptyset$ is the scattering angle. This equation (3.1) is describing Rutherford scattering, gives rise to the backscattered electron (BSE) signal. [80, 83]

In contrast, inelastic interaction implies a number of physical processes that all result in electron energy loss. Here, the incident beam electrons lose a significant portion of their kinetic energy which is transferred to the sample's atoms, causing the ejection of weakly bounded shallow electrons, which are referred to as secondary electrons (SE), and tightly bounded inner shell electrons which result in characteristic (X-ray) emission, Auger electron emission and cathodoluminescence (CL). Each one of these generated signals can provide different information on the material. [80, 83]

The generation of these signals depends on the interaction volume which can be affected by different factors such as the electrons' energy, the sample's atomic weight, and the geometry of the sample with respect to the incident beam. The resolution of each signal depends on their generated volume for example, SE and Auger electrons are generated from a small interaction volume, so these signals generate the best spatial resolution images. At the same time, X-ray and CL emission produce the lowest resolution images as they have the greatest interaction volume. Figure 3.3 illustrates the signals that can be produced in an SEM with respect to their relative generation depths. It is worth mentioning that Monte Carlo simulations are used to theoretically predict the effect of various SEM parameters on spatial resolution.[83, 84]

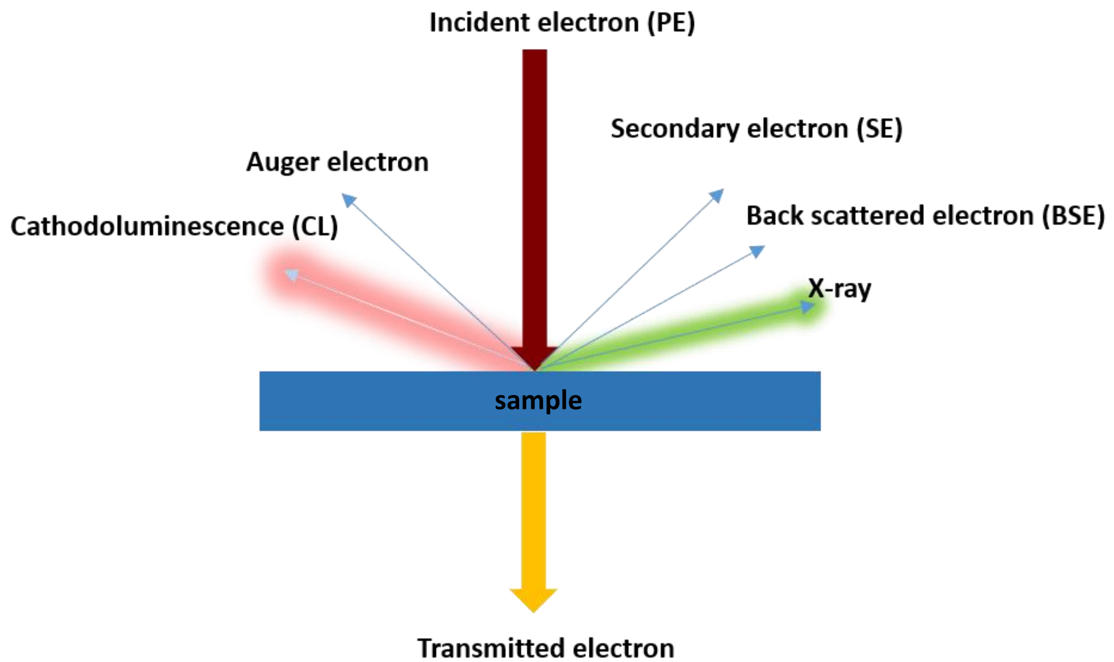

Figure 3. 2: The generated signals of the electron- sample interaction.

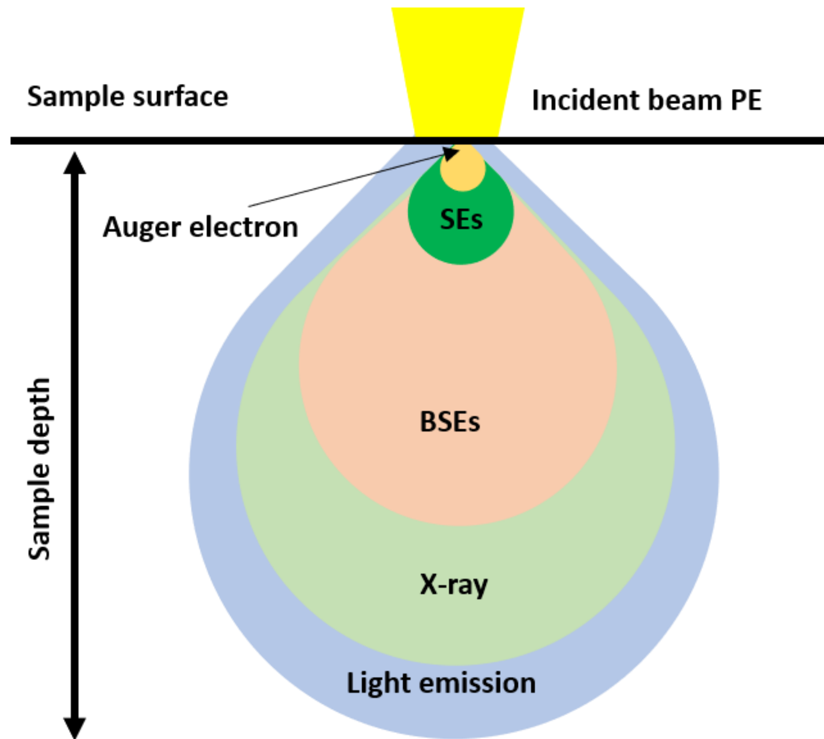

Figure 3. 3: Depth of the generated signals in the scanning electron microscope.

3.1.2 The generated signals

Secondary electrons (SE) have an energy of a few eVs ($E_{SE} \leq 50$ eV). There are three types of secondary electrons:

i. SE1, is the secondary electron signal generated via the direct interaction between the incident primary beam and the sample.
ii. SE2 is the secondary electron signal generated as a result of the collision of backscattered electrons (BSE) with inner atoms, on their trajectory to escape the sample
iii. SE3 is the generated electrons from other chamber surfaces or the pole piece inside the sample chamber of an SEM as a result of BSEs and primary beam (PE) strikes, respectively.

The SE1s and SE2s emerge from, or close to, the sample surface. Due to their low energies, these electrons can travel only a few nanometres. Their signal can provide topographical information that can be used to study a material's surface in a scanning

electron microscope. *H. Knoll* was the first person to use the SE signal to generate an image of the morphology of a bulk sample.[80]

Backscatter electrons (BSE) can have energies ranging from the primary beam energy to close to the energy of secondary electrons (SEs) (50 eV $\leq E_{BSE} \leq E_{PE}$).
The primary beam electrons (PE) that travel for a distance before being scattered by the sample's inner atoms and whose trajectory deviates back out through the sample surface are known as backscattered electrons (BSEs). BSEs can be deflected from deep in the sample before emerging back through the surface. The energy of BSEs varies depending on the material's atomic number and the travelled distance. As shown in figure 3.4, the BSE energy distributions can be classified into two regions, the near primary beam energy (region I) that dominates in the case of high or intermediate atomic number materials. The highest energy corresponds to those primary beam electrons that are scattered immediately after entering the sample or after travelling only for a short distance. The electron, in this case, is deflected as a result of a single collision with the atoms thus its energy approximately preserved (quasi elastic scattering).
In the case of light materials, the primary beam travels deeper through the sample and the electrons undergo numerous collisions with atoms. Therefore, they will lose energy inelastically before scattering out of the sample. The BSE energy in region II (see figure 3.4) covers a wide energy range that is located between the primary beam energy down to close to the energy level of SE $\approx<$ 50 eV. Region III in figure 3.4 is relevant to the energy of SE $\approx<$ 50 eV.

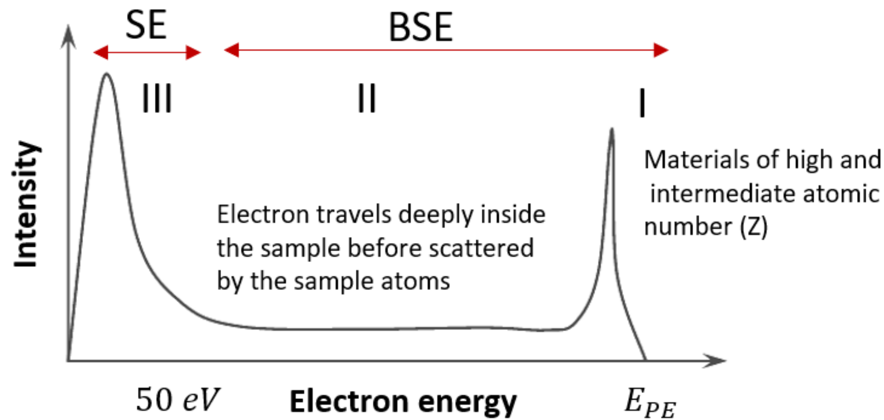

Figure 3. 4: The distribution of SE and BSE energy. Regions I and II correspond to BSE energies, and region III to the SE energy. Adapted from reference [82].

3.1.3 The detection system in a conventional scanning electron microscope

For **secondary electrons,** a conventional Everhart-Thornley (E-T) detector with an applied positive bias is the most common detector used for rapid imaging. The essential idea of this detector is based on converting the electrons to photons. Then, the photons are converted to an electric signal by a photo-multiplier tube.

The detector construction is shown in figure 3.5, it begins with a collector grid which is biased between -50 to +300 V, that collects the emitted SEs. Then the scintillator with an applied high bias ranging from 10-12 kV is used to accelerate the SEs. As electrons strike the scintillator, they are converted to photons which in turn strike the cathode of the photo-multiplier tube where they convert to an electric signal and are amplified by the photomultiplier by a factor on the order of 10^6. The resulting electric signal is proportional to the number of incident SEs on the scintillator. [80]

This detector will also detect BSE. In the case of BSEs, by applying a negative bias to the grid (~ - 50 eV), the SEs will be repelled and BSEs can be detected due to their high energy when the detector is located in their trajectory. In general, the (E-T) detector is placed at an inclined angle with respect to the sample surface as shown in figure 3.1. This position is not ideal for the BSE path; as a result, the detected fraction of BSE is very low and this detector is not efficient at detecting BSEs. Due to the applied positive voltage, the SEs can reach the detector even for a high tilted sample.

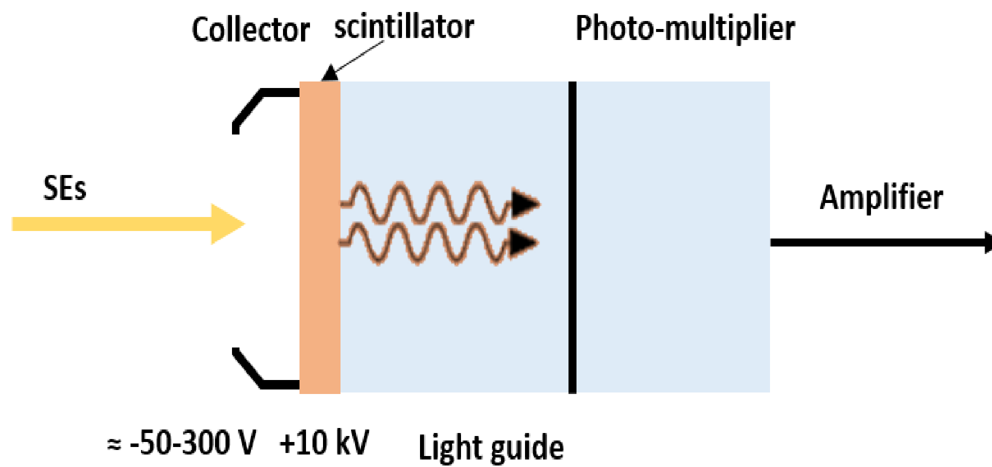

Figure 3. 5: Schematic of an E-T detector used to detect SEs

The primary detector used to detect BSEs is **the solid-state detector**. This type of detector does not require the collector grid as in the SE detection system. The detector is located directly above the sample (see figure 3.1) and consists of a doped semiconductor material (p-n junction diode), most commonly silicon. As the BSEs with certain energy E_{BSE} bombard the detector, the silicon electrons are excited, forming electron-hole pairs.

The number of generated electron-hole pairs n can be described with the following equation:

$$n = E_{BSE}/E_{exc}$$

The E_{exc} is the excitation energy (for silicon it is 3.6 eV). This equation clearly illustrates that the number of electron-hole pairs n is proportional to the E_{BSE} energy. Thus the generated signal from such a detector is more sensitive to high energy BSEs than those with low energy. Such a detector has a low energy threshold ranging between 1 keV- 3 keV so it is only able to detect high energy electrons and cannot be used to detect SEs. [83]

In the case of a highly tilted sample, the detector is mounted in front of the sample and collects what are referred to as forescattered electrons. In the present work this is the

primary geometry used, in particular where EBSD information is acquired simultaneously with the diffraction information (ECCI), from a forescattered detector placed beneath the EBSD detector. This work is demonstrated later in chapter 6.

3.2 Electron channelling contrast imaging (ECCI)

In order to characterize the defects in a sample, ECCI is used. Although transmission electron microscopy (TEM) is a reliable technique for imaging defects, it requires time-consuming sample preparation and can only be used to examine a small area of the sample. ECCI is an alternative technique to TEM for studying line and surface defects, where there is no need for sample preparation and a large area of the sample can be imaged.

ECCI was discovered by Coates in1967 [85, 86]. In ECCI, the incident beam penetrates down the crystal before being diffracted from lattice planes, this is described in more detail below. The utilization of this phenomenon for imaging defects in bulk materials was proposed by Booker et al [85]. The observation of a single defect had been achieved earlier in TEM by Hirsch's group in 1962 [86]. The first observation of dislocations in an SEM was made by Clarke in 1971[87]. To date, ECCI is used in a wide range of applications to characterize a variety of materials such as bulk materials [88-90] and thin films including GaN [87, 91, 92] GaP [93, 94] and SiC [95, 96].

Analogous to TEM, in ECCI the visibility depth of the beam varies from tens to hundreds of nanometres beneath the surface of a sample, depending on the material type, beam conditions and the reflection planes [85-87, 97]. The optimal spatial resolution achievable with this technique is on the order of tens of nanometres. The contrast in the ECCI micrograph is derived from the crystal structure, as discussed below. Any deviation in lattice orientations such as tilt or twist grain boundaries and single defects can be imaged and identified.

The electron behaves as a wave and a particle. The backscattered electron can be described as utilizing the wave nature of the electron. The Bloch wave, which is a standing wave can be used here. These waves are propagating through the top surface of a crystal as sets of plane waves. Two types of waves are considered and are referred to as wave-I and wave-II and are defined below. Both types' intensities significantly depend on the position of the lattice atoms. As seen in figure 3.6, wave-I has a

maximum intensity along the plane of atoms while the maximum intensity of wave-II is located between the lines of atoms. As a result, the probability of an electron of wave-I being diffracted is significant as it is located close to the atom. The interaction between the wave-II electrons and the lattice atoms is weak due to the separation distance. Therefore the probability of this type of wave being diffracted is weak. [98, 99] The simple model in figure 3.6 demonstrates that the probability of electrons being backscattered is dependent on the incident beam angle and the proximity of the primary beam to the atoms. Consider a case when the incident beam is travelling parallel to the lattice atoms, the yield of BSE is weak. Therefore, the intensity or the yield of BSEs can be varied as the incident beam angle or the orientation of the sample is changed, as seen in figure 3.7 (orange and green arrows).

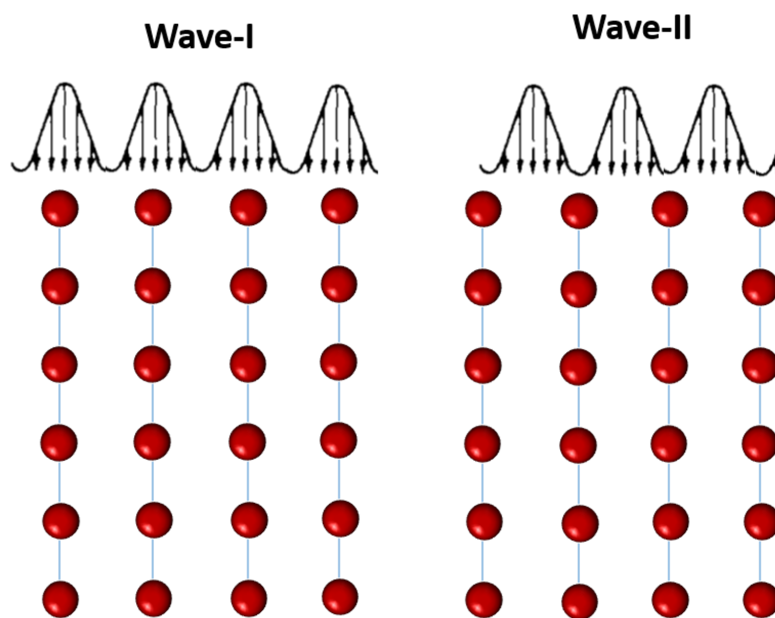

Figure 3. 6: The Bloch waves that are used to describe the behavior of the electron beam in respect to the lattice atoms. Wave-I has a maximum intensity in the atom plane while wave-II has a maximum intensity in between the plane of the atoms.

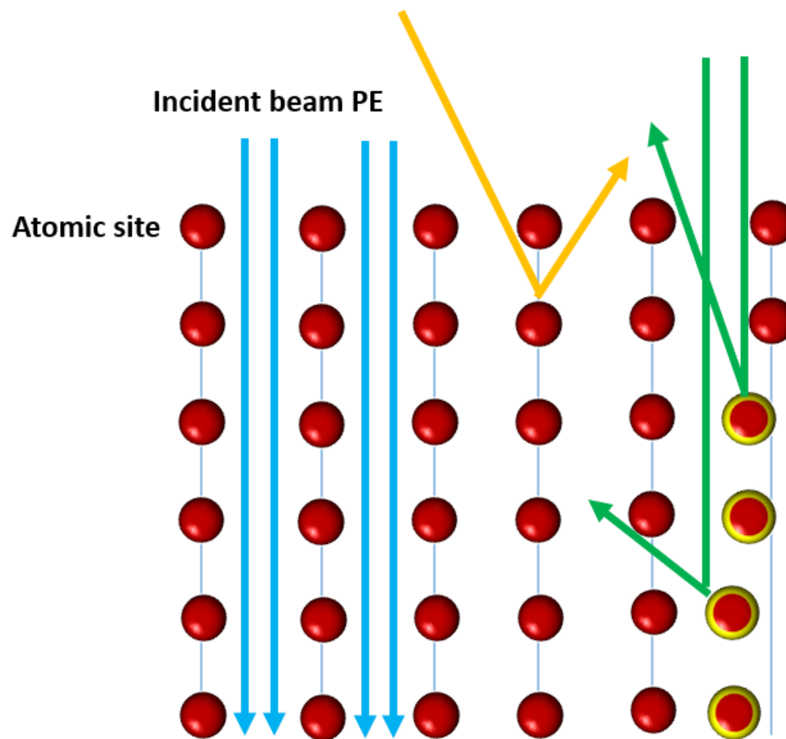

Figure 3. 7: The relationship between the incident beam angle and the atomic site as it related to the generation of BSE. Blue arrows indicate the condition where the incident beam is lined up with the crystal lattice, the orange arrow illustrates the case when the incident beam angle changes with respect to the lattice. The green arrow indicates the effect of a change of positions of atoms in the crystal with respect to the perfect lattice as might be produced by a defect.

Since the incident angle of the beam is constant, the sum of the Bloch intensities is constant. However, the ratio of intensities of wave- I and wave- II electrons can be changed and therefore the intensity of BSEs will also change. The intensity of BSEs will vary with the angle of the incident beam on the sample with respect to the atomic lattice structure.

Electron channelling contrast can be visualized in two modes; Electron channelling patterns (ECP) and the ECC imaging mode [83, 87, 100].

An electron channelling pattern (ECP) can be acquired when the SEM is operated at low magnification. As the beam scans across the sample surface, its angle relative to the crystal planes changes and the beam satisfies the Bragg condition for multiple crystal planes. Bragg's equation is defined as $2\, d\, sin\, \theta = \lambda$ where the λ is the electron wavelength and d the separation distance between the atomic planes and θ is the angle between the electron beam and the atomic planes. This leads to a change in the BSE signal as the beam is scanned over the sample (see further discussion below) and a number of overlapping planes (bands) are visible, superimposed on the image of the sample. This is known as an ECP. Figure 3.8.a illustrates this process, where the beam scans across the sample surface and its angle relative to the crystal planes changes, as does the intensity of BSE. Focusing on the area between points A and B in figure 3.8.b, this shows that a rapid change in the intensity of BSEs occurs close to the Bragg angle. When the angle of the incident beam θ is smaller than the Bragg angle θ_B ($\theta < \theta_B$) a small change in the angle of the beam with respect to the sample will result in a significant increase in the BSE intensity. Where the scanned beam angle θ is greater than the Bragg angle θ_B ($\theta > \theta_B$), a reduction in the BSE intensity occur.

Due to this, arrays of overlapping 2D bands can be acquired. Each band represents a set of atomic lattice planes and the angle between the bands corresponds to the angle between the corresponding lattice planes. The centre of the pattern is exactly the beam direction during the scan. Any distortion in the crystal can be predicted through the ECPs, as the distortion can deviate the planes from their original site. In other words, the symmetry of the crystal lattice planes is affected due to crystallographic defects which affect the acquired ECPs. ECPs thereby provides information about crystal orientation and phase identification.

In the case where defects exist in a crystal, for instance, a single dislocation, a distortion (bend) will be introduced into the surrounding planes. If the incident beam satisfies a Bragg condition for the undistorted set of planes, those planes distorted due to the presence of dislocations have a different Bragg angle, either greater or smaller ($\theta < \theta_B$ or $\theta > \theta_B$). As a result, the yield of BSE will be affected providing defect contrast. [85] This is the mechanism used to produce ECCI micrographs as discussed in the next section.

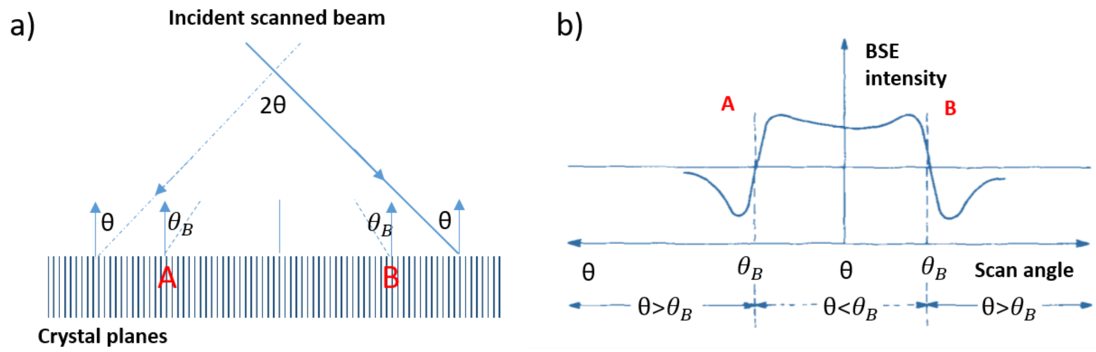

Figure 3. 8: a) The variation of the incident beam with respect to the crystal planes b) The backscattered intensity difference as the incident beam angle θ either greater or smaller to the Bragg angle θ_B. figures adapted from Joy et al. [98]

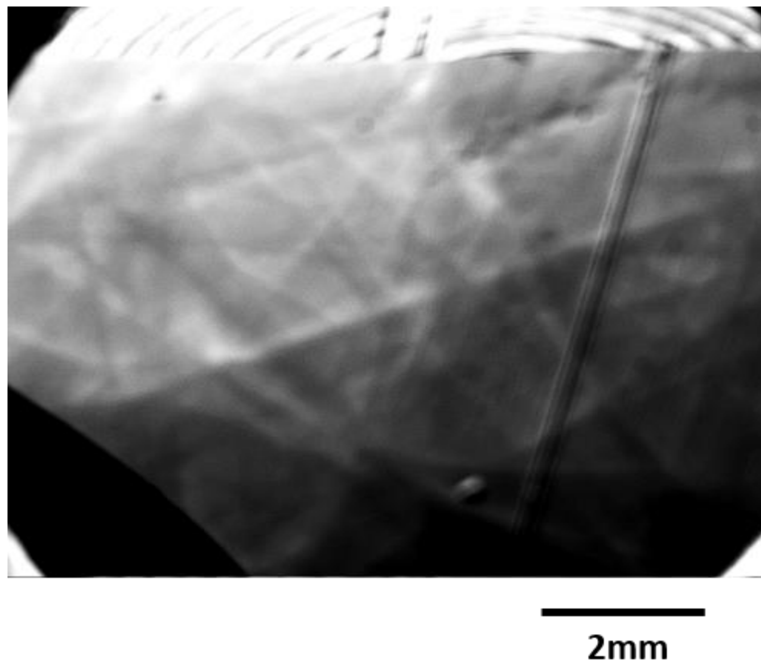

Figure 3. 9: ECPs from ELOG GaN demonstrate overlapping bands. This image was acquired at a tilt of 47° and an accelerating voltage of 30 keV.

Electron channelling contrast image (ECCI), the ECP can be used to set a Bragg condition, as discussed above, the centre of the pattern is exactly the beam direction during the scan and this can be set so that the incident beam is diffracted from a particular set of planes. To acquire an ECCI micrograph the SEM is operated at high magnification where the angle between the sample and the beam remains constant. Any distortion of the sample due to the presence of a dislocation will result in a deviation away from the Bragg condition leading to a change in the BSE intensity, revealing the dislocation.

ECCI geometry

The sample orientation with respect to a detector can be divided into two geometries; backscattered geometry and forescattered geometry, this classification depends on the orientation of the measurement, particularly the BSE detector position. In the backscattered geometry the detector, as was mentioned in section 3.1.2, is directly above the sample beneath the SEM pole pieces, the sample for this geometry is at or close to horizontal with respect to the incident beam (≈ 90° in respect to incident beam). While for the forescattered geometry the detector is located in front of the sample and in this case, the sample is tilted to between ≈30°-70°. Both geometries are illustrated in figure 3.10.

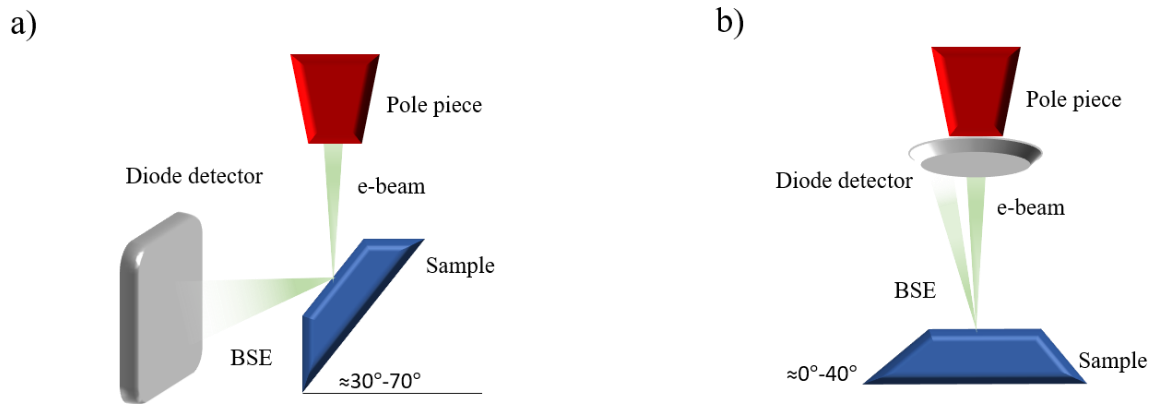

Figure 3. 10: Schematic of the ECCI experiment geometry a) is the forescattered geometry, b) is the backscattered geometry.

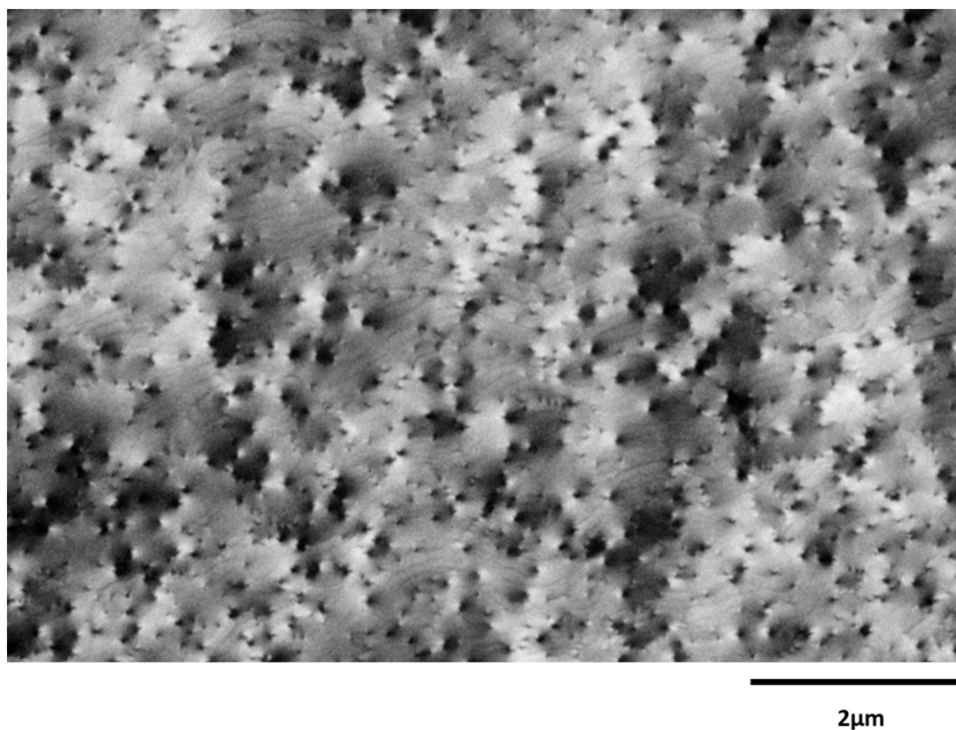

Figure 3. 11: ECCI micrograph from AlGaN thin film sample which shows various information from the crystal (grains, atomic steps, and threading dislocations). Threading dislocations (TD)s appear as black-white contrast. The image was acquired at an accelerating voltage of 30 keV and at a tilt 50° in the forescattered geometry.

The information from ECCI micrographs

The density of threading dislocations and their distribution in the sample can be obtained from an ECCI micrograph. An example ECCI is shown in figure 3.11. To characterize the defects (TDs) in wurtzite material, at least two ECCI micrographs should be acquired from the same area under different diffraction conditions to identify their types: edge (*a*-type), screw (*c*-type), or mixed ((*a* + *c)*- type). Note that the dislocations may only be described as edge and screw in wurtzite material when the dislocation line and Burgers vector are perpendicular and parallel to each other respectively. Dislocations appear in ECCI micrographs as dots with black-white contrast, as seen in figure 3.11. Analogous to the TEM technique, it is possible to use the invisibility criterions ***g.b*** and ***g.b*×*u*** to recognize TDs types. The diffraction vector ***g*** can be acquired from ECPs; hence one can estimate that when ***b*** is parallel to ***g*** the outcome of ***g.b*** is maximized and minimized in the case when ***b*** and ***g*** are orthogonal to each other. In the case of c-plane III-nitrides for a plan view imaging (ECCI or plane view -TEM), (0002) and ($11\bar{2}0$) cannot be used to discriminate between the edge, screw and mixed threading dislocations. Instead of that it can satisfy ***g.b*** = 0 for dislocations with a Burger vector of $\frac{1}{3}$ <$11\bar{2}0$> by selecting a ***g*** vector of ($1\bar{1}00$) hence a significant reduction in the intensity of a proportion of the *a*-type TDs (edge dislocations). In the case of in plan view imaging, a screw dislocation (*c*-type TDs) where ***b*** = <0001> at the ***g*** vector of ($11\bar{2}0$) and ($1\bar{1}00$) will not meet the invisibility criteria for *c*-type (screw) as a further factor which needs to be taken into account when attempting to apply the invisibility criteria to ECCI micrographs (and plan view-TEM images), is the effect of surface relaxation on the observed defect contrast. The variation in strain due to surface relaxation around a defect can dominate the observed defect contrast. The mixed dislocations ((*a* + *c)*- type) is visible under these two diffraction conditions. [101, 102] The image in figure 3.12 acquired under diffraction condition where the edge dislocations have the weaker contrast (yellow circles) in compare to the dislocations with screw component (pink circles).

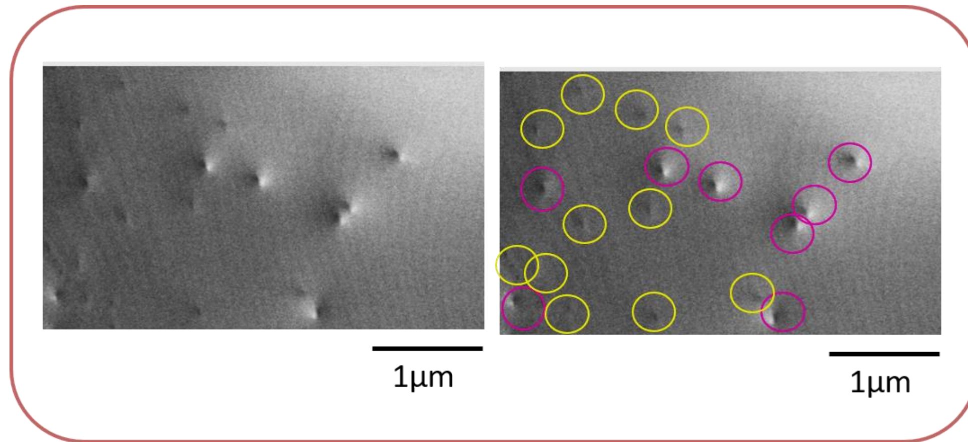

Figure 3. 12: ECCI micrograph at diffraction condition where the edge have the weaker contrast in contrary to the screw component dislocations. The yellow circles are the edge dislocation where the pink circles are related to the screw component dislocations. The image acquired from the ELOG GaN sample from chapter 4.

For nitride semiconductor thin films, additional strategies have been developed to identify the TDs. By tracking the change in the black-white contrast under different diffraction conditions, dislocations types can be recognized. Figure 3.13 demonstrates the ECCI standard method of TD identification by tracking the change in the dislocation black-white contrast direction under two diffraction conditions, figure 3.13.a and b are the images of the same area at the first and the second diffraction condition respectively. In the case of the of edge dislocation, the black-white contrast either remains the same or flips (black-white contrast reversed), see yellow arrows in figure 3.13. While in the case of *c*-type/ (a + c)- type (dislocations with screw components), the contrast changes in other directions, see the green arrows in figure 3.13. In the case of inclined dislocations, this method does not work as will be discussed in chapter 4 and other strategies for identifying dislocations are required.
In addition, if a diffraction condition is selected so that atomic steps are observed in the ECCI micrograph it is possible to identify TDs by applying a technique developed for AFM. [103, 104] TDs are identified as screw (*c*-type) or mixed ((a+c)- type) if the TDs terminate at a step or as *a*-type if they are located on a step.

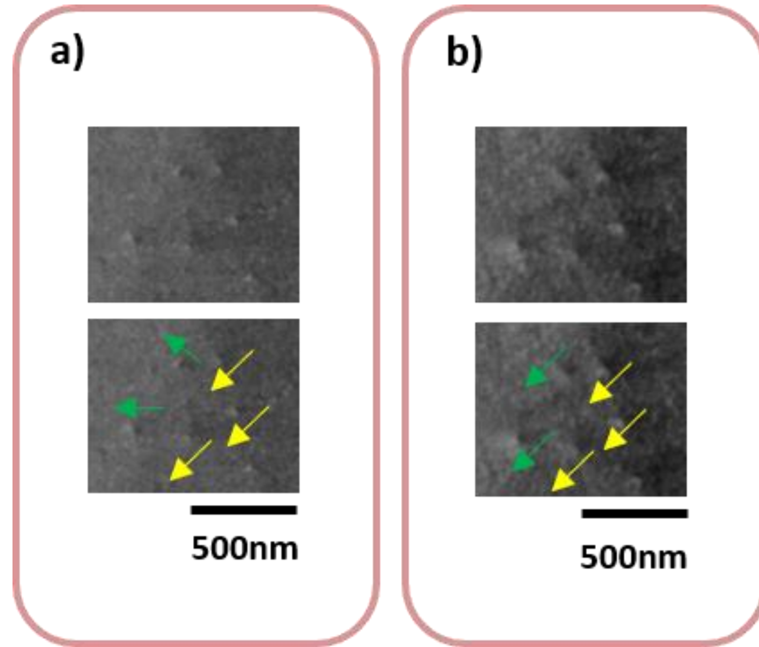

Figure 3. 13: Illustrating the standard ECCI method that is used to classify TDs, a) shows the first diffraction condition where the arrows in the bottom image indicate the black-white contrast direction (yellow arrows for edge dislocation, green arrows for screw component dislocations) b) shows the second diffraction condition from the same area where the bottom image is the same image including the arrows that indicate the black-white contrast direction (yellow= edge, green= screw component dislocations). The dislocation images are extracted from a larger image acquired from AlN thin film sample (sample A in chapter 6).

In addition to dislocation type, grains, sub-grains, stacking faults and atomic steps can be revealed using ECCI.[105] The ECCI micrograph in figure 3.11 illustrates atomic steps, TDs as black-white spots and some sub-grains (where the term sub-grain is used to refer to a region which has a different orientation with respect to neighbouring regions but this misorientation is of order a degree or less). In figure 3.11 sub-grains are observed to be surrounded by dislocations. The difference in the orientations of sub-grains, in relation to the incident beam, makes them visible. Differences are observed in the grey scale for different sub-grain orientations.

ECCI can be used in conjunction with other techniques which provide complementary information. It can be used with cathodoluminescence CL to study the effect of the TDs on the light emission as in references [74, 87, 105, 106]. It can also be used with AFM, as shown in chapter 4, where AFM images are compared to ECCI micrographs to determine if all dislocations are imaged in ECCI. Moreover, AFM is used with EBSD to study the orientation of grains and strain [88, 90, 105, 107]. In chapter 6 ECCI is used in conjunction with EBSD to study TDs and grain boundaries.

3.3 Electron backscattered diffraction (EBSD)

Electron backscattered diffraction (EBSD) in the scanning electron microscope is used to acquire quantitative microstructural information from single or polycrystalline materials at different magnifications, ranging from the millimetre to the nanometre scale (bulk samples, thin films, and nano-materials). The information obtainable via this technique includes; crystal orientation and the distribution of crystal orientations (texture), crystal structure, grain boundary types, strain, as summarised in Table 3.1. EBSD is capable of providing information with high spatial resolution on the order of tens of nm.[108] Thus, EBSD is an attractive technique that is utilised widely for material characterisation in a diverse range of fields, e. g. aerospace, metal research, earth science, and semiconductors.

As the electron beam is scanned across a crystal sample in a raster fashion, orientation maps can be produced which allow identification of the orientation of each point in the crystal for which an electron backscatter pattern (EBSP) is acquired. Figure 3.13 is a schematic illustration of an EBSD map where the different colours represent the different orientations of the crystal grains. [90, 108-110]

EBSD may be combined with other analytical techniques in the scanning electron microscope, for example, ECCI, CL and EDS. ECCI is the preferable technique in the case of measuring the density of dislocations and their types. However, an ECCI micrograph exhibits sub-grain misorientation as a variation in contrast, but does not provide any quantitative information (e.g. the direction of misorientation or magnitude); whereas the EBSD technique can provide this information.[105] When EBSD is combined with CL it is possible to compare the luminescence properties of a

crystal to its structural properties.[105] EBSD maps can be acquired simultaneously with EDS maps for phase identification by correlating crystallographic information with chemical composition. This is illustrated by the work of Laigo et al. [111] where they studied a series of complex alloys (Fe–35Ni–25Cr–0.4C–1Nb) which contain several carbide phases (e.g. niobium-rich carbides (NbC), and chromium-rich carbides ($Cr_{23}C_6$ and Cr_7C_3)). EDS was unable to discriminate between ($Cr_{23}C_6$ and Cr_7C_3) phases, however these phases have different crystal structure, EBSD can discriminate between the phases. [111]

EBSD information	Description	References
Grain orientation and texture	EBSD is capable of identifying a grain's orientation, its size, and the magnitude of the misorientation with other grains/or with a reference orientation. The distribution of crystal orientations in a polycrystalline material is often referred to as its texture.	[105, 112, 113]
Grain boundary type	EBSD is able to provide a statistical information on grain boundaries types; low angle and high angle boundaries	[114]
Phase identification	EBSD may be utilised to identify different crystal structures in polycrystalline materials	[115, 116]

	as each crystal structure of a material has a unique EBSP.	
Strain	EBSD is capable of resolving the deviation in a pattern with strain as small as ≈ 10^{-4} based on EBSPs analysed through applying a cross-correlation approach.	[117-119]
Defect (dislocations)	By using the cross-correlation approach, EBSD provides accurate measurements of the misorientation and strain, thus, the density and the types of the geometrically necessary dislocations (GND) can be obtained.	[113, 118, 120]

Table 3. 1: Summarizing the information that is provided by EBSD and brief descriptions

The formation of electron backscatter patterns (EBSPs)

In EBSD, patterns similar to ECPs (i.e., containing Kikuchi bands are recorded, and are referred to as electron backscatter patterns (EBSPs). The formation mechanism of EBSPs differs to that of ECPs. Obtaining an EBSP experimentally, starts when the incident electron beam enters the highly tilted crystal and the electrons undergo inelastic scattering by the lattice planes. On exiting the crystal some BSEs may fulfil Bragg's law. This leads to the formation of pairs of diffraction cones (Kossel cones) as a result of diffraction from different planes in the crystal. In EBSD these cones intersect with a phosphor screen and are therefore observed as a pair of parallel straight lines (Kikuchi bands). As EBSD patterns provide information about the crystallography and crystal orientation, thus any change in the sample geometry (rotation or tilt) will lead to change in the pattern either as due to rotation or a shift in the pattern. [88, 121]

The experimental EBSD geometry

In order to study the microstructure of a crystal using EBSD, a highly tilted sample is required (≈70°). A fluorescent (phosphor) screen is placed in front of the sample which lights up as BSEs strike it, forming Kikuchi patterns. A camera is coupled to the screen to record the patterns. The camera is connected to the computer where the patterns are indexed. The high sample-tilt geometry was proposed by Alam et al. in 1954 as they discovered that the pattern is much clearer in the case of the high tilted sample as the BSE yield is dependent on the angle of the sample, the higher angle means more BSEs. Figure 3.14 shows the high tilted geometry of the EBSD experiment schematically. As is clear, the sample is placed at a high tilt of 70° in respect to the stationary incident electrons beam, to ensure a high yield of BSE. Solid state detectors are also usually placed around the screen to detect BSEs in the forescatterd geometry.

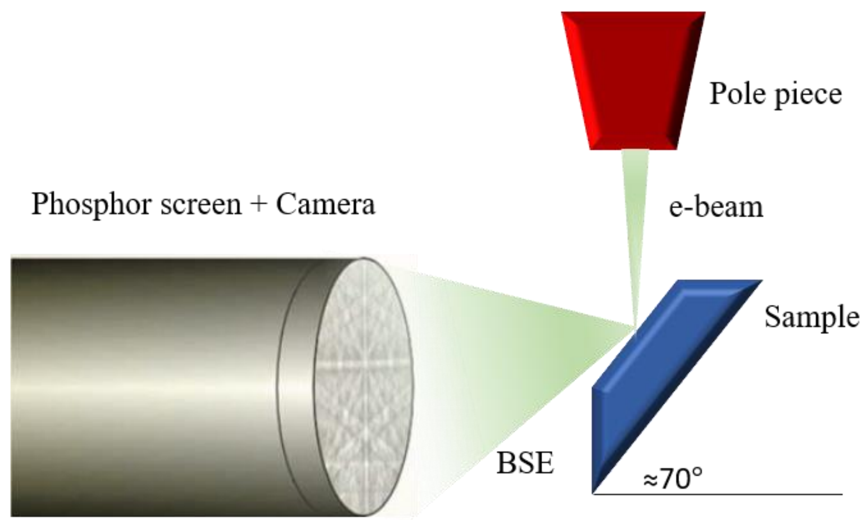

Figure 3. 14: Schematic of the EBSD setup

3.4 Atomic force microscope (AFM)

AFM is a versatile instrument that is used to generate high-resolution, rapid and non-destructive, 3-D nanoscale topographic images. The AFM was invented by Binnig et. al. in 1986 [122]. This invention was as an adaptation of the scanning tunnelling microscope (STM). The AFM can be combined with other techniques to study the properties of materials, for example the relationship between topographic features and, structural properties and light emission.

AFM setup

The main parts for any standard AFM are listed below (see figures 3.15):

i. A fine tip that is mounted to a flexible cantilever spring. Both parts are commonly fabricated from Si, SiN, or diamond. The cantilever size is a few micrometres, the diameter of the tip apex can be as small as 4 nm. As the tip scans over the sample surface, the cantilever will bend either up or down with respect to high or low features on the sample respectively.

ii. A piezoelectric scanner is used to control the movement of the tip in the z direction (up and down) or in the x and y directions.

iii. A detection system which contains: a quadrant photodiode detector and laser beam, that is reflected from the back of the cantilever onto the detector to track its deflections. The surface topography of the sample influences the bending of the cantilever which is tracked by the laser beam. Any deflection in the cantilever that causes a change of the position of the reflected laser beam on the PSD. The electrical signal from the photodiode detector is used monitor the position of the cantilever. A feedback loop is associated with the photodiode and the scanner to control the height of the tip above the sample thus accurate AFM maps are acquired. See figure 3 which shows a schematic of a standard AFM.

Tip–Sample Interaction

The tip-sample interaction is key to the operation of the AFM. The forces at the atomic level are Van der Wals force (attractive) and the electrostatic force (repulsive) and follow Hook's law $F=-kZ$, as the cantilever here acts as a spring. The spring constant k and the distance between the probe and the surface Z play a crucial rule in this process. Both forces depend on the distance between the tip and the sample. For simplicity see figure 3.16 which demonstrates the relationship between the separation distance between the sample and the tip versus the force. From the right side of the plot, the force is attractive as the tip is away from the sample. When the tip is very close to the sample, a repulsive force will result as the electron cloud of the atoms of the tip and sample repel each other. One can observe that the curve in the case of the attractive force changes gradually while it is very steep in the case of the repulsive force.

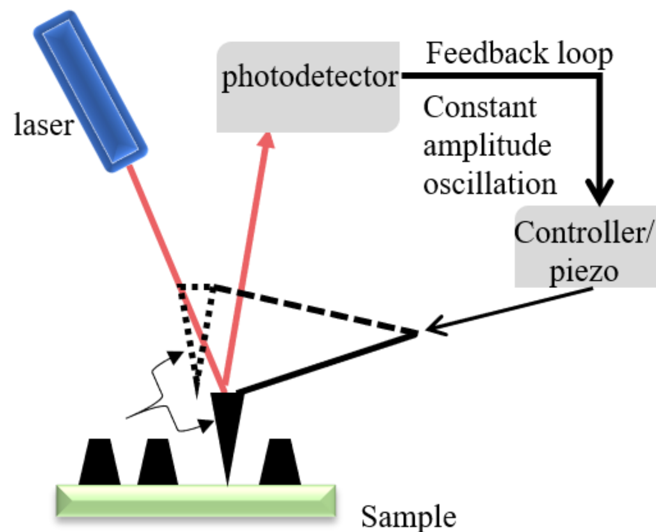

Figure 3. 15: Schematic of an AFM setup adapted from [122].

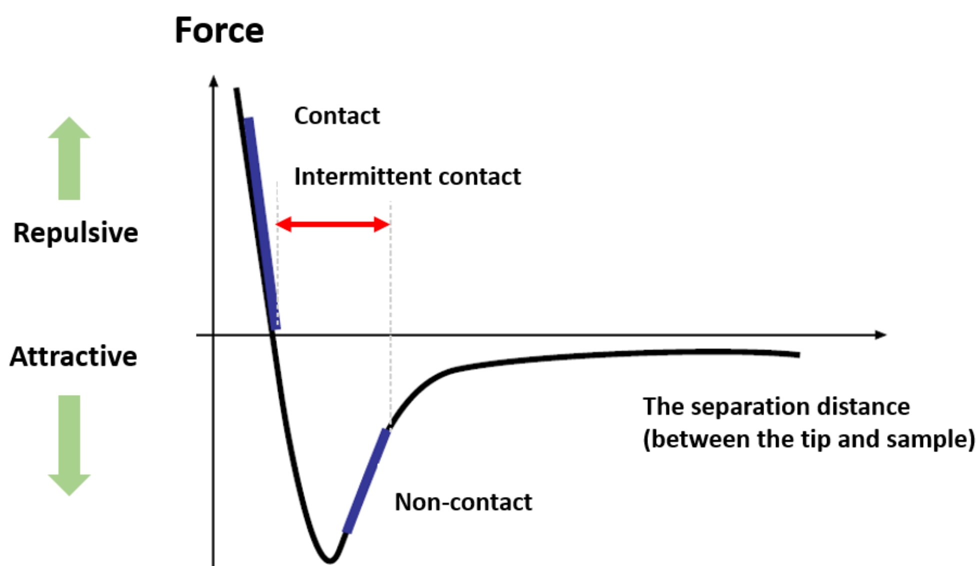

Figure 3. 16: A plot of the forces between the tip and the sample as a distance-dependent interaction adapted from Maghsoudy-Louyeh et al. [122]

AFM operating modes

The most common operating modes of the AFM are contact mode, non-contact mode, and tapping mode (intermittent contact mode): [122-124]

In contact mode the tip is scanned close to the sample surface which results in a strong repulsive force between the tip and the sample. The generated force causes the cantilever to bend as it scans across the sample surface. In this mode the sample can be damaged as a result of direct contact with the AFM tip. In addition, the tip can be damaged in this mode, effecting the image quality. The tip is often damaged and must be replaced often. However, this mode can provide a high resolution measurements on the order of sub-nanometre.

In non-contact mode, the cantilever oscillates above the sample during the scan with no contact between the tip and the sample. The oscillation amplitude (and deviation from the cantilever's resonant frequency) changes with distance between the tip and the sample as a result of variation in the attractive force between the tip and the sample.

In this mode the sample surface and the tip are protected from damage. This makes it an effective mode to investigate very thin or biological samples. However, it provides lower resolution images. The lifetime of the tips in this mode is longer than in other modes.

Tapping mode (which was used in this thesis) combines the advantages of both contact and non-contact modes. The separation distance between the tip and the sample surface is intermediate between that used in contact and non-contact modes. The tip oscillates above the sample and tracks the topography by lightly tapping the surface for a short time. As the tip approaches the sample the reduction in the tip oscillation amplitude can be measured thus mapping the sample topography.

TDs determination by AFM

In this thesis, specifically in chapter 4, AFM is used to estimate TD density and identify dislocation types. The results obtained with AFM are combined with ECCI to investigate the behavior of TDs.

Previous studies of dislocations in the AFM include the work of Watkins et. al. [125] who used the AFM to study dislocation structure and surface morphology of InAs and GaSb samples. AFM is also widely used to investigate TDs as well as the surface features of III-nitride thin films samples such as GaN [126] and AlGaN [127] thin films. Tian et. al. [128] used a number of different microscopes to investigate dislocations in GaN samples. The SEM was used to study the distribution of pits in the samples, while AFM was used to identify the size and shape of the pits. TEM was then used to confirm the dislocation types and CL was used to estimate the dislocation density.

TDs create small pits when they terminate at the sample surface and this change in topography can be imaged by AFM. Preliminary surface treatment is required to ensure that all pits are detected.[103] This can be either performed in-situ during or immediately after growth using SiH_4 and NH_3 [74, 129] or ex-situ [130] to extend the pits.

From an AFM image, TD type is determined by the location of TDs as related to a step and the size of the pits. If a TD terminates on a step then it is a *c*-type/ (*a*+*c*)-type

(screw or mixed) dislocation (see the red circle in figure 3.17.a) whereas, if a TD is located on a step it is an *a*-type (pure edge) dislocation (see the green circle in figure 3.17.a). The differences in magnitude of the Burgers vectors between the *a*-type and *c*-type dislocations leads to different sizes of pits. [19] Also, 'in depth' analyses are used to identify TDs. The shallower dislocations indicate an *a*-type, whereas the deeper ones indicate *c*-type/ (*a*+*c*)-type dislocations, see figure 3.17.b [20, 21]

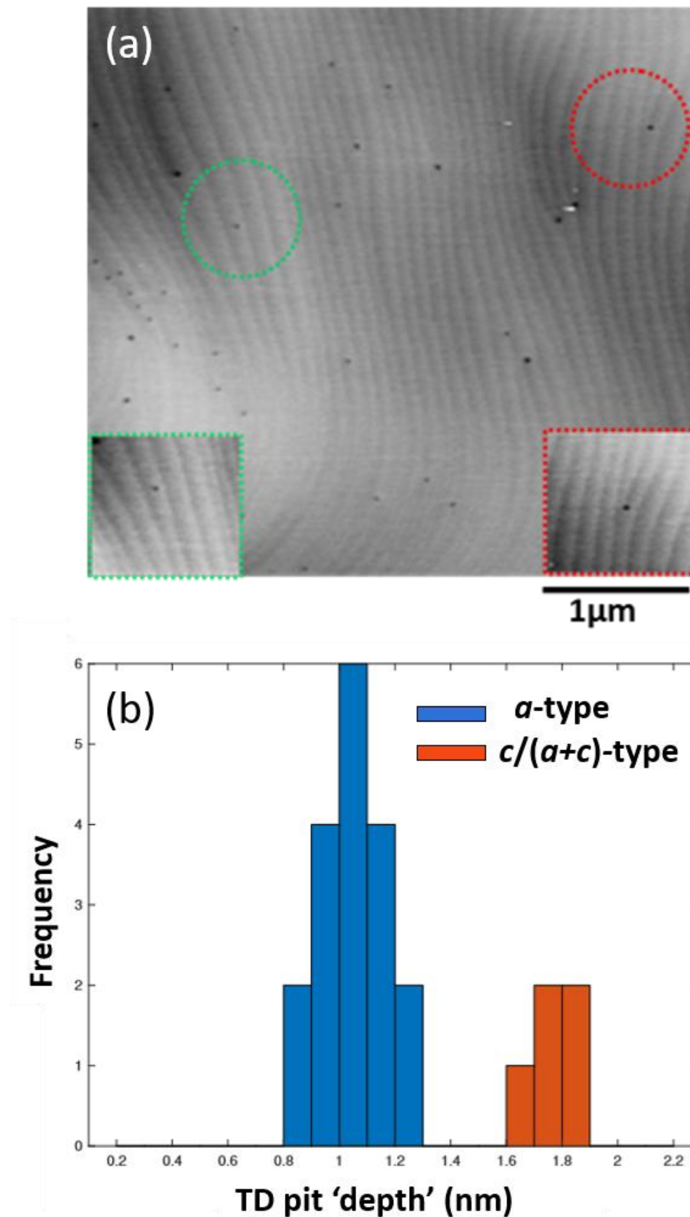

Figure 3. 17: a) Demonstrating the method used for TDs identification in an AFM image (the red circle and inserted magnified image in the red box show a c/(a+c)-type dislocation terminating a step, the green circle and inserted magnified image green box is a-type dislocations located on the step. c/(a+c)-type dislocation (red box) is larger in size comparing to a-type dislocations (green box). b) Histograms from AFM measurements of TD pits depth and step edge terminations, the blue bar is a-type dislocations where the orange one is for c/(a+c)-type dislocation. This data is from ELOG GaN sample which is studied in chapter 4.

Chapter 4

Coincident ECCI and AFM of threading dislocations in ELOG GaN

In this chapter, the correlation of electron channelling contrast imaging (ECCI) in a scanning electron microscope is correlated with atomic force microscopy (AFM) to reveal and identify threading dislocations (TDs) in an epitaxially laterally overgrown GaN (ELOG), 17 μm-thick sample. The main aim is to demonstrate that all TDs detected by AFM can be also resolved by ECCI, the imaging of inclined dislocations with ECCI is also explored.

4.1 Introduction:

In the last decades, there has been a spectacular revolution driven by the III-nitride semiconductors, specifically GaN and its alloys, in the solid-state lighting industry with blue LEDs being the key component in white LED light bulbs. In addition to lighting, GaN and its alloys are also being exploited in the manufacture of UV photodiodes and high–speed/high–power electronic devices.[131, 132]
As mentioned previously in 2.2.3, the growth of GaN on a foreign substrate (Al_2O_3, SiC or Si) leads to a detrimental high density of TDs. Consequently, the efficiency of the devices will be affected.[133] Continuous research efforts have been made on improving the semiconductor growth through the use of various growth techniques such as metal-organic vapour phase epitaxy (MOVPE), hydride phase epitaxy (HVPE), liquid phase epitaxy (LPE), molecular beam epitaxy (MBE) and atomic layer deposition (ALD).[134] Among the aforementioned growth techniques, MOVPE is one of the widely used methods for producing large area, high crystalline quality wafers, see 2.2.1. Novel defect reduction techniques such as epitaxial lateral overgrowth (ELOG) have also been developed to reduce defect densities [135, 136], a brief description on this TDs reduction method can be found in section 2.4. It has been

possible to obtain longer device lifetimes and superior performance through these improvements in growth [137].

As discussed in section 2.2.1, the ELOG structure studied in the present work comprises overgrowth over stripes of SiO_2 (wing regions), where the growth initiates through open (window) regions between the stripes of SiO_2. TDs under the SiO_2 mask cannot propagate to the surface, while those located in the window regions close to the edge of the mask will bend toward the mask into the wing region, thus producing inclined dislocations which thread at an angle from the surface normal. [136, 138] Ideally, the inclined dislocations located in the wing region interact and annihilate each other. [104]

To image and count dislocations and determine their character, rapid, non-destructive and statistically reliable methods are required. In this present work, I report the application of coincident electron channelling contrast imaging (ECCI) using a scanning electron microscope (SEM) (see section 3.2) and atomic force microscopy (AFM) in tapping mode (see section 3.4) to investigate dislocations in the ELOG-GaN. [87, 103, 139] Combination of these two techniques is a powerful structural characterisation tool for studying extend defects and surface in semiconductors and other material systems.

4.2 The sample fabrication:

The GaN sample used in this correlated study to compare AFM and ECCI techniques was grown by a two-step epitaxial lateral overgrowth (ELOG) process (discussed previously in section 2.4), and the growth was done in a metal-organic vapour phase epitaxy (MOVPE) reactor.

The sample growth began with a 1 μm highly resistive seed layer of GaN. Then a 100 nm layer of SiO_2 was deposited as a mask. The mask was patterned, using etching with stripes parallel to the $[1\bar{1}00]$ GaN direction so that both the wing and the window had equal widths of 5μm (see figure 4.1.a and b). The growth is completed in two stages of different V/III ratio. First, the formation of pyramidal stripes was achieved at a comparatively low temperature of 970°C. In the second stage, coalescence was

achieved at a high temperature of 1050°C (see figure 4.1.a). As a result, the lateral epitaxial overgrowth extends over the mask through the opening area. The final thickness of the GaN layer was 17 µm. Finally, a surface treatment by silane (SiH_4) is applied to increase the pits' size to assist the identification of TDs by AFM.

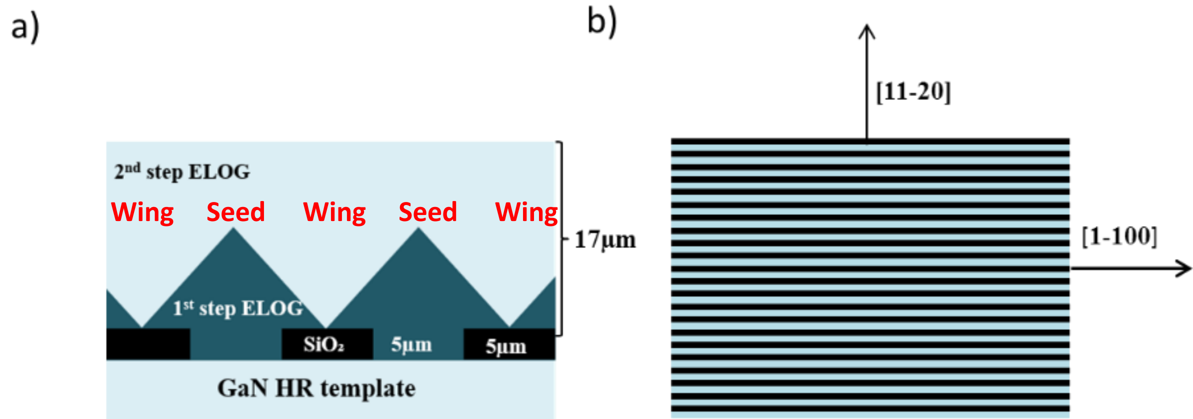

Figure 4. 1: a) Schematic diagram illustrating the growth stages of ELOG, the wing and seed regions are shown, b) Schematic diagram of surface of ELOG showing the direction of the stripes relative to the [$1\bar{1}00$] and [$11\bar{2}0$] directions.

4.3 The experimental methods

An FEI Sirion 200 Schottky FEG–SEM was used, operating at 30 kV, with forescatter Si diodes and an amplifiers provided by KE Developments Ltd. (now Deben, UK). AFM measurements were taken on a Veeco Dimension 3100 microscope in intermittent contact/ tapping mode, using a nanoscope V controller.

To avoid tip damage during the fast scan or the loss of information, the sample was aligned so that the angle between atomic steps (which were in general perpendicular to the mask stripes) and the scan direction was 45 degrees. This alignment allowed both wing and window regions to be imaging.

To identify TDs types in the large AFM image, PITS software developed by David Holec [50] was used to identify TDs based on the pit's size, depth and position in relation to the atomic steps. All AFM results and data were provided by Dr. Thomas

O'Hanlon [140] and Prof. Rachel Oliver, Department of Materials Science and Metallurgy, University of Cambridge.

4.4 Results and discussion

4.4.1 The AFM result

Figure 4.2 shows a large AFM image of a 30×30 μm^2 area. AFM measurements were performed first, followed by ECCI. From this AFM image, the average density of TDs in the seed region was found to be $5.0 \pm 0.2 \times 10^8$ cm^{-2} while in the wing region it is $1.3 \pm 0.1 \times 10^8$ cm^{-2}. The average density of TDs across the sample was estimated to be 3×10^8 cm^{-2} . The image shows the variation of TDs between wing and seed region and the atomic steps which were crucial in terms of TDs identification.

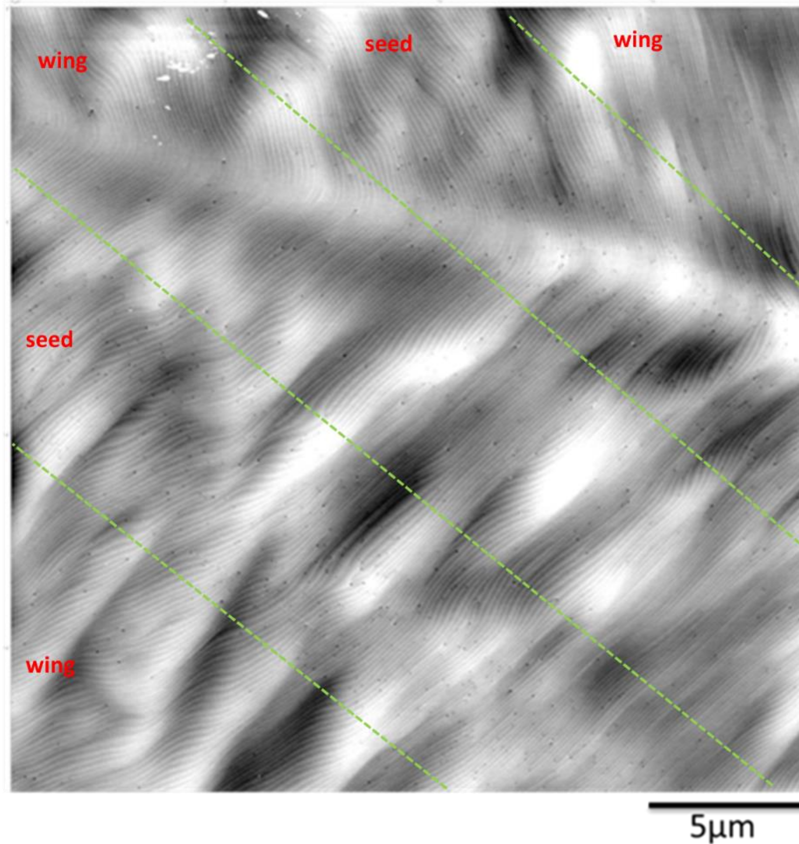

Figure 4. 2: Large AFM image showing a number of wing and seed regions. The approximate locations of the seed and wing regions are indicated and have an equal width of 5 µm.

4.4.2 The ECCI result

An image obtained with ECCI is shown in figure 4.3, the change in the density of TDs between wing and seed regions can be clearly seen. As shown in the figure 4.3, the wing region shows a reduction in the density of TDs comparing to the seed region. One can see the wing on the right has a larger density of TDs compared to the left wing. In addition, TDs align at the coalescence line in the middle of the right wing (inside red box). The TDs along the coalescence line exhibit a black-white contrast approximately perpendicular to coalescence line which is consistent with these being edge TDs along a low angle grain boundary.[37]

Using ECCI, the average density of TDs in the seed region is $4.2 \pm 0.7\times10^8$ cm^{-2} while in the wing region it is $1.3 \pm 0.1\times10^8$ cm^{-2}. These results were obtained by using the average of TDs from three images obtained from three different areas of 25 μm^2 for each region and from random parts of the sample and are consistent with the TD densities determined with AFM.

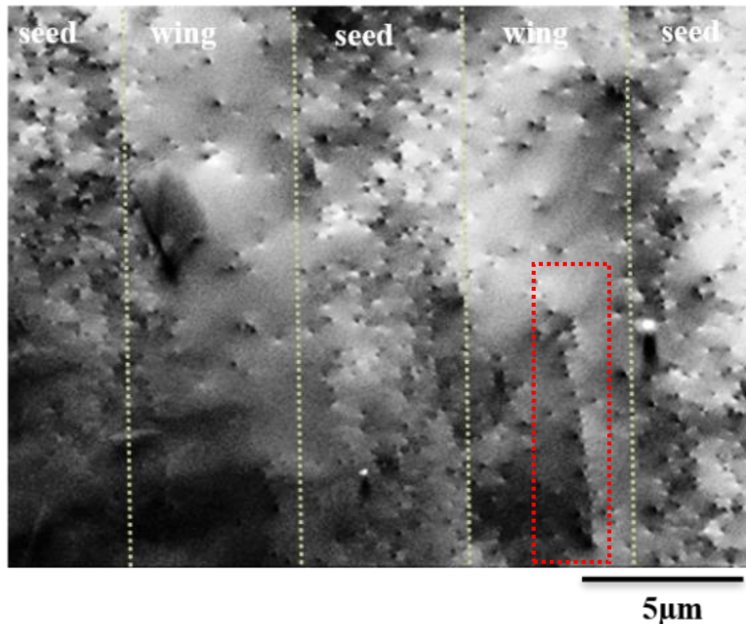

Figure 4. 3: Large ECCI micrograph showing a number of wing and seed regions. The approximate location of the seed and wing regions are indicated and have an equal width of 5 μm. Red box in the right wing include array of TD that align up at the coalescence line.

A closer look at a coalescence boundary can be seen in figure 4.4. Along the boundary there an array of dislocations at the coalescence line in the middle of the wing region. The intensity on opposite sides of the coalescence boundary are different, indicating a difference in orientation of the film on either side of the boundary line. The TDs on the coalescence line are not exhibiting the standard dipole black-white contrast more usually observed [87], instead they exhibit a contrast similar to simulations of the contrast for edge dislocations described by Picard et al. [101] (see inserted image in figure 4.4) in a $SrTiO_3$ foil, and are therefore likely to be edge type dislocations.

Figure 4.5.a demonstrates the variation in intensity across an ECCI micrograph along the dotted arrow, over a number of ELOG periods, where the change in the intensity over the ELOG sample is related to changes in orientation across the sample. This is likely to be due to an out of plane rotation about an axis parallel to the SiO_2 stripes. A similar variation in the intensity in an ECCI micrograph was observed by Trager-Cowan et al. [92] for an ELOG GaN sample, an out of plane rotation was confirmed by EBSD measurements.

The graph in figure 4.5.b is the first derivative of the intensity profile which shows the greatest difference in the intensity obtained over the ECCI micrograph. It is clear from this intensity profile that the greatest changes in the intensity are located at the coalescence line in the middle of the wing and in the middle of the seed region.

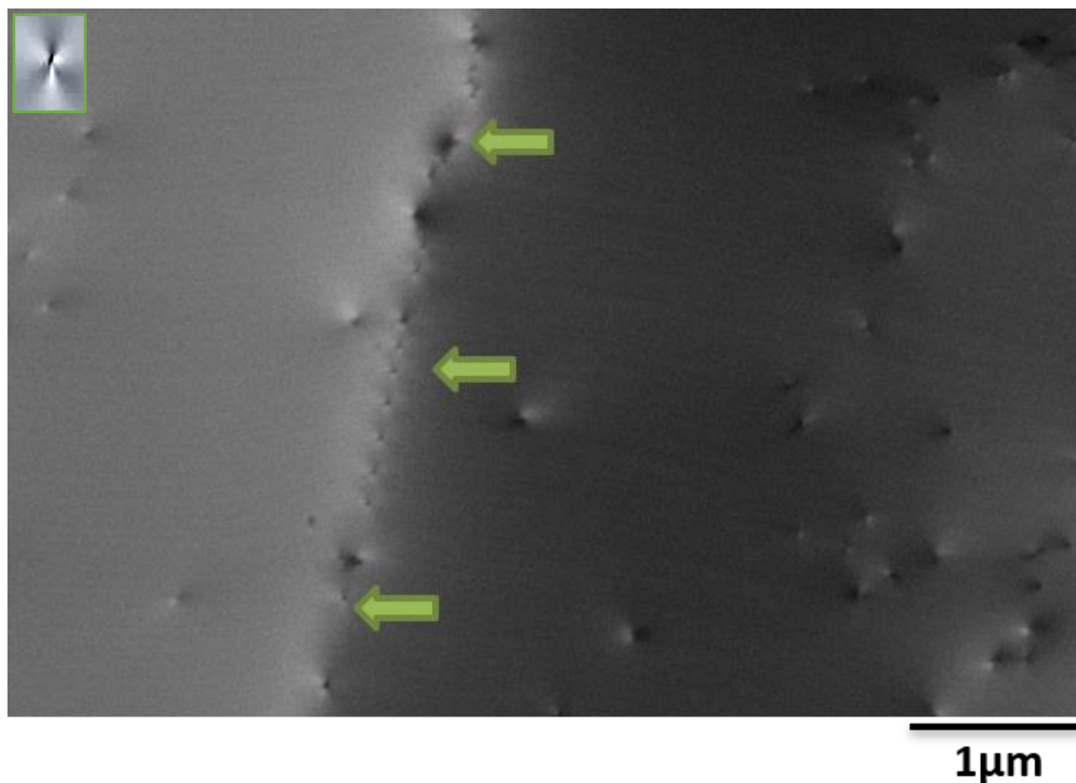

Figure 4. 4: Enlarged ECCI micrograph of the coalescence line at the middle of the wing region the green arrows indicate to the array of dislocations that set at the boundary. The inserted simulated dislocation image is from Picard et al [101].

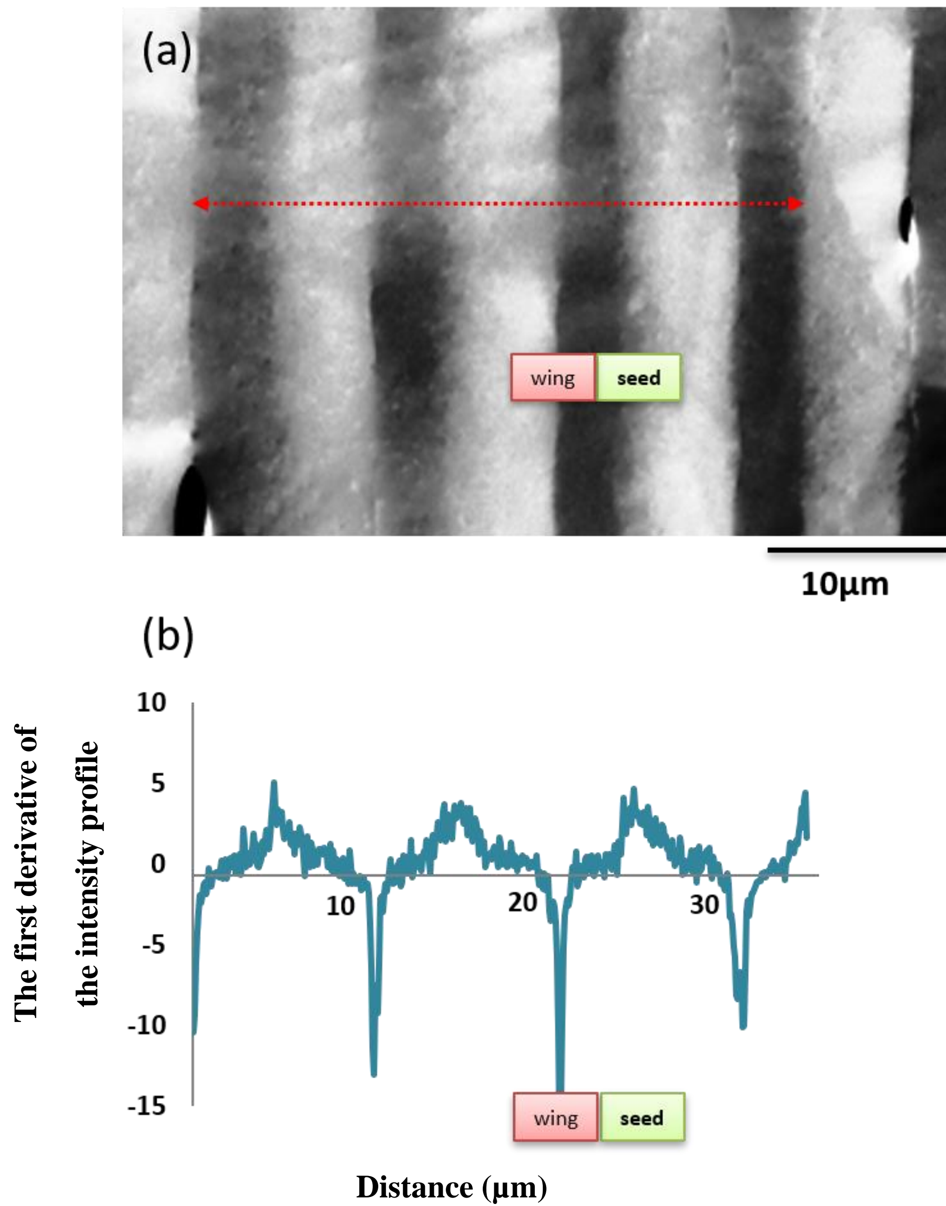

Figure 4. 5: a) ECCI micrograph demonstrating the deviation in the grayscale across large area of the sample (parallel of dark and bright stripes) b) the first derivative of the intensity profile across the ECCI micrograph (Note that it is horizontally aligned with the ECCI micrograph).

4.5 Coincident ECCI and AFM measurements

In the case of correlating the ECCI and AFM techniques, surface features (e.g. voids, contamination, etc) were used to identify the same area of the sample with both techniques. AFM measurements were performed followed by ECCI. AFM and correlated ECCI micrographs were used to analyse 130 TDs from both the seed and wing regions. Figure 4.6 shows images acquired from the same area of a seed region by both techniques. There is a one to one correlation of dislocations revealed independently by AFM and ECCI. The results from ECCI and AFM complement each other and confirm the presence of 51 near vertical TDs which are either pure edge or contain a screw component, i.e., they are either pure screw or mixed TDs. However, 72 TDs exhibit anomalous contrast in the ECCI micrographs, see for example the TD highlighted by the white box in figure 4.6.b. We attribute the observed elongated contrast to these TDs being inclined with respect to the c-axis. The small lines in ECCI micrographs correspond to the projection of inclined dislocations lines within the interaction probe depth.[141] When TDs thread at an angle to the surface of the sample, while under some diffraction conditions they are observed as dots exhibiting black-white contrast, for other diffraction conditions they may appear as short line segments. In addition, for diffraction conditions where they are observed as dots, the direction of the black-white contrast will be influenced by the inclination direction. The appearance of an inclined TD will depend on its inclination angle, the penetration depth of the electron beam and the diffraction condition. For a given material, the penetration depth depends on the electron beam energy and the diffraction condition. For an inclined dislocation, on changing the diffraction condition, any black-white contrast direction observed for these TDs will generally change by an angle other than 0° or 180° and it is not possible to deduce the Burgers vector of these dislocations from observation of the black-white contrast direction for different diffraction conditions. However it was possible to differentiate between TDs with a Burgers vector of $\frac{1}{3}<11\bar{2}0>$ and those with a Burgers vector of <0001> or $\frac{1}{3}<11\bar{2}3>$ from the relative contrast they exhibited under an appropriate diffraction condition. Under some diffraction conditions TDs with a Burgers vector of <0001> or $\frac{1}{3}<11\bar{2}3>$

showed significantly stronger contrast than those with a Burgers vector of $\frac{1}{3}$<11$\bar{2}$0> as shown previously in section 3.2, figure 3.12. In addition, where the inclined dislocations appeared as short line segments, it was possible to infer the direction of the inclination of the TDs from the direction of the line.

Figure 4.6.d highlights the observed direction of black-white contrast observed for the pure edge TDs (blue arrows). All the vertical pure edge dislocations exhibit a black-white contrast direction which is parallel to the Burgers vector; that is parallel to the <11$\bar{2}$0> directions also indicated in figure 4.6.d. This black-white contrast direction is consistent with their identification as edge dislocations.[101, 102, 142] The inclination direction of the inclined TD (inside the white box) is along <11$\bar{2}$0> as is logical as it is perpendicular to the mask stripes.[48, 143, 144] Figure 4.6.e shows the TD distribution derived from a larger area AFM image, the coloured area indicates the dislocations identified in figure 4.6.a to d. Figure 4.6.e reveals no trend in the distribution of TDs.

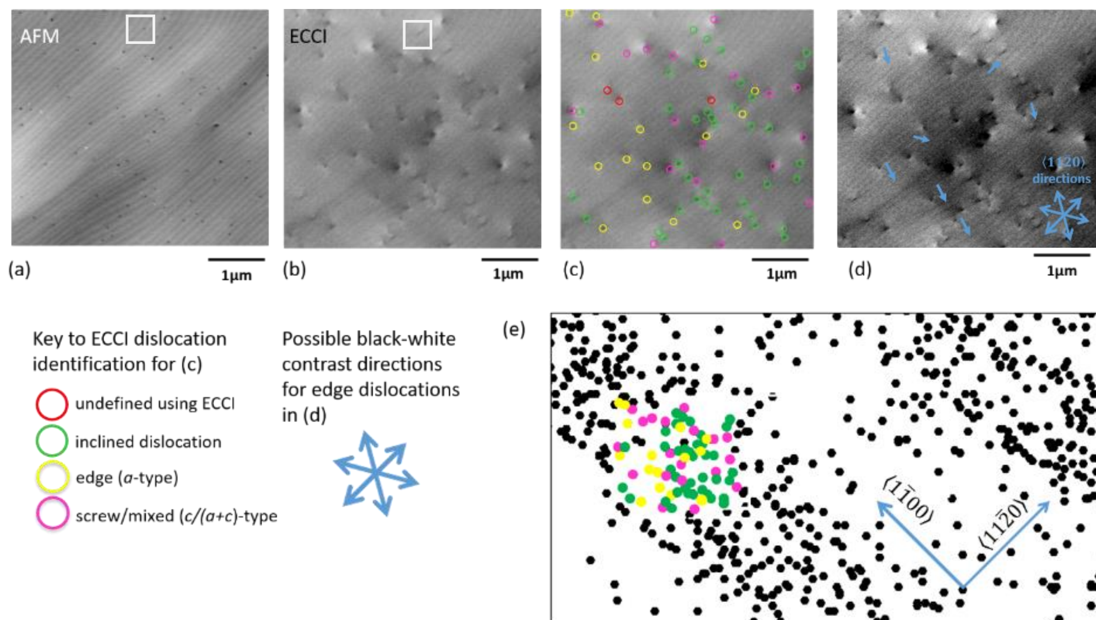

Figure 4. 6: The correlated ECCI and AFM images from a seed region a) AFM image b) ECCI micrograph c) ECCI micrograph with coloured circles representing the TDs type d) ECCI micrograph showing the possible black-white contrast direction of pure edge TDs e) distribution of dislocations determined from AFM overlaid with

identification of TDs in seed region. The wing and window stripes of the ELOG sample are readily seen.

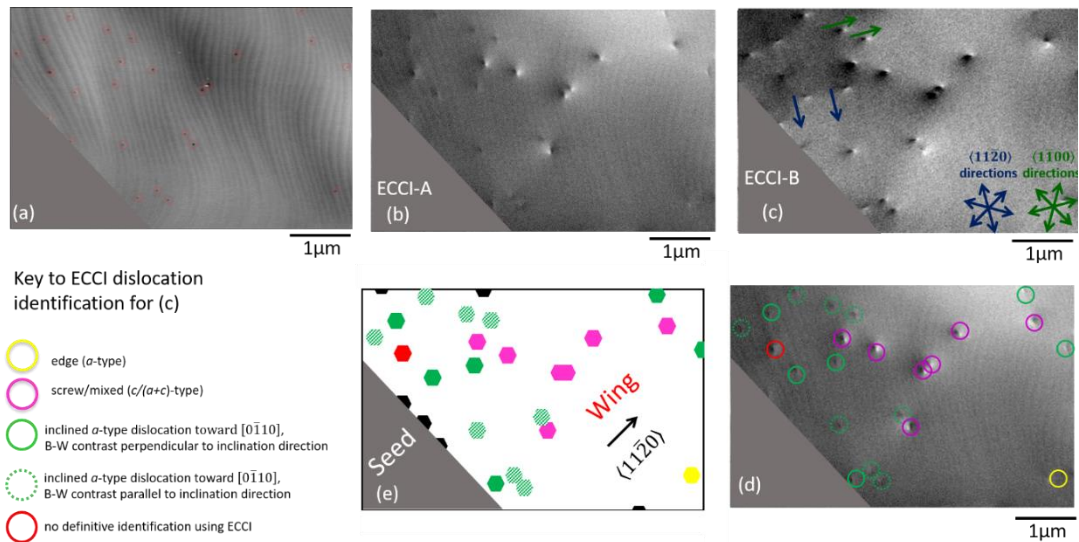

Figure 4. 7: Correlated ECCI and AFM from a wing region a) AFM image b) ECCI micrograph at first diffraction condition c) ECCI under second diffraction condition, the <11$\bar{2}$0>and <1$\bar{1}$00> directions are shown, d) ECCI micrograph with colored circles representing the TDs types as described by the key e) Distribution of dislocations determined from a larger AFM image overlaid with the identification of dislocations in wing region.

Figure 4.7 a, b, and c shows correlated AFM and ECCI images from a wing region, where b and c are ECCI micrographs obtained under different diffraction conditions. It is clear from images in figure 4.7. a and b, that the TDs are revealed in both the AFM and ECCI micrographs.

The ECCI micrograph of figure 4.7. b was acquired in a diffraction condition where the screw component TDs show stronger contrast compared to *a*-type TDs where the edge component dominates. The identification of screw component dislocations using this method agrees with the identification of these dislocations by AFM, see previous chapter for TDs identification by AFM (section 3.4). A second ECCI micrograph, figure 4.7.c was acquired to investigate the inclination of dislocations in this area. The elongation of the observed TDs, and thus the deduced inclination direction, of the *a*-

type TDs in this region appear to be toward the $[0\bar{1}10]$ direction, with an angle of 60° to the stripes (represented by green arrows). Romanov and Speck [145] observed in an AlGaN sample that the inclination of *a*-type dislocations was toward the $[1\bar{1}00]$, perpendicular to the Burgers vector of the dislocation and showed a segment of the dislocation in [0001] direction can effectively lead to a change in the strain $\Delta\varepsilon = bL\rho/2$, where b is the Burgers vector, L the segment length, and ρ is the density of dislocations. This had also been observed previously by Cantu et al.[146] in Si doped AlGaN samples, as the surface roughness increased, the strain relaxation via inclined dislocations was observed to increase. The inclination of the dislocations in this region could perhaps be attributed to the strain modulation.

In addition to the inclination direction, different directions of black-white contrast are observed for these inclined dislocations, either parallel or perpendicular to the inclination direction. For example see the two dislocations highlighted with the blue arrows, these exhibit a black-white contrast direction toward the $[\bar{2}110]$ direction, perpendicular to the inclination direction. If this black-white contrast direction is related to the Burgers vector, that is parallel to the Burgers vector, this is consistent with the results reported by Romanov and Speck [145] and Cantu et al.[146] where the inclination direction was observed to be perpendicular to the Burgers vector. However, this black-white contrast is also consistent with the contrast expected for inclined dislocations. These dislocations are marked in figure 4.7.d with solid green circles.

Other dislocations highlighted with green arrows exhibit black-white contrast toward $[0\bar{1}10]$, and the black-white contrast and the inclination directions are in the same $[0\bar{1}10]$ direction, at present we have no explanation for the contrast exhibited by these dislocations. These dislocations are marked in figure 4.7.d with dashed green circles.

The relationship between the inclination angle and the TD contrast may be explained in terms of the strain field and the angle of inclination. The higher the inclination of an *a*-type TD, the greater the [0001] segment of the TD. Follstaed et al. [147] studied three AlGaN samples with different Ga composition. High Ga composition introduced large strain to the material. To relax this strain, dislocations are inclined and show a large inclination angle for the sample with higher strain. Further information about the

role of the inclined dislocations in strain relaxation in III-nitrides materials can be found in references [148-150].

At this point, no definitive conclusions can be reached due to the low number of dislocations observed in the wing region (figure 4.7), more work is required. Multiple ECCI micrographs acquired under different diffraction conditions from different wing regions are required. Unfortunately this sample contaminated very quickly, making the acquisition of multiple ECCI micrographs difficult.

Table 4.1 summarises the results from both techniques. Inclined TDs are observed in both the seed and wing regions. 4 out of the 130 TDs observed with both AFM and ECCI were unidentified by ECCI because they were too close together to be resolved as individual TDs.

AFM TD type	**ECCI TD type**	**Total**
a-type	*a*-type	26
(a+c)/c-type	*(a+c)/c*-type	25
a-type	Inc.	72
(a+c)/c-type	Inc.	3
		126 total + 4 undefined by ECCI micrographs dislocations

Table 4. 1: Show the comparison between AFM and ECCI from seed and wing regions.

The coalescence region:

To investigate the coalescence region in more detail and to study the behaviour of the TDs, a short series of ECCI micrographs were obtained from the coalescence area (middle of the wing) under different diffraction conditions. There is a change in the rotation of approximately 30° between each condition. Figures 4.8.a-c show specific areas of the coalescence region to highlight the behaviour of particular TDs under different diffraction conditions. Figure 4.8.d shows the whole area imaged, with the specific areas shown in figures 4.8.a-c marked. For figure 4.8.a and figure 4.8.d, the ***g*** vector was estimated from the geometry of the sample to be approximately $(11\bar{2}0)$ with the majority of the TDs exhibiting strong black-white contrast parallel to the $[11\bar{2}0]$.

Figure 4.8.b shows ECCI micrographs acquired on rotating the sample by about 30° to a **g** vector of approximately $(10\bar{1}0)$. Figure 4.8.c shows ECCI micrographs acquired on rotating the sample by a further 30° to a **g** vector of approximately $(2\bar{1}\bar{1}0)$.

The majority of the TDs in the green box exhibit strongest contrast for a diffraction condition of $(11\bar{2}0)$. Three of the TDs exhibit strongest contrast for a diffraction of $(2\bar{1}\bar{1}0)$ and are identified as mixed dislocations (see TDs highlighted by pink box and circles in figure 4.8.d) with a probable Burgers vectors of $\frac{1}{3}[2\bar{1}\bar{1}3]$, $\frac{1}{3}[2\bar{1}\bar{1}\bar{3}]$, $\frac{1}{3}[\bar{2}113]$ or $\frac{1}{3}[\bar{2}11\bar{3}]$ from **g.b** considerations (see Table 4.2). The remaining TDs are probably *a*-type dislocations with a Burgers vector of $\frac{1}{3}[11\bar{2}0]$ or $\frac{1}{3}[\bar{1}\bar{1}20]$ from **g.b** considerations. The diffuse elongated contrast observed in figure 4.8.b may indicate that some of these dislocations are inclined *a*-type dislocations, however the observed contrast is too diffuse to allow for any definitive conclusions.

Finally the red box highlights what appear to be dislocation loops.[151]

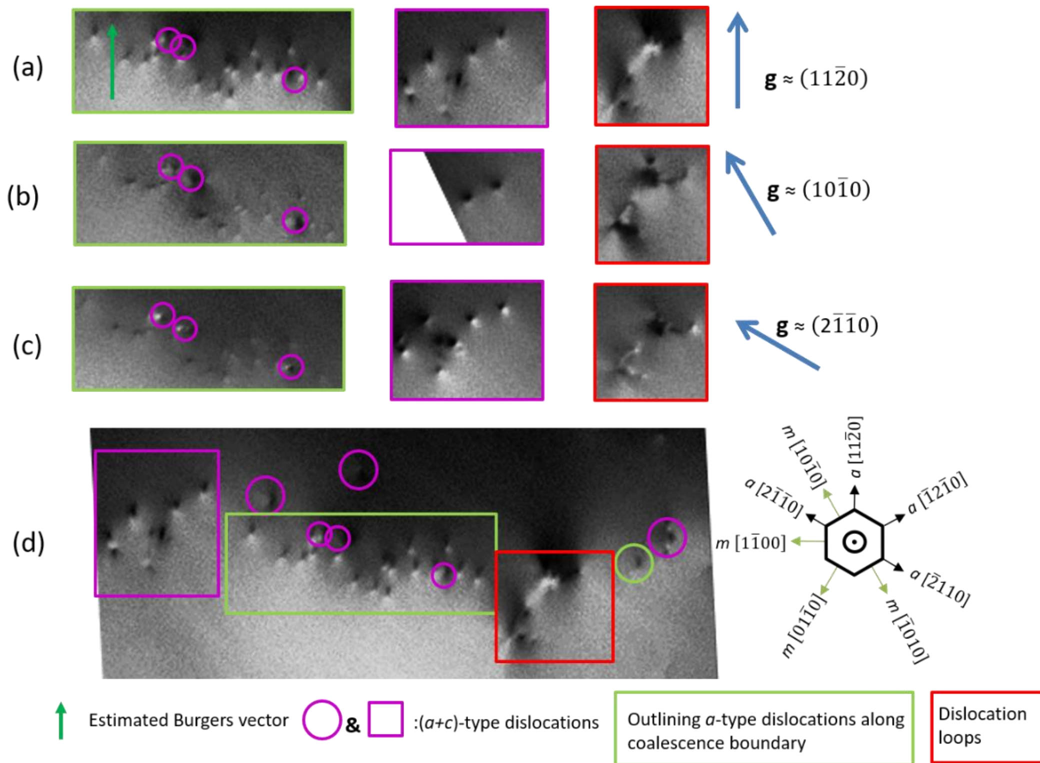

Figure 4. 8: The behaviour of inclined *a*-type and (*a*+*c*)-type dislocations under different diffraction conditions with **g** vectors of approximately a) (11$\bar{2}$0), b) (10$\bar{1}$0) and c) (2$\bar{1}\bar{1}$0) d) ECCI micrograph from whole coalescence region showing all dislocations highlighted in a, b and c. In addition, some important hexagonal direction are given.

g vector	Green rectangle *a*-type dislocations with Burgers vector = $\frac{1}{3}[11\bar{2}0]/[110]$, $\frac{1}{3}[\bar{1}\bar{1}20]/[1\bar{1}0]$ g.b		Pink box and circles Mixed dislocations with Burgers vector = $\frac{1}{3}[2\bar{1}\bar{1}3]/[101]$, $\frac{1}{3}[2\bar{1}\bar{1}\bar{3}]/[10\bar{1}]$ $\frac{1}{3}[\bar{2}113]/[\bar{1}01]$, $\frac{1}{3}[\bar{2}11\bar{3}]/[\bar{1}0\bar{1}]$ g.b	
	Calculated	**Experimental Observation**	**Calculated**	**Experimental Observation**
$(11\bar{2}0)/(110)$	2	strong contrast	1	strong contrast
$(10\bar{1}0)/(100)$	1	visible contrast	1	strong contrast
$(2\bar{1}\bar{1}0)/(2\bar{1}0)$	1	visible contrast	2	strongest contrast

Table 4. 2: Summary of the calculated visibility criterion in different diffraction conditions and the experimental observation through ECCI micrographs in figure 4.8 for *a*-type and mixed ((*a*+*c*)-type) dislocations.

Tentative estimation of inclination angle:

The inclined TDs which fail to annihilate each other cannot end inside the material [104] and reach the sample surface. TDs which incline at different angles are observed in ECCI micrographs as lines with different length (see figure 4.6). Cross-section TEM is the desirable and reliable technique to identify the inclination angles. However, ECC micrographs can be used to estimate the approximate inclination.

The relationship between the length of lines and the inclination angles is given in the following expression:

$$L = h \tan\alpha / \cos(\theta) \quad [146, 147, 152]$$

Where L is the length of the elongated line, h is the electron penetration depth within the sample (thickness of the sample in TEM measurement), α is the inclination angle, and θ is the sample tilt.

The electron penetration depth is a difficult parameter to determine but it can be estimated from measurements. In ECCI the electron probe depth is estimated to be no more than 100 nm [107]. Mansour et al.[153] estimated this value to be around 71 nm. Deitz et al.[93] demonstrated that the electron probe depth is approximately equal to

or less than the resolution of ECCI. Hence, I will assume the probe depth to be between 50 nm to 100 nm. The estimated length of the dislocation lines is between 100 nm-190 nm, the accelerating voltage is 30 kV. The inclination angles approximately are between 63°- 45° which is consistent with the previous study by Gradečak et al.[154] In their study of ELOG GaN, the inclination of *a*- type dislocation was classified into two angles 41°± 7°and 62°± 3°, in addition to the inclination mainly observed, which was at right angles to the mask alignment direction.

4.6 Summary

Electron channelling contrast imaging (ECCI) in a scanning electron microscope was correlated with atomic force microscopy (AFM) to reveal and identify threading dislocations in a 17 μm thick epitaxially laterally overgrown GaN film, where the pattern for overgrowth comprised stripes parallel to the GaN $[1\bar{1}00]$ direction. There was one to one correlation of the dislocations revealed independently by AFM and ECCI. ECCI revealed that some dislocations thread vertically through the sample, i.e., their direction is normal to the surface of the sample, while some are inclined, i.e., thread at an angle from the surface normal. Each dislocation was identified, using complementary information provided by AFM and ECCI, as either an *a*-type or as a *c*/(*a*+*c*)-type dislocation. There was complete agreement between both techniques when they were independently used to identify the vertical threading dislocations. It was harder to identify the inclined dislocations, with it being necessary to compare the results obtained using both the AFM and ECCI techniques to unambiguously identify these dislocations; the majority of inclined dislocations were identified as (*a*-type) dislocations. In the seed region the inclination direction is towards the $[11\bar{2}0]$ direction; that is perpendicular to the stripe direction. This is attributed to bending of dislocations as a result of the overgrowth process. In the wing regions the inclination direction is towards the $[0\bar{1}10]$ direction; that is at 60° degrees to the stripe. In this case the inclination angle is thought to be driven by strain relaxation.

Chapter 5

ECCI in the gaseous environment for characterization of insulating samples

This chapter demonstrates the use of the ECCI technique in the low vacuum mode in the scanning electron microscope. It describes the mechanisms which enable ECCI micrographs to be acquired in such an environment, utilizing gaseous secondary electron detectors. A gaseous environment facilitates the imaging of insulating materials which generally charge under the beam. The presence of gas in the chamber enables amplification of the signal, allowing ECCI micrographs acquired in the backscattered geometry to be obtained with improved signal to noise. This facilitates the imaging of large samples. The chapter also discusses the impact of various factors, such as detector bias, gas pressure, scan rate, working distance and sample geometry on the quality of the ECC micrographs and discusses how these were optimized.

5.1 Introduction:

The numerous applications of III-nitride based UV-LEDs such as water purification, curing, medical diagnosis, sterilization (for food, tools and surfaces) and gas sensing, has resulted in a lot of effort being dedicated to identifying techniques to examine the properties of these materials and contribute to reducing the structural defects of these materials. AlN is one of the most important III-nitride materials that is used to produce optoelectronic devices in the deep UV. The reduction of defects in these material defects contributes to an increase in the internal quantum efficiency (IQE) of AlGaN based LEDs. [3, 155, 156]

A good method with which to study extended defects in semiconductors [87, 139] or metals [88, 97] is the ECCI technique. As discussed in Chapter 3, it is an approach that is performed in a scanning electron microscope (SEM). Obtaining an ECCI micrograph from AlN is challenging since AlN is an insulating sample, and such materials charge under electron beam excitation.

The build-up of negative charges on the surface of the sample leads to repulsion of the incident electron beam and this causes numerous problems such as drift, low contrast, and creates a blurry image. There are several ways to solve the charging problem, such as coating the samples with conductive materials. Carbon is the most preferred for coating due to its low atomic number. The coating process should be controlled carefully to ensure that the strength of the measured signal is not reduced.

Alternatively, the low vacuum SEM mode helps to eliminate the charging and enhance the signals. The wide application of the variable pressure-SEM (VP-SEM) for studying biological samples, uncoated insulators, and semiconductor samples [157-164], motivated me to characterize the AlN samples by using this reliable and non-destructive technique. Performing ECCI in a low vacuum mode is a new approach that lets us investigate the properties and defects in AlN samples. In this present work, I worked on and optimized the use of the gaseous secondary electron detector to obtain ECCI micrographs from insulating samples with no need for any coating process.

All the ECCI micrographs in this chapter were acquired using the FEI Quanta 250 variable pressure FEG-SEM (Thermo Fisher). Typically, an electron beam energy of 30 keV, beam currents between $\approx$2 nA to 4 nA, working distances between 10 mm and 16 mm and gas pressures between 0.5 mbar and 1 mbar were used to perform ECCI in a low vacuum mode. All images were processed after acquisition by applying fast Fourier transform band-pass filtering in ImageJ to eliminate the horizontal lines that are as a result of gas fluctuation during the scanning.

5.2 The principle of the variable pressure SEM (VP-SEM)

The essential aim of studying charging samples in as natural state as is possible led to researchers in the 1970s to innovate and produce an alternative SEM that was capable of operating at high pressure.[81] This approach can be applied in the case of charging (insulating or semiconductor materials), wet, dry, liquid and biological samples in the low vacuum mode (high pressure). The low vacuum SEM or variable pressure- SEM (VP-SEM) sample chamber pressure ranges between 0.1- 10 torr (≈ 0.1–13 mbar), while the column remains under high vacuum ($\leq 10^{-6}$ mbar). As illustrated in Figure 5.1, the main difference between VP-SEM and the conventional SEM (described in chapter 3) is the pumping system and a series of pressure limiting apertures (PLAs). There are three pressure zones in the VP-SEM that ensure a differential pressure can be applied in the SEM. Figure 5.1 shows three pressure zones P0, P1, and P2. Any leak in the gas from the sample chamber can be pumped out in the P1 zone (between the two apertures), this is to keep the column and gun filament under high vacuum. The sample chamber is under high-pressure P0 which separated from the column which is always kept under low-pressure P2. In the FEI Quanta ESEM, PLA1 is located just below the pole pieces with the gaseous secondary electron detector (GSED) placed directly above the sample. The region between PLA1 and PLA2 are kept under intermediate pressure P1 ($\approx 10^{-1}$ mbar) and are connected directly to the pumping system.[165]

Numbers of gases have been utilized to date in the environmental SEM including air, water (H_2O), N_2, CO_2, N_2O, He, NH_3 and CH_3CH_2OH. Water vapor (H_2O) is the most common gas used and was used in this present work. The inserted gas has two main functions: it eliminates the accumulated negative charges from the sample surface and acts as the media for amplification of secondary electrons (SEs) (explained later in this section).

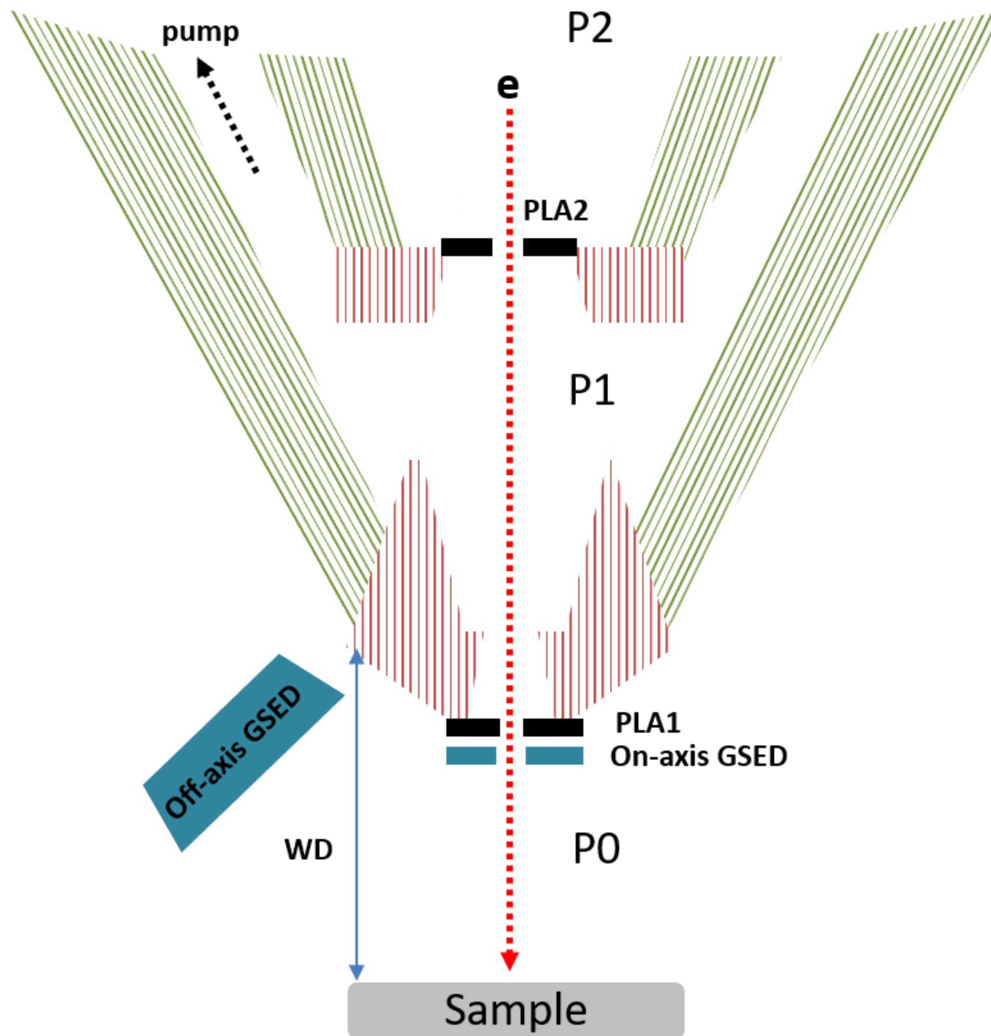

Figure 5. 1: The variable SEM parts, including three different regions in pressure P0, P1, and P2 besides series of PLAs (PLA1 and PLA2).

Gas-primary beam interaction

In addition to the sample-primary beam interaction (explained in chapter 3), an extra interaction will occur between the primary beam and the gas molecules as a result of inserting any gas into the sample chamber of the VP-SEM. The primary beam, as a result of the new interaction can be classified into two types: unscattered beam (conserves its energy and its trajectory) and the scattered beam which has lost energy and results in the beam probe becoming wider. The primary electrons (PEs) interaction with inserted gas will produce the environmental secondary electrons ESEs which are the basis of the gaseous secondary detection following the equation:

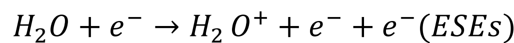

$$H_2O + e^- \rightarrow H_2\,O^+ + e^- + e^-(ESEs)$$

The scattered beam leads to the formation of the beam skirt which affects the signal to noise ratio and the image resolution as a result of generating SEs far away from the focused beam which acts as a noise background to the image.

The beam scattering phenomena depends on various factors: the type of gas, gas pressure, beam energy, and the working distance WD.

The radius of the skirt may be estimated using the equation derived by Danilatos [166]:

$$R = (0.364\ Z/E)\ (p/T)^{1/2}\ L^{3/2}$$

Where, R = skirt radius (m)

Z = atomic number of the gas

E = beam energy (keV)

p = pressure (Pa)

T = temperature (K)

L = the beam-gas path length (m)

The total scattering cross-section of the gas is the main factor that is used to determine the energy loss in the incident primary beam as also illustrated by Danilatos. This factor depends on the energy of incident electrons and the type of gas. According to Thiel, [167] the scattering cross-section of low energy electrons (SEs) is one to three orders of magnitude greater than that of high energy electrons (e. g. PE, BSE). m is the number of the collisions per electron $m = \sigma_T n d$ where n is the gas-particle

concentration, d is the free mean path, σ_T is the total cross section. Then the probability that an electron suffers x number of collisions (x= 0,1,2,..) can be written as a Poissonian probability formula :

$$p(x) = \frac{m^x e^{-m}}{x!} \qquad 5.1$$

The number of electron-gas molecule collisions reduces as the distance the electron travels through the gas reduces, this also reduces as the gas pressure is reduced. [166]

The gaseous secondary electron detectors (GSEDs)

In this present work two types of GSEDs were used and they will be discussed here; an on-axis GSED, metallic ring 3 mm in diameter, and an off-axis GSED, comprising a metallic plate. The on-axis detector is located directly below the pole piece and it provides a small field of view. The off-axis detector is located off the pole piece axis. See figure 5.2 which shows the detection mechanism of SEs in the gaseous environment, where the off-axis detector is used.

An applied positive bias on the gaseous secondary electron detectors (GSEDs) accelerates the emitted SEs from the sample, with energies which are typically a few eV. The accelerated SEs are directed toward the GSED, which is located nearly above the sample. When the kinetic energy of electrons are above the first ionization potential energy of the gas (12.7 eV for H_2O), then they will ionize the gas. As a result of this interaction, a positive ion and an extra free electron will be produced. The additional free electrons are called the environmental secondary electrons (ESEs). The gas amplification process is a continuous process as both electrons are accelerated and cause further ionizations events, to simplicity, the diagram in figure 5.2 shows the amplification process for one electron (green spheres). In the case of using H_2O as imaging gas, the generated ESE signal is up to three orders of magnitude (10^3) greater than the original emitting SEs from the sample surface.[164] [168]

In addition, the resultant heavy positive ions (blue sphere in figure 5.2) will drift toward the negatively biased sample. The recombination between the positive and the

negative charge on the sample surface, results in negative charges which accumulate on the sample surface to be eliminated (charge neutralization).

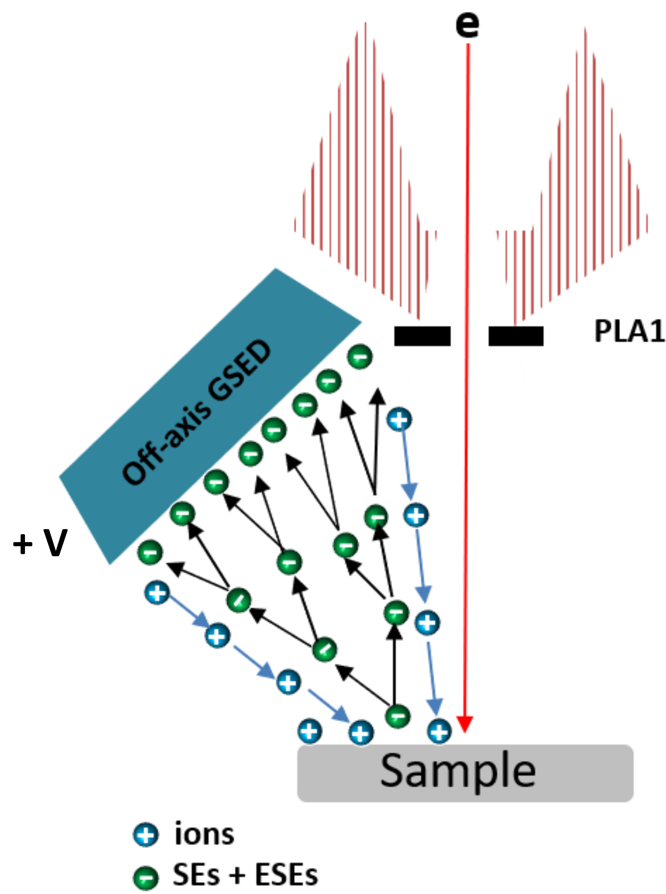

Figure 5. 2: The gaseous secondary detection mechanism, in the case of using the off-axis detector. Generated SEs from sample ionize the imaging gas molecules. Positive ions move to land on the sample surface and the amplification process of SEs continue and attracted by the positive bias detector.

1. On-axis GSED

This detector is located directly above the sample so one can think about this as a capacitor which contains two parallel plates separated by distance l. While the upper plate (electrode) held at +V bias and the lower plate (sample) is earthed (V=0), the electric field between the detector and sample is constant $E=V/l$. This detector required higher pressure in the range of 1-20 Torr (≈1-26 mbar). The beam-gas path length is equal to the sample- detector distance see figure 5.3.a. As the working distance is decreased, the amplification process decreases as well (or in other words, the distance between the sample and the detector is decreased as well).

2. Off-axis GSED

The off-axis detector has the potential to show a large field of view, it is also known as the large field detector (LFD). This detector follows the same principle of gas amplification. The location of this detector is off-axis in the SEM as shown in figure 5.1 . The off-axis detector can provide a very excellent signal at low pressure with maximum pressure of 1.5 mbar. This detector allows scanning at short working distance to minimize the beam-gas path length (to reduce the beam scattering).While at the same time the distance between the sample and detector can be kept larger than the beam-gas path length see figure 5.3.b. Thus the amplification process here is much larger than in the case of on-axis detector, or in other words the ion flux reaching the sample is much larger.[167]

This detector can be used in low pressure at a short working distance and still give a very acceptable signal. It is very good for imaging insulator samples that require more ions to overcome the charging issue (large amplification process), however it is not ideal for imaging were high pressure is required (hydrated sample), in such a case the on-axis detector is the more appropriate detector to use.

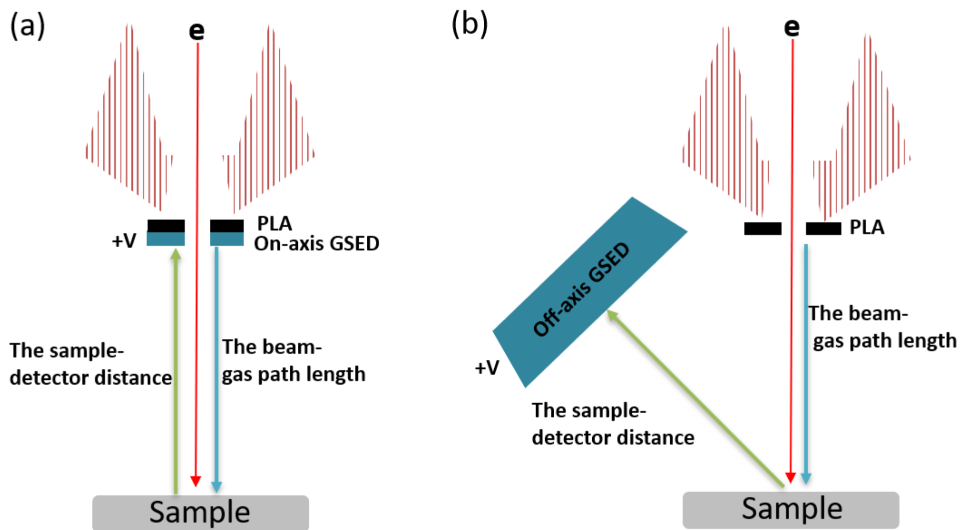

Figure 5. 3: Shows that a) the on-axis GSED where the beam-gas path length (blue arrow) is equivalent to the sample-detectoe distance (green arrow), b) the off-axis GSED where the beam-gas path length (blue arrow) is not is not equivalent to the sample-detectoe distance (green arrow).

5.3 ECCI technique as a new approach in VP-SEM

The interaction between the electron beam and the sample leads to the emission of several signals from the sample which provide different information about the sample's properties, such as structural, chemical composition, and topographical information. The electron signals, that is secondary electrons (SEs) and backscattered electrons (BSEs) are the main focus in this chapter. SEs can, as previously discussed in chapter 3, provide us with the surface topography, and the BSEs supply both surface topography and for appropriate samples compositional information. With the sample placed at or close to the Bragg's condition, this can provide us with diffraction information and thus provide structural information on the sample. [87, 92, 139]
Emitted SEs have energy of ≈ 5 eV which is insufficient to ionize the gas (in the case of water vapour the first ionization potential ≈12.5 eV), so an electric potential applied to the GSED electrode will increase their kinetic energy to a value which is sufficient to ionize the gas molecules by ejection of bound electrons and forming positive ions that participate in neutralizing the charging sample. Its worth mentioning that the primary beam and BSEs contribute in the gas ionization process however, the SEs have the highest interaction cross section. As a result, the signal provided by GSEDs is dominated by SEs signal. [83, 159, 167, 169]. The original emitted SEs and the ejected electrons of the gas molecules either by SE, BSE or even by the primary beam will be all accelerated by the applied bias, leading to continuous gas ionization events forming the cascade of SE signal, increasing the signal by up to three orders of magnitude.[170-172]
The image generated from the gaseous secondary electrons detector GSEDs when the sample is placed at or close to the Bragg angle, is a synthesis of topographic and diffraction information. The diffraction contrast that is provided here by detecting the secondary electrons SEs, is attributed to the fact that the diffraction of the primary beam PE modulates all generated signal intensities of the samples e.g. BSEs, SEs, and the light emission signal. [21] Figure 5.4.a shows the ECC micrograph that is produced by GSED, specifically by the large field detector (the off-axis detector), from an AlN thin film.

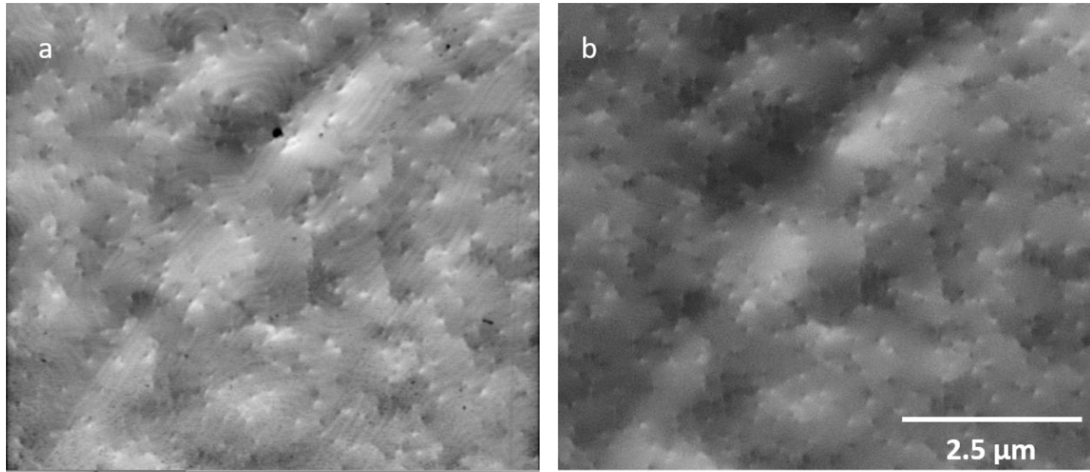

Figure 5. 4: ECCI micrographs acquired at tilt 64.6° of AlN thin film from a) the large field detector LFD b) the forescattered solid-state detector that located under the EBSD detector. The accelerating voltage is 30 keV for both images, and the gas pressure is 0.6 mbar.

The image clearly reveals threading dislocations (TDs) as the sample is oriented at a diffraction condition, and surface atomic steps. Figure 5.4.b shows the ECCI micrograph provided by the conventional solid-state detector from the same area at the same time. There is one to one correlation in TDs between the LFD and the conventional solid-state detector. The images were produced under the accelerating voltage of the electron beam of 30 keV, gas pressure of 0.5 mbar, both images acquired at the high tilt of 64.6° and a working distance of 11 mm. The bias on the LFD was +230V. Section 5.4 discusses the impacts of these parameters on the quality of the acquired images.

Even though there is no significant difference in dislocation contrast and the dislocation density derived from both images acquired by both detectors, however the detectors function is different. The solid-state detectors collect the high energy BSEs while the GSED, as mentioned before, collects the low energy electrons. It is an obvious difference that the image obtained by the forescattered detector does not show any atomic steps however, atomic steps are clear in the image obtained by LFD. The

contrast in the images acquired with GSEDs does not appear to be dependent on the relative positions of the sample and detector.

At low magnification, an ECP for the single crystal AlN thin film was captured by the LFD (ECP was described in Chapter 3). Obtaining the ***g*** vector from the ECP pattern will help to identify the type of TDs. Figure 5.5., shows that the pattern center is located on the Kikuchi band from a (11-20) plane, so the estimated ***g*** vector is (11-20).

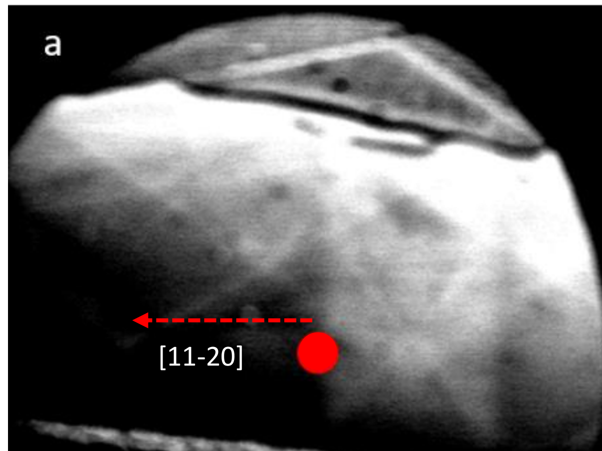

Figure 5. 5: Shows ECP that acquired using off-axis GSED, and the red circle is the pattern center. The ***g*** vector is (11-20)

Images exhibiting diffraction contrast can also be acquired with the on-axis detector. Also, related to this detector, its position is not playing any significant role in the contrast observed in the ECCI micrograph or ECPs. Since positive bias is applied to the GSEDs, the sample and detector act as a capacitor, and the electron direction is toward the detector out from the sample (which is as the negative plate of the capacitor). Figure 5.6 demonstrates the capability of the detectors to produce ECCI micrographs in both backscattered and forescattered geometries with a spatial resolution of approximately 30 nm at a gas pressure of 1 mbar. The on-axis detector can reduce the effect of the beam skirt at high gas pressure thus allowing ECCI micrographs of high signal to noise ratio to be obtained.

Hence, this new approach can be an alternative to a backscattered detector that is placed under the pole piece of SEM and the forescattered detector that may be located

under the EBSD system. The GSEDs offer the flexibility to tilt the sample between 0° to 70° to achieve a wide range of diffraction conditions.

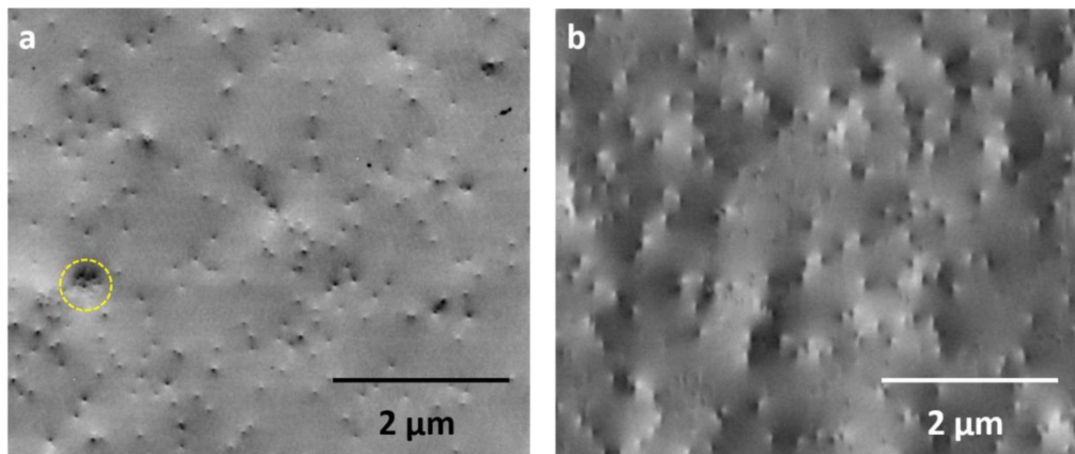

Figure 5. 6: Shows the ECCI micrographs of AlN thin film not from the same area obtained used the on-axis detector (the ring) located under the pole piece; the image acquired a) at tilt 0°, the dotted circle shows a cluster of TDs with the separation distance ≈ 30 nm. b) at tilt 65°. The accelerating voltage of 30 keV, gas pressure of 1 mbar.

5.4 The effective parameters on ECC imaging in VP-SEM

5.4.1 Effect of detector bias

Typically, around +250 V positive bias is applied to the off-axis gaseous secondary electron detector (GSED) to attract electrons emitted from the sample. As a result, a series of gas ionization and the generation of the environmental SEs, an amplified current will be produced. Figures 5.7 a, b, c, and d are a series of images with different bias/contrast setting 100%, 75%, 50%, and 25%, respectively. The images illustrate the significant influence of the detector bias on the image in terms of signal to noise ratio. The highest bias is desirable, as shown in figure 5.7.a in that more electrons will be accelerated and attracted by GSED to contribute in imaging. For figure 5.7.d, in which the bias is 25%, this leads to unclear surface features (black dots). Also, the dislocations that surrounding by the red circles in all four images in figure 5.7, become invisible in figure 5.7.d. In figure 5.7.a and b those two dislocations are clearly visible.

All acquired ECCI micrographs were obtained under the same conditions: beam current and accelerating voltage of 30 keV, dwell time of 100 µs, and the sample was tilted to 64°.

To investigate the impact of detector bias on the amplification process, the sample current was measured as a function of accelerating voltage and contrast setting (detector bias). It was measured by using the Faraday cup and an electrometer. In brief, you mount the Faraday cup (it's a piece of metal with a hole in it) that collects the electrons, and the output of this is connected to the electrometer to measure the current. The plot in figure 5.8 shows the values of the sample current for each contrast value. As the detector bias is increased, the sample current also increases. The examined values of detector bias are between 100%-50%. From the plot, the sample current at 50% of detector bias is close to the zero value for all accelerating voltage of 10 keV, 20 keV, 30 keV. While in the case of increasing the detector bias to 100% (+250 V) the sample current reach the values of 40 nA, 90 nA, 130 nA for accelerating voltage of 10 keV, 20 keV, 30 keV, respectively.

The sample current is a sum of the electrons and ion current, as Mohan et al.[161] experimentally showed that in the high vacuum SEM mode, the sample current with negative value (only electrons) is independent of the detector bias. Where introducing the gas to the chamber is changing the sign to positive (ions flux) and become dependent on the detector bias. Similar results to Mohan et al. [161] result, the sample current increased as the detector bias is increased. Note that in Mohan et al. study they used the on-axis detector where here the off-axis detector was used.

To compare the images in figure 5.7 to the result obtained from the plot in figure 5.8, the higher ion flux reach the sample mean higher amplification signal that reach the detector. Image with higher signal to noise ratio obtained at close 100% of the detector bias value.

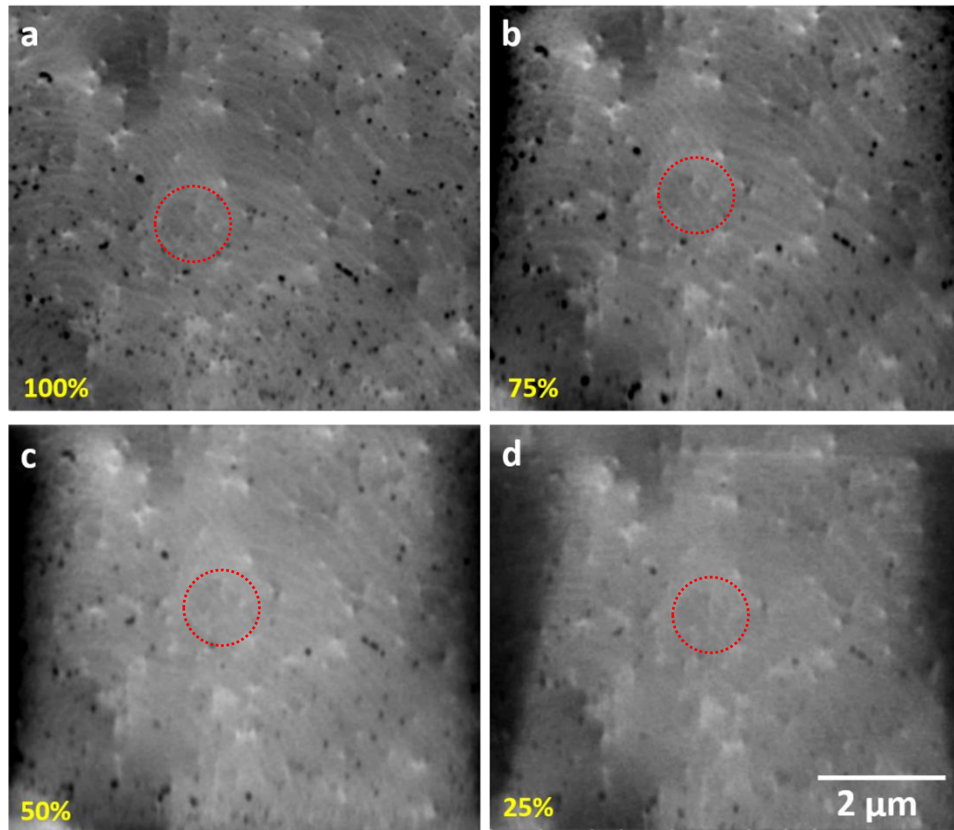

Figure 5. 7: Shows the impact of changing the detector bias by changing the contrast setting of the gaseous secondary electron detector to (a) 100 %, (b) 75%, (c) 50 %, and (d) 25 %. The signal strength decreases as the bias voltage is decreased. All four ECCI micrographs are acquired with the same beam current and an acceleration voltage of 30 keV, dwell time of 100 µs, and a sample tilt of 64°.

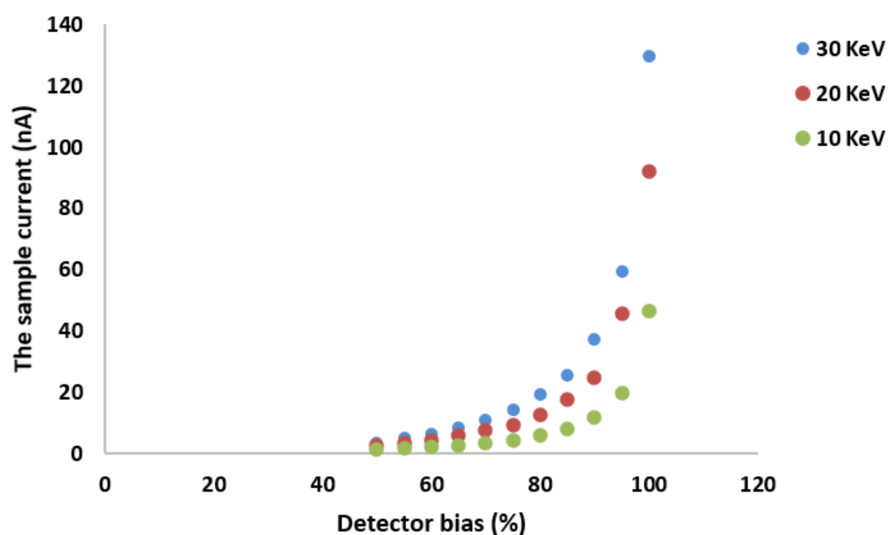

Figure 5. 8: Shows the plots of the magnitude of the sample current (nA) as a function of the various accelerating voltages (keV) and the detector bias (%) for fixed gas pressure of 0.5 mbar and spot size of 6.

5.4.2 Effect of gas pressure

The influence of gas pressure on the spatial resolution was investigated. Comparing images acquired as the pressure was increased revealed a slight degradation in the resolution with increased pressure, this is illustrated in figure 5.9. Note that in the image of figure 5.9 a, two very close dislocations clearly can be resolved as separated dislocations, whereas in c they can be no longer resolved and appear as a single dislocation. It is also obvious on comparing the three images that by increasing the gas pressure, the signal to noise ratio is slightly decreased as well. As the gas pressure increased to very large amount, the gas molecules could prevent the SE current from reaching the GSED in addition, cause the primary beam to be scattered.[167] All three ECCI micrographs were acquired with the same beam current and an acceleration voltage of 30 keV, dwell time of 100 µs, and a sample tilt of 52°.

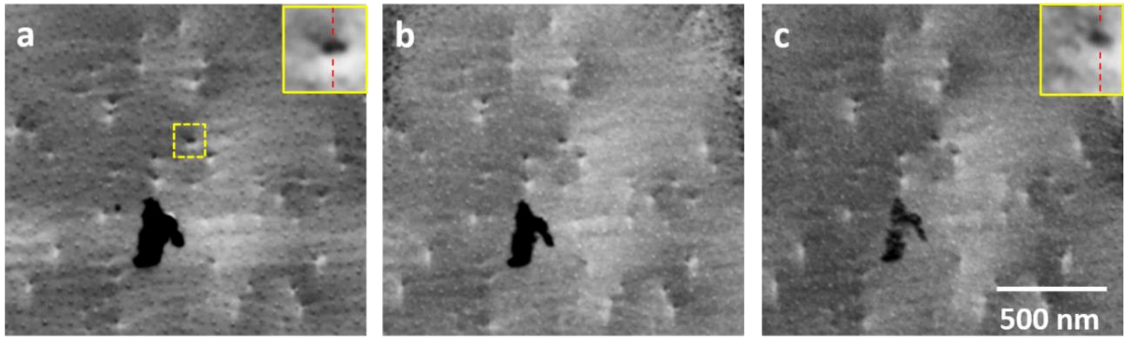

Figure 5. 9: ECCI micrographs of AlN thin film acquired at the same beam current and an acceleration voltage of 30 keV, of tilt of 52°, dwell time of 100µs, and of gas pressures (a) 0.3 mbar, (b) 0.5 mbar and (c) 0.8 mbar. The inset image in (a) shows two dislocations that can be resolved at a gas pressure of 0.3 mbar. However, on increasing the gas pressure to 0.8 mbar (inset in image c), the individual dislocations are no longer resolved.

Figure 5.10 shows the plot of the magnitude of the sample current (nA) as a function of the various accelerating voltages (keV) for different gas pressures of 0.5, 0.7, and 1 mbar respectively at spot size 6. Clearly, increasing the gas pressure increased the total ions that reach the sample. If the data from the plot are compared to the ECCI micrographs in figure 5.9, that mean increasing the gas pressure should be controlled carefully as this increase may have negative effect on the image even though it is lead to increasing the signal amplification process.

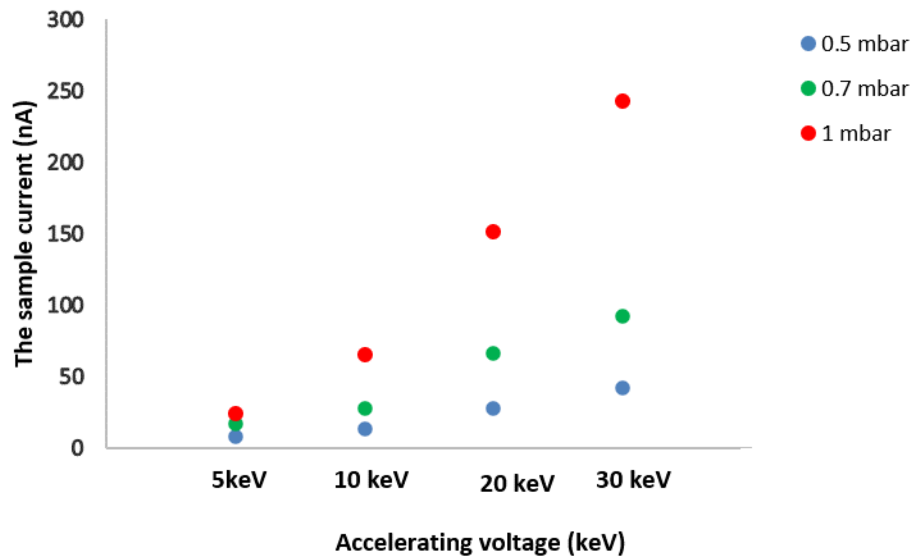

Figure 5. 10: The impact of gas pressure in VP-SEM on the beam current. It significantly increased as the gas pressure increased. at 0.5 mbar, 0.7 mbar, and at 1 mbar for different beam accelerating voltage (5, 10, 20, 30 keV) for spot size of 6.

5.4.3 Effect of scan rate

Increasing the length of time you take to acquire images in the VP-SEM will improve your signal to noise ratio by eliminating random noise, just as is the case for high vacuum -SEM mode. [173]

Here I investigated the effect of the dwell time on acquired ECCI micrographs with the off-axis detector. Figure 5.11 shows the difference between images acquired with different dwell times. It is clear that a long scan improves the signal to noise ratio, and as a result, a high quality image can be obtained. Under the long scan rate, the TDs become visible. Note that from figure 5.11.c and d, horizontal bright and dark bands are introduced to the image, their density is proportional to the scan time. This as a result of the fluctuation of gas pressure during the scan. An FFT- bandpass filter in the ImageJ imaging software is used to remove any horizontal or vertical lines that are introduced to the image during the scan. Figure 5.11 a, b, c and d are the image acquired at a dwell time of 1 μs, 10 μs, 100 μs, and 1000 μs respectively. While e, f, g, and h are the same images respectively after applying FFT bandpass filter.

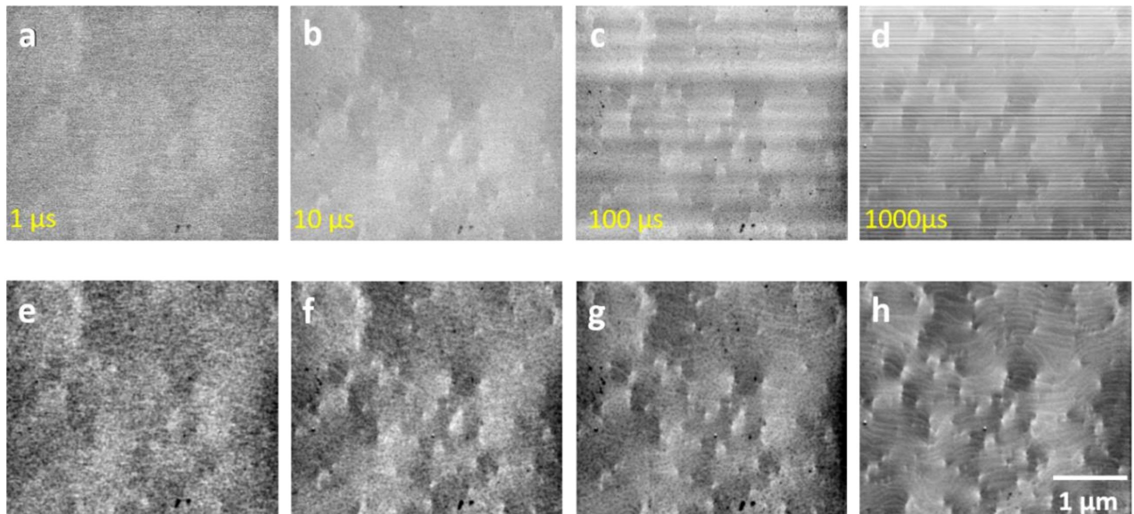

Figure 5. 11 ECCI micrographs of AlN thin film acquired at the same beam current and an acceleration voltage of 30 keV, tilt 52°, 11.4 mm working distance and at various dwell times of (a) 1 µs, (b) 10 µs, (c) 100 µs and (d) 1000 µs. The dark and bright horizontal lines observed when the scan time is long (c and d) are due to fluctuations in the gas pressure. (e-f) show the images after FFT band-pass filtering to remove the horizontal lines. All images were taken with an image resolution of 1024 × 884.

5.4.4 Effect of working distance

The beam-gas path length (≈ working distance), is a crucial parameter for the cascade amplification process of electrons in the VP-SEM. Similarly, the distance between the sample and the GSED should be taking into consideration when acquiring images. This section reports on the investigation of the impact of the working distance on the quality of the generated ECCI micrographs. A greater amplification can be acquired at the longer gas path length; however, at a low vacuum moving the sample too far away from the objective lens can negatively affected the quality of images as the sample is moved away from the focused beam. Figure 5.12 a, b, c, and d shows images acquired at working distance at 6 mm, 8 mm, 11 mm, 14 mm respectively, obviously, there is not a large negative impact on the image quality since the change in working distance was very slight. The images shown in c and d are slightly noisier when compared to

the images in a and b, this may be as a result of changing of the signal to noise ratio by increasing the working distance. This noise is due to increasing the beam-gas path length which lead to beam scattering by the gas molecules (beam skirt issue), as a consequence the skirt electrons will interact with the surrounded area of the studied area and resulting noise. [83]

In the present result, all four images in figure 5.12 contain similar surface and diffraction information. All ECC micrographs in Figure 5.12 are acquired at the same conditions beam current and an acceleration voltage of 30 keV, P= 0.5 mbar, dwell time of 100 μs, and a sample tilt of 0°.

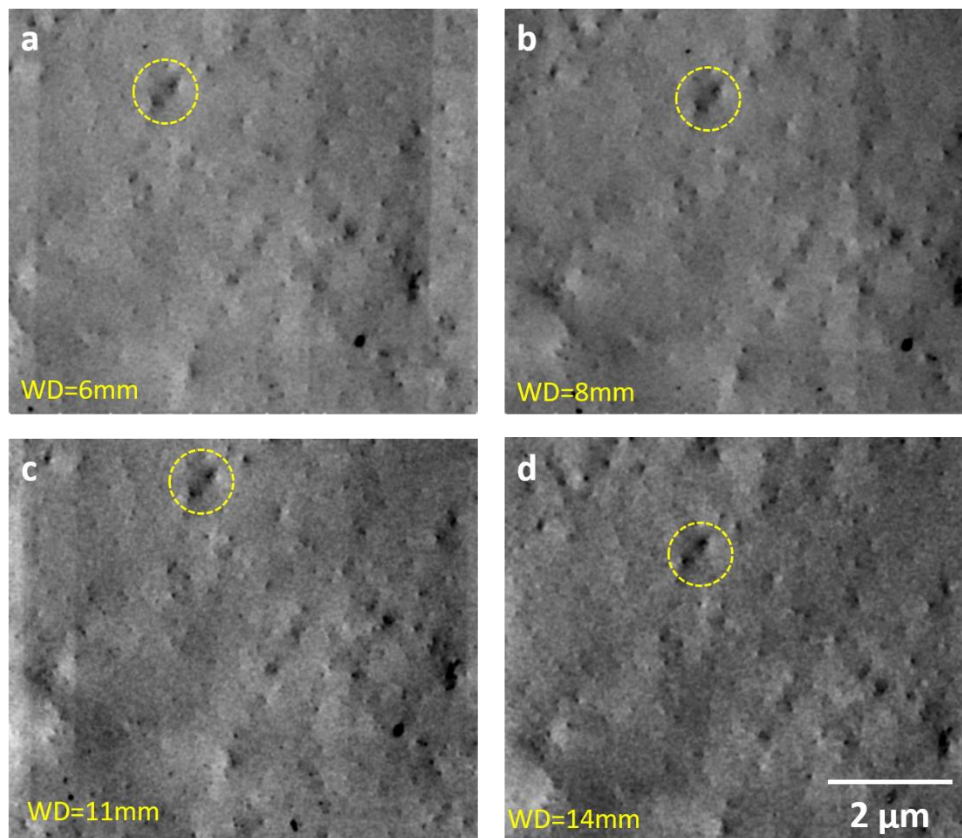

Figure 5. 12: ECCI micrographs of AlN thin film acquired at the same beam current and an acceleration voltage of 30 keV, of tilt of 0°, dwell time of 100 μs and various of working distance between the sample and the pole piece to (a) 6 mm, (b) 8 mm, (c) 11 mm and (d) 14 mm.

Figure 5.13 shows that The sample current at 30 keV at working distance of ≈ 14 mm is ≈ 70 nA higher while the sample current at working distance of 10 mm is 40 nA. Clearly this plot show that the sample current (ion flux) increases as the working distance is increased. To conclude, an increase in the gas amplification is obtained by increasing the working distance. However, it should be taken into consideration that on increasing the working distance, the gas-beam path length will also increase and cause the beam scattering that lead to affect the signal to noise ratio. All acquired data in the graphs figure 5.13 acquired under vacuum 0.5 mbar.

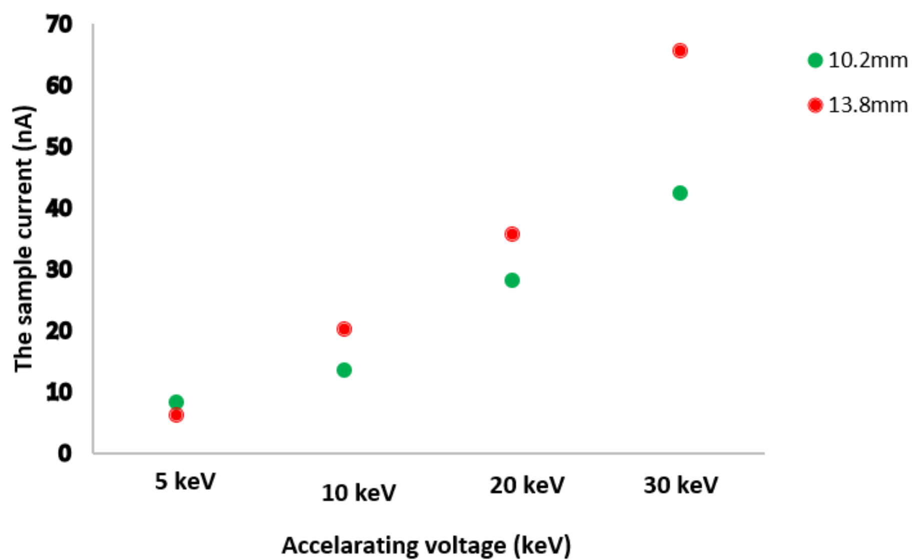

Figure 5. 13: Shows the plots of the magnitude of the sample current (nA) as a function of the various accelerating voltages (keV) and the spot size for fixed gas pressure, at working distance = 13.8 mm and 10.2mm and the information obtained under the gas pressure of 0.5 mbar and spot size of 6. The influence of increasing working distance, as well as the beam-gas path length increases, the current increased as shown from graphs.

5.4.5 Effect of sample geometry

Increasing the tilt of the sample so that it is in the forescatter geometry increases the BSE yield as well as the yield of SE. Figure 5.14 shows two images that demonstrate the effect of modifying the tilt of the sample from 0° to high angles on the ECCI micrograph in VP-SEM. The difference between the two images is that figure 5.14.a, which is acquired at 0°(backscatter geometry), shows the signal to noise is improved due to the higher SE yield and that obvious from the topography information observed in the image. While in figure 5.14.b, the 70° tilt (forescatter geometry) the image contrast (the signal to noise ratio) increased. It is proof of the statement which includes the position of the GSEDs has no significant impact on the image except that the tilting sample modifies the electrons yield, and consequently, the contrast and the spatial resolution of the image will be affected as well. From the two images, there is a one to one correlation in the dislocations seen in both images. Both ECC micrographs are acquired under similar conditions of the beam current and the accelerating voltage of 30 keV, 0.5 mbar, and dwell time of 100 µs.

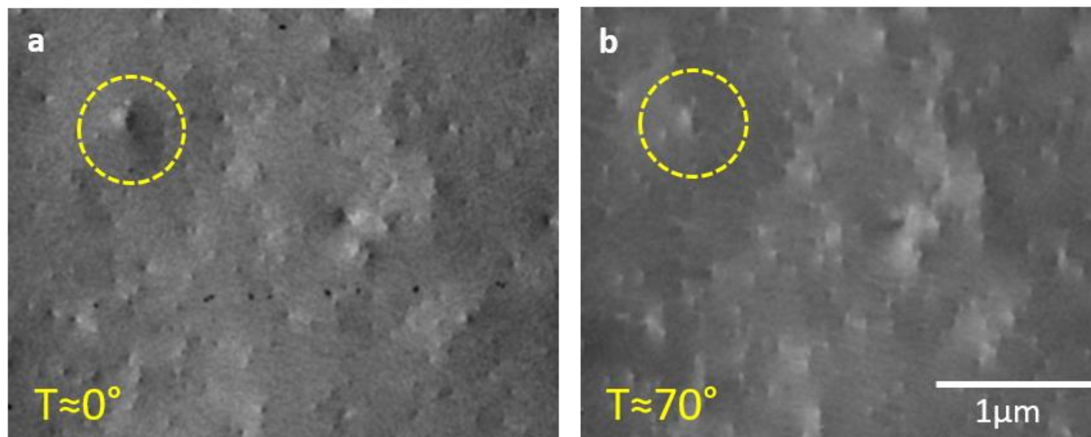

Figure 5. 14: ECCI micrographs of AlN thin film acquired at the same beam current and an acceleration voltage of 30 keV, dwell time of 100 µs and sample tilt at (a) 0° tilt, ideally used in the backscatter geometry and (b) 70° tilt, often used in the forescatter geometry.

5.5 Summary:

In conclusion, this chapter demonstrate the capability of using the variable pressure - SEM (VP-SEM) to conducting ECCI measurements on semiconductor or insulating samples). The working principle for this mode is based on that the accelerated electrons (most likely SEs) ionize the H_2O molecules to produce positive ions and extra electrons (ESEs). The positive ions participate in eliminating charging where the resultant electrons will continue the ionization process. Also the ability of gaseous secondary electron detectors GSEDs (either on-axis detector or off-axis detector /LFD) to produce high quality ECCI micrographs and ECPs has been demonstrated. The signal provided by the GSEDs is a result of detecting the SEs under diffraction of the primary beam, which affects the intensity of all outcoming signals (e.g. BSEs, SEs, etc.). The imaging in the VP-SEM is affected by various parameters like the detector bias, gas pressure, scan rate, working distance, and the sample geometry.

In this research it was found that the detector bias must be set at a large value, all images in this thesis were obtained with the detector bias above 90% (≈ 230V). The gas pressure is a crucial factor in ECC imaging, in that a high amount of gas in the chamber can degrade the image quality hence, gas pressures of ≈ 0.5 mbar were used for the images presented in this thesis as this was sufficient to overcome the charging problem and provide acceptable images. Long scan times will successfully improve the signal to noise ratio by removing the noise. However, this led to line artefacts in the images due to gas fluctuations which were removed by applying an FFT filter in ImageJ software. Larger working distance can provide higher sample current (ions), however at the same time can decrease the signal to noise ratio as a result of the primary beam scattering by the gas molecules. Images in this thesis where taken with working distance around 10-11 mm. The last parameter is the sample geometry, the sample at the horizontal (0° tilting) and at sample tilting at 70° exhibits no difference in the image information except the sample at 70° has more signal to noise. Next chapter is an application based on this chapter, all ECCI micrographs of AlN samples in chapter 6 are produced using the gaseous secondary electron detector GSED (off-axis detector) in VP-SEM.

Chapter 6

Characterization of AlN/nPSS thin films by SEM

In this chapter results from five AlN samples overgrown on nano patterned sapphire substrates (nPSSs) by MOVPE are discussed. In this case, the nPSS was patterned with nanopillars. The samples are divided into two series. In the first series, the influence of substrate miscut on the morphology and structural properties (e.g., step bunching, threading dislocation (TD) density, dislocation type and misorientation) is investigated by comparing results for two samples with a substrate miscut of 0.1° and 0.2° respectively. In the second series, the results from three samples are compared to explore the influence of the nanopillar dimensions, specifically pillar diameter, on step bunching, TD density, dislocation type and misorientation. ECCI was used to determine the TD density and the relative percentages of edge dislocations and dislocations with a screw component, and explore the relationship of dislocations and sub-grains in the AlN/nPSS thin films. EBSD was used to investigate the magnitude and sense of the relative misorientation of the sub-grains.

6.1 Introduction

The significant applications of AlGaN deep UV-LEDs in the medical field and water purification motivated research to produce high-performance of UV-LEDs through the growth of LED structures on high-quality AlN/sapphire templates. [174, 175] Such templates of high quality can be achieved via defect reduction mechanisms using nPSS, which can be performed in MBE, MOVPE/MOCVD or HVPE reactors, discussed briefly in chapter 2.

Kneissl et al [3] obtained a TD density of $\approx 5\times10^{8}cm^{-2}$ for an AlN/nPSS epilayer grown by MOVPE to a thickness of 2.5 µm. This was lower than the density of TD from a sample grown on a conventional sapphire substrate, which estimated to be $\approx 1\times10^{10}$ cm^{-2}. Such a reduction in TDs density improves the internal quantum efficiency of UV-LED structures from ≈5% to ≈40%. Considerable improvement in the structural properties of AlGaN grown on AlN/nPSS in comparison to the one grown on the conventional sapphire substrate, a high-quality AlGaN epilayer with a smooth surface and significant reduction in TDs can be achieved. [176] Tasi et al.[177] found that the screw and edge dislocations density had decreased for an AlGaN sample grown on nPSS, utilizing a nano hexagonal hole pattern, compared to the one grown on the conventional substrate. They revealed that, for example, the screw dislocations density reduced from 7×10^{9} cm^{-2} (for the sample grown on conventional sapphire) to 1-2 $\times10^{9}$ cm^{-2} (for the sample grown on AlN/nPSS measured) of 3 µm thick samples grown by HVPE.
In addition, as discussed previously in chapter 2, the growth of samples on miscut substrates can lead to a reduction in the density of TDs as shown by Gkanatsiou et al.[178]. They demonstrated a decrease in the TD density for GaN layers from 9 $\times10^{9}cm^{2}$ to 3 $\times10^{9}cm^{2}$ as the substrate miscut angle was increased from 0° to 2°. Also, in a study to investigate the impact of miscut angle on the misorientation grain boundaries, Shen et al. [61] reported a decreased in the in-plane and out-plane grains misorientation of GaN samples with a miscut angle larger than 0.5° in addition to the reduction in the density of TDs.
In the present work, to explore the influence of the miscut angle on the morphological and structural properties of AlN/nPSS thin films, two samples grown on nano patterned sapphire substrates with different miscut angle were investigated (samples A, miscut angle ≈ 0.1° and sample B, miscut angle ≈ 0.2°), see table 6.1. The properties of sample A and sample B are summarised in Table 6.1.
In nPSS technology, the dimensions of the pattern are crucial. The pattern configuration with the film thickness influence the sample properties. For example, Zhang et al.[58] studied the impact of the hole size for nPSS patterned with holes with hole diameters of 300 nm, 450 nm, 650 nm, 800 nm respectively, on the properties of 6 µm thick AlN/nPSS samples. Their XRD measurements revealed that the narrowest

full width at half maximum (FWHM) was obtained for the sample with the hole diameter of 650 nm, which lead to conclude that the lowest misorientation (in-plane and out-plane) of sub-grain boundaries was obtained for this sample as well as the lowest density of TDs.

In the research reported here, to explore the influence of the pattern dimension size on the structural properties of AlN/nPSS thin films, three samples with a different top and bottom diameter of the pillars were investigated, sample C (≈ 250 nm and 400 nm respectively) and sample D (≈ 275 nm and 430 nm respectively) and sample E (≈ 310 and 460 respectively). The properties of samples C, D and E are summarised in Table 6.1.

6.2 Sample fabrication

In this chapter five samples are investigated and their structural properties and morphology are compared. All samples were grown using nanopillar nPSS (nano patterned sapphire substrates), briefly described in section 2.4.2. The samples were grown as described in Walde et. al. [63]. Figure 6.1.a demonstrates the growth process. First, the growth started on a 2-inch wafer. The metal nanodots mask were deposited on the sapphire by using displacement talbot lithography (DTL) and lift-off. The resulting array of nanopillars were transferred into the sapphire via dry etching in a chlorine solution. The overgrowth of AlN on nPSS has been done MOVPE reactor. The nanopillars are illustrated in scanning electron microscopy (SEM) image in figure 6.1.b and schematically cross-sectional in figure 6.1.c. The thickness of the samples is about 7 µm. To simplify, we can name the samples as sample A and B where the full description of the samples is listed in table 6.1. The table demonstrates that the sample A and B are similar in pillar dimensions (that the pillar height, bottom diameter, and top diameter are 260 nm,430 nm and 280 nm respectively) however the difference was in the miscut angles of the substrates, which are 0.1° and 0.2° respectively toward sapphire *m* plane. Sample C, D and E are similar in the miscut angle of 0.1° toward sapphire *m* plane and different in pillars dimensions (top and bottom diameters, see table 6.1). The sidewall of the pillars facets tilted by 75° towards the sapphire *c*-plane.[63, 64]

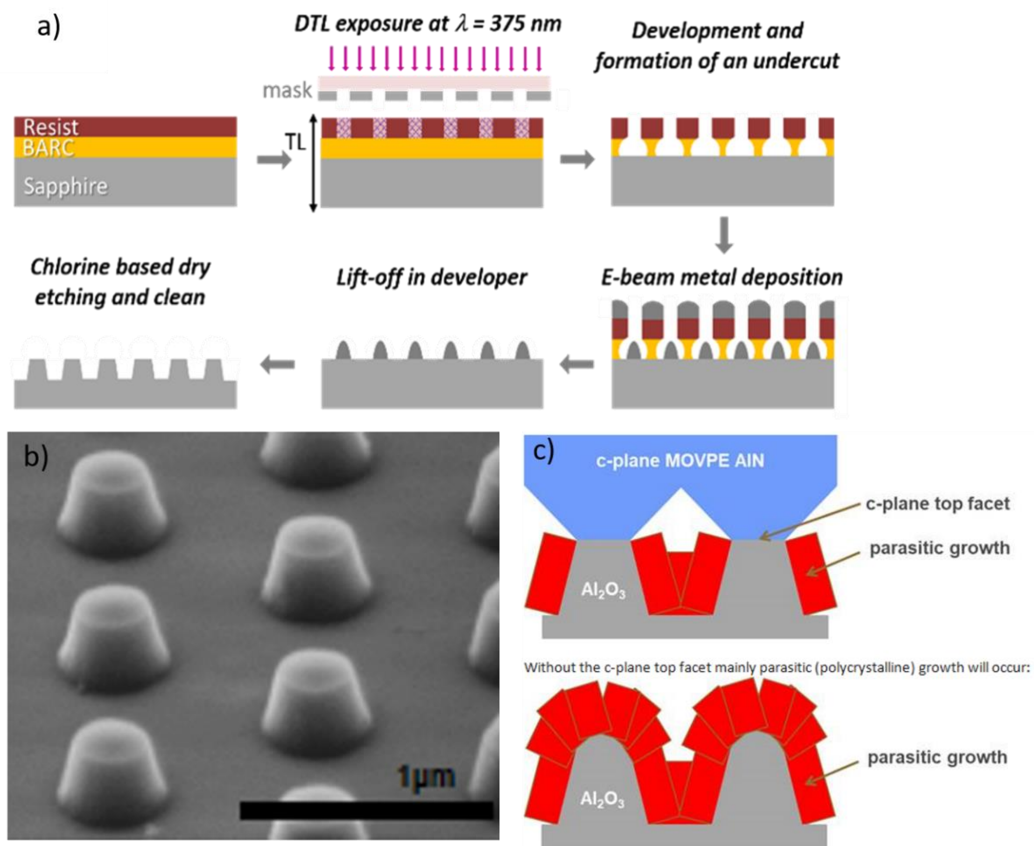

Figure 6. 1: a) Shows the process of nPSS fabrication (original from[63]), b) shows the SE image of nanopillars sapphire, c) scheme of the epitaxial growth of AlN on nPSS. b and c provided from the University of Bath and FBH.

	Sample No.	Substrate offcut towards sapphire *m*-plane (degrees)	Pillar height (nm)	Pillar bottom diameter (nm)	Pillar top diameter (nm)
Substrate miscut	A	0.1	260	430 ± 10 nm	280 ± 5 nm
	B	0.2	260	430 ± 10 nm	280 ± 5 nm
Pattern dimensions	C	0.1	310	400 ± 10 nm	250 ± 5 nm
	D	0.1	310	430 ± 10 nm	275 ± 5 nm
	E	0.1	310	460 ± 10 nm	310 ± 5 nm

Table 6. 1: The description of the samples studied in this chapter.

6.3 The experimental methods

ECCI and EBSD measurements were carried out using an FEI Quanta 250 environmental secondary electron microscope (ESEM). The ECCI and EBSD experimental setups were described previously in chapter 3. The EBSD system used here is Oxford Nordlys instruments. ECCI micrographs obtain by the off-axis gaseous secondary electron detector (off-axis GSED). MTEX software was used to generate EBSD maps.[179]

6.4 The influence of substrate miscut on AlN/nPSS thin films epilayer

6.4.1 The ECCI results

Figure 6.2 shows ECCI micrographs, acquired from areas of order 40 × 40 μm² in size, from Samples A and B, demonstrating the differences in their surface morphologies. Figure 6.2.a shows the surface morphology of sample A, revealing step bunches, hillocks, and sub-grains. The step bunches are described as bunches of monoatomic steps (indicated by yellow arrows), their height is generally several monoatomic steps higher. Sub-grains of different orientations are revealed as regions exhibiting different greyscale. In the same image, one can observe wide terraces between the step bunches. The length of the steps bunches are typically 6-7 μm long, no continuous steps bunches running across the whole sample were observed. The density of step bunches is measured to be ≈ 0.5×10^{3} cm^{-1}. By increasing the substrate miscut angle to 0.2° in sample B, the step bunches density increases to ≈ 1.5×10^{3} cm^{-1}. The ECCI micrograph (Figure 6.2.b) from sample B shows the steps bunches and sub-grains for this sample. The majority of the step bunches in this sample are continuous, running across the whole sample. As discussed previously (chapter 2, section 2.4) increasing the substrate miscut angle leads to a decrease in the distance between the step bunches, thus an increase in the density of the step bunches. For sample B, the minimum distance between step bunches was measured to be ≈ 3 μm. The step bunches height is measured by AFM to be ≈ 10 nm. [63]

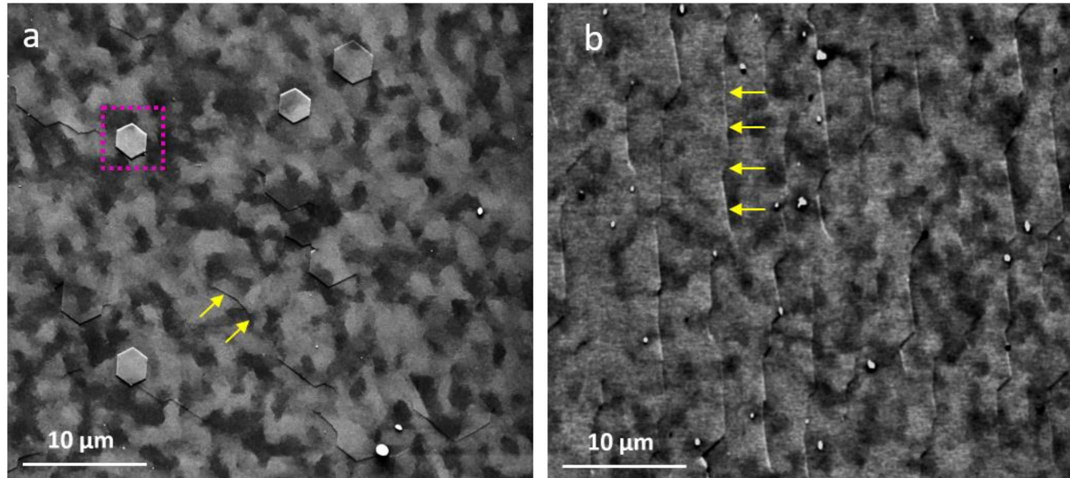

Figure 6. 2: Shows ECCI micrographs of sample A and B to illustrate the different surface morphologies, a) ECCI micrograph of sample A reveals small step bunches (indicated by yellow arrows), hillocks (inside the pink box), and sub-grains, b) ECCI micrograph of sample B demonstrates a higher density of step bunches compared to sample A. All images are acquired in the variable pressure SEM using off-axis GSED and under a beam of energy 25 keV, a gas pressure of 0.5 mbar and tilt of ≈50°

Figure 6.3 shows ECCI micrographs acquired at higher magnification, from areas of order 6 × 6 μm² in size, obtained from both samples. Figure 6.3.a shows an ECCI micrograph for sample A which distinctly shows the TDs as they are threading up to the surface with black-white contrast, and also shows sub-grains and monoatomic steps. At this point, one can notice arrays of TDs align up along the sub-grain boundary (inside the dashed yellow box). As the misorientation of these sub-grains is related to in-plane rotation, see section 6.6, the arrays of dislocations located at the boundaries are assumed to be pure edge dislocations with Burgers vectors perpendicular to the boundary plane. The observed black-white direction is consistent with the assumption in ref [37]. The density of TDs is measured at this magnification, and it is estimated to be 1.5×10^{9} cm^{-2} for this sample.

Figure 6.3.b is an ECC micrograph from sample B, The image shows the TDs, sub-grains, monoatomic steps and step bunches. Similar to sample A, pure edge dislocations align along the in-plane rotation boundaries. The density of TDs in this sample estimated to be 8×10^{8} cm^{-2}. In sample B, the terraces between the step bunches

contain several atomic steps (monoatomic steps) which were shown previously in ref. [59].

On comparing these two images, the dislocations located at the sub-grain boundary highlighted by the dashed yellow box in figure 6.3.a for sample A, have a higher density than the dislocations at the sub-grain boundary highlighted by the dashed yellow box in figure 6.3.b. Note also that the difference in greyscale for sub-grains on either side of the highlighted sub-grain boundary in sample A is clearly discernible, whereas the difference in greyscale for sub-grains on either side of the highlighted sub-grain boundary in sample B is barely discernible. This indicates that the misorientation between the sub-grains in sample B is smaller than in sample A. This observation is consistent with the observed difference in dislocation density, as the misorientation angle increases proportionally with the density of aligned dislocations. [180] However the observed differences in greyscale, while providing an indication of the magnitude of misorientation between the neighbouring sub-grains, does not provide a quantitative measure of their relative orientation, hence an EBSD measurement is required. EBSD measurements are discussed in section 6.6.

To confirm the ECCI results, especially in the case of sample B, results were compared to those obtained using the selective defect etching method, which was carried out by Walde et al.[63]. The techniques show complete agreement in the case of the TD density for sample A. In the case of sample B, there was a small difference in the density of TDs as it was found to be 9×10^{8} cm^{-2} by the selective defect etching method. The logical explanation of this small deviation between the results acquired by these two techniques, is that the contrast for TDs which line up at the step edge cannot be resolved with ECCI, as the step bunch contrast dominates in this case. While in the selective defect etching method, the dislocations which align along the step bunch edge appear as a line of pits see figure 6.4, the yellow rectangle highlights the dislocations that line up at the step bunch in sample B.

Also, it is well known from previous studies that increasing the miscut angle leads to an increase in surface roughness. [71, 181] The samples' surface roughnesses were measured by Walde et al. [63] with AFM. Sample A (miscut 0.1°) has a root mean square (rms) roughness value of 0.9 nm and for sample B (miscut 0.2°) it was 3.7 nm.

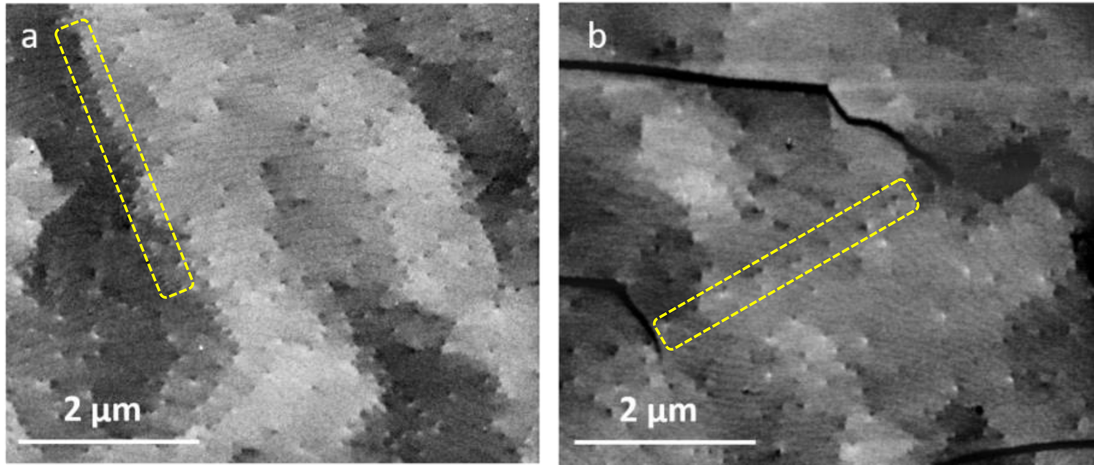

Figure 6. 3: Show ≈6 × 6 µm² ECCI micrographs of the sample A and B, a) high magnification image of the sample A that shows a closer look at the TDs (dots with black-white contrast) and sub-grains, b) high magnification image of the sample B that show TDs, sub-grains and step bunches. Both images were acquired in the variable pressure SEM using off-axis GSED and under a beam of energy 25 keV, a gas pressure of 0.5 mbar and dwell time 100µs, and tilt ≈ 50°. The yellow rectangles highlight TDs that align with sub-grain boundaries.

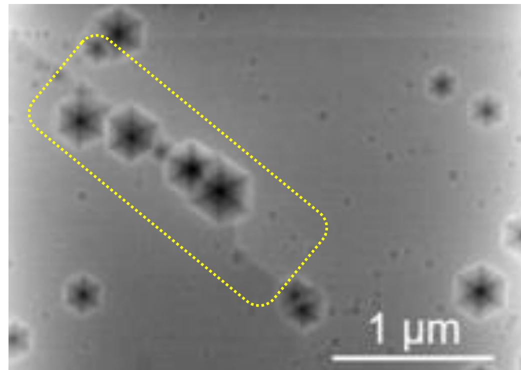

Figure 6. 4: Demonstrating the selective defect etching method image. The image was obtained from sample B, where the yellow rectangle surrounds the dislocations that align with the step bunch.

6.4.2 Identification of TDs

Two ECCI micrographs were obtained from the same area under different diffraction conditions to identify the types of TDs through monitoring the direction of the black-white contrast under different diffraction conditions as described in Chapter 3, figure 3.13. The application of this method was made more difficult for these samples as the second image was generally of poorer quality as a result of carbon contamination after the first scan.

The majority of dislocations in both samples were identified as pure edge dislocations. Measurements revealed that for sample A approximately 90% of the dislocations are pure edge. 8% of them were identified as screw/ mixed dislocations, while the remaining 2% could not be identified due to the poor quality of the second image.

On increasing the substrate miscut from 0.1° to 0.2° i.e., for sample B, the percentage of edge dislocations decreased to 70%. 25% were identified as screw/mixed dislocations and the remaining 5% were undefined due to poor image quality. In general, for AlN thin films, the percentage of screw component dislocations is found to be significantly lower than the percentage of edge dislocations. [58]

In addition, TDs can be identified using selective defect etching where the smaller pits are attributed to edge dislocations, and the bigger ones are attributed to dislocations with a screw component. [182] This is illustrated in figure 6.5; yellow circles indicate pits related to the edge dislocations and the big green circles to dislocations with a screw component. For both samples (sample A and B) there is a good agreement between ECCI and the selective defect etching method in determining the relative percentages of edge and screw component dislocations.

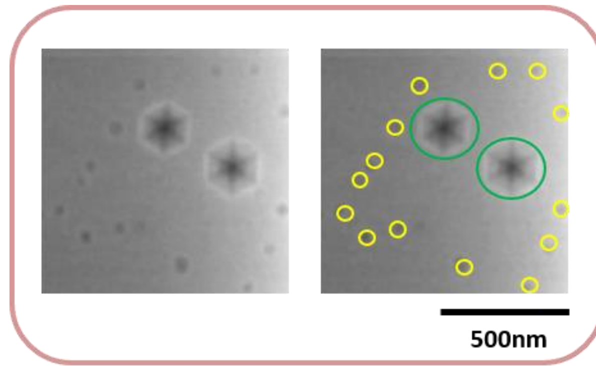

Figure 6. 5:Illustrates the identification of TDs by a selective defect etching method. The right image is marked to indicate the types of dislocations. Yellow small circles indicate edge dislocations while the big green circles indicate screw component dislocations. This image was acquired from sample B.

6.4.3 The impact of step bunches on TDD

The reduction of TDD for sample B in comparison to sample A, can be related to the greater density of step bunches in sample B which was explained previously in chapter 2 section 2.4.3. The reduction of TDs in sample B is attributed to those inclined dislocations that meet with the vertical ones and either annihilate each other, form dislocations loops leading to reduction of dislocations density or end up aligning at the step bunches edge as Walde et al.[63] show for sample B. Figure 2.12 shows the TDs reduction mechanism, the interaction of the inclined and the vertical dislocations.

Shen et al.[183] demonstrated previously that the edge dislocations tend to incline toward the step bunches which can lead to two dislocations to interact with each other and either annihilated each other (if they have opposite Burger's vectors) or form a single dislocation (if they have different Burger's vector). The edge dislocations tend to incline toward $\langle 11\bar{2}0\rangle$ and $\langle 1\bar{1}00\rangle$ directions which are the slip planes for edge dislocations. Also, mixed dislocation can be expected to bend because of their edge components. While screw dislocations do not tend to bend toward $\langle 11\bar{2}0\rangle$ and $\langle 1\bar{1}00\rangle$ directions and commonly thread vertically toward [0001]. [184] The role of step bunches more likely affect the density of edge dislocations which is consistent with the ECCI results where the step bunches inverse proportional with the pure edge

density. The growth on the miscut substrate can be used as a method of dislocation reduction.

6.5 The influence of pattern dimension on AlN/nPSS thin films epilayer

To study the influence of the substrate pattern configuration, I studied three samples with a different top and bottom pillar diameter with the same substrate miscut of about 0.1°, see table 6.1. Figure 6.6 shows ECCI micrographs ≈10×10 μm^2 acquired from these samples. Sample C (see figure 6.6.a) has the top and bottom diameter of the nanopillars around 250 and 400 nm respectively and exhibits a high density of step bunches that run across the whole sample in comparison to the other two samples. It has a step bunch density of 4×10^3 cm^{-1} with a minimum terrace width measured to be around 2 μm. Figure 6.7.a shows a higher magnification ECCI micrograph (6×6 μm^2) which shows TDs and sub-grains, atomic steps and step bunches. The yellow box highlights TDs on the boundary of the sub-grain. The total density of dislocations was found to be 5×10^8 cm^{-2}. The red arrows indicate curved atomic steps which tend to follow spiral growth. This is more obvious in the high magnification ECCI micrographs of figure 6.8 that was obtained from the same sample.
By increasing the top and bottom diameters of the nanopillars to be around 275 nm, and 430 nm respectively, one can notice a decrease in the density of step bunches in sample D (figure 6.6.b ≈10×10 μm^2 in size) with a minimum terrace width of ≈ 4 μm. The density of the step bunches was found to be 1×10^3 cm^{-1}. The length of the step bunches is about ≈ 2-20 μm, lower in comparison to sample C. The ECCI micrograph shown in figure 6.7.b was acquired with higher magnification with an image size of ≈6 × 6 μm^2. The image reveals TDs with black-white contrast, it also shows sub-grains and monoatomic steps. The density of TDs in this sample is estimated to be 1×10^9 cm^{-2}, which is higher when compared to sample C. The sub-grain in the middle of the image (inside the yellow box in figure 6.7.b) is surrounded by numbers of TDs, their black-white contrast and alignment are consistent with the majority of them being pure edge dislocations. As in the previous section, TDs types were identified by obtaining two images from the same area under different diffraction conditions. The pure edge dislocations were found to be 80% of the total TDs. The increase in TD density in this

sample, when compared to sample C, is a result of the reduction of step bunches density in this sample. As in the previous section, it can be concluded that introducing step bunches effectively reduces the TD density, most likely the density of pure edge dislocations.

Figure 6.6.c shows an ECCI micrograph ≈10×10 μm^2 size obtained from sample E. In this sample, the top and bottom diameters of the nanopillars are increased to be around 310 nm and 460 respectively. The step bunches is reduced to be 5.4×10^2 cm^{-1} with wide terraces and the length of step bunches is ranging between 4-20 μm. Figure 6.7.c is an ECCI micrograph from sample E in high magnification which shows the atomic steps and TDs. The total density of dislocations is higher than sample C and D and measured to be around 1.2×10^9 cm^{-2}.

This section is showing possible evidence of the impact of the pattern dimensions on the formation of step bunches. As the substrate for all three samples had the same miscut, the changing in the density of step bunches appears to be due to the changing of the nanopillar diameters. Clearly, there is an inversely proportional relation between the density of TDs and step bunches as previously demonstrated in section 6.4.

In addition, the ECCI micrographs from sample C indicate spiral growth that is usually observed in III-nitrides grown in an MBE reactor [185] and under different growth conditions (e.g. thick samples, low growth temperature, growth rate, etc), see figure 6.8 this also a close look on the spiral from sample C (inside the dashed yellow box). The formation of the spirals is attributed to screw dislocations that terminate steps. [186]

The observed differences in step bunch density may be as a result of slight changes in the growth temperature or in the substrate miscut (all these samples were grown on the same wafer). There is presently no other literature reporting a relationship between the feature size and the formation of step bunches. However, this work does confirm the relationship between the density of TDs and the density of step bunches.

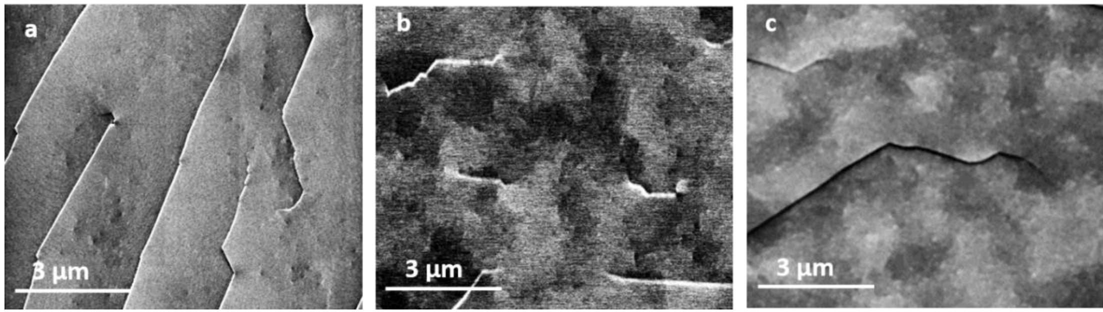

Figure 6. 6:Shows 10×10 µm² ECCI micrographs of the samples C, D and E a) sample C exhibits continuous step bunches across the sample b) sample D exhibits small step bunches covering the sample surface c) sample E has a lower density of step bunches in comparison to sample C and D. All images were acquired in the variable pressure SEM using off-axis GSED and under a beam of energy 25 keV, a gas pressure of 0.5 mbar and dwell time 100µs, and tilt ≈ 50°.

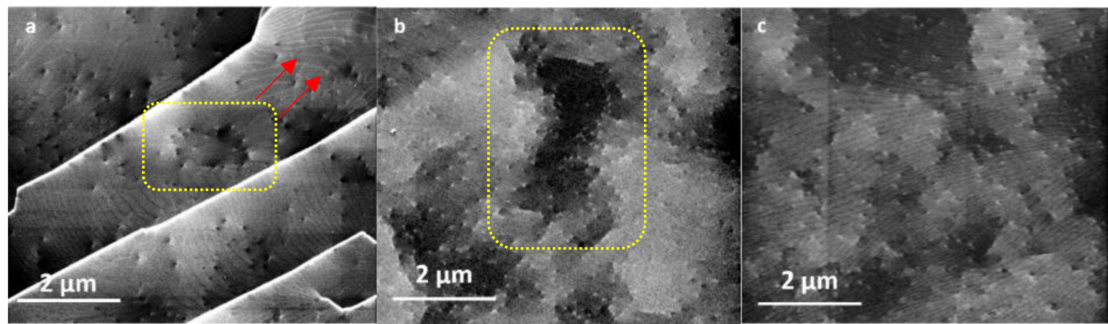

Figure 6. 7: Shows ≈6 × 6 µm² ECCI micrographs of the samples C, D and E a) high magnification image of sample C that shows a closer look at the TDs (dots with black-white contrast), sub-grains, atomic steps and step bunches b) high magnification image of sample D that show TDs, atomic steps and sub-grains. c) high magnification image of the sample D that show TDs, sub-grains and atomic steps. All images acquired in the variable pressure SEM using off-axis GSED and under a beam of energy 25 keV, a gas pressure of 0.5 mbar and dwell time 100µs, and tilt ≈ 50°. The yellow rectangles highlight TDs that align with sub-grain boundaries.

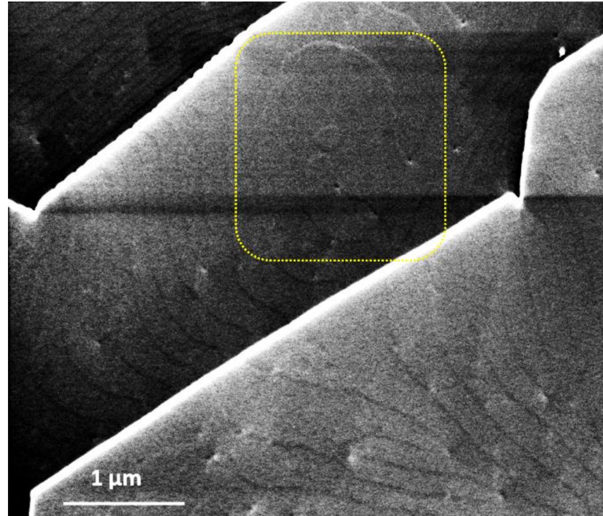

Figure 6. 8: ECCI micrograph from sample C that shows the spiral growth in this sample, the yellow box surrounds the spiral.

6.6 Measurement of misorientations in AlN/ nPSS thin films using EBSD

This section aims to investigate the misorientations in samples A, B, D, discussed earlier in this chapter, using electron backscatter diffraction (EBSD). The aim was to investigate the relationship between misorientation and TD density. Sample A is utilized as a reference sample. Sample B has a different miscut and sample D has a different pillar height compared to sample A.

As discussed above, ECCI micrographs provide us with qualitative information on sub-grains, but do not provide any quantitative information on the magnitude or direction of the misorientation of sub-grains. Thus EBSD was required to extract this information. Figure 6.9 illustrates EBSD maps which are obtained under low vacuum (≈ 0.4 mbar) where the accelerating voltage was 20 keV.

The EBSD analysis starts with the pattern matching of the experimental EBSP to the dynamically simulated patterns using the Bloch wave approach. [187, 188] EBSD maps were then produced using MTEX software [189], in this project grain reference

orientation deviation (GROD) maps were produced. Grain reference orientation deviation (GROD) maps provide us with grain misorientations with respect to a specifically selected reference orientation. [190]

Figure 6.9.a, b and c show grain reference orientation axis maps with respect to the sample normal (Z-axis) (GROD-Z) for sample A, B and D respectively. These maps identify the orientation direction of sub-grains with respect to the normal axis of the sample (which is the c-axis or [0001] direction, neglecting the miscut). In these maps, the red and blue colours indicate the direction of the sub-grains in-plane rotation, where the blue and red regions rotate in opposite directions around the c-axis.

From indexed electron backscatter patterns (EBSPs) (see figure 6.10) the step bunches in sample B and D are found to be aligned approximately with the $[11\bar{2}0]$ direction. Figure 6.10.a shows an experimental EBSP acquired from sample B. The ECCI micrograph in figure 6.10.b was obtained coincidently with the EBSP, thus allowing the step bunch direction to be estimated. Figure 6.10.c is the dynamically simulated EBSP that was used to index the experimental EBSP. Figure 6.10.d shows some indexed planes highlighted on a kinematically simulated pattern. Previous studies have shown that the direction of the step bunches are independent of the substrate miscut direction. Bryan et al. [191], studied step bunches in AlN grown on miscut sapphire substrates and found that their direction aligned perpendicular to the AlN $[1\bar{1}00]$ direction. They showed that the sample grown on the substrate with the miscut toward the sapphire *a*-plane, exhibited step bunches with straight edges. While in the case of AlN grown on a substrate miscut toward the sapphire *m*-plane, it exhibited step bunches with zigzag edges. Similarly in ref.[192], the growth of GaN layers on two substrates with different miscut direction, revealed that the miscut direction only affected the step bunches edges not their direction. They demonstrated that GaN grown on miscut sapphire, with the miscut toward the sapphire *a*-plane, resulted in step bunches with straight edges, growth on sapphire with a miscut toward the sapphire *m*-

plane resulted in step bunches with zigzag edges. Both studies confirmed, as observed here, that the step bunches lie parallel to the $[11\bar{2}0]$ nitride direction.

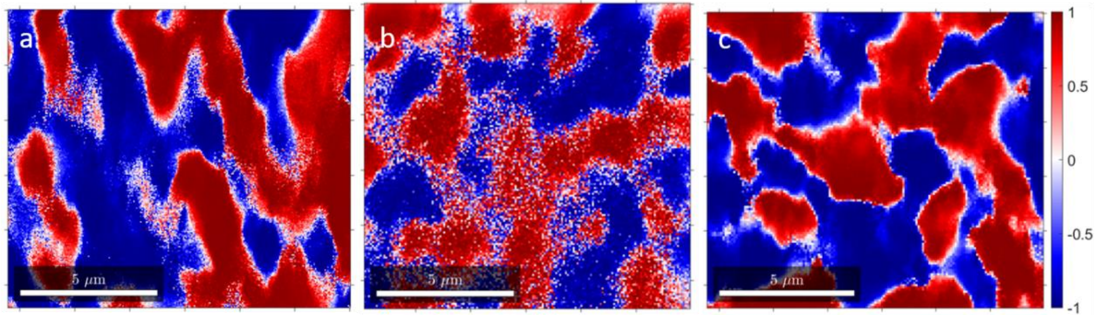

Figure 6. 9: The grain reference orientation deviation (GROD) maps with respect to the sample normal (Z-axis) which is the c-axis/[0001] direction. That is GROD-Z maps obtained from a) sample A, b) sample B and c) sample D. The colours indicate rotations of the opposite direction. These maps were extracted from EBSD data using MTEX software.

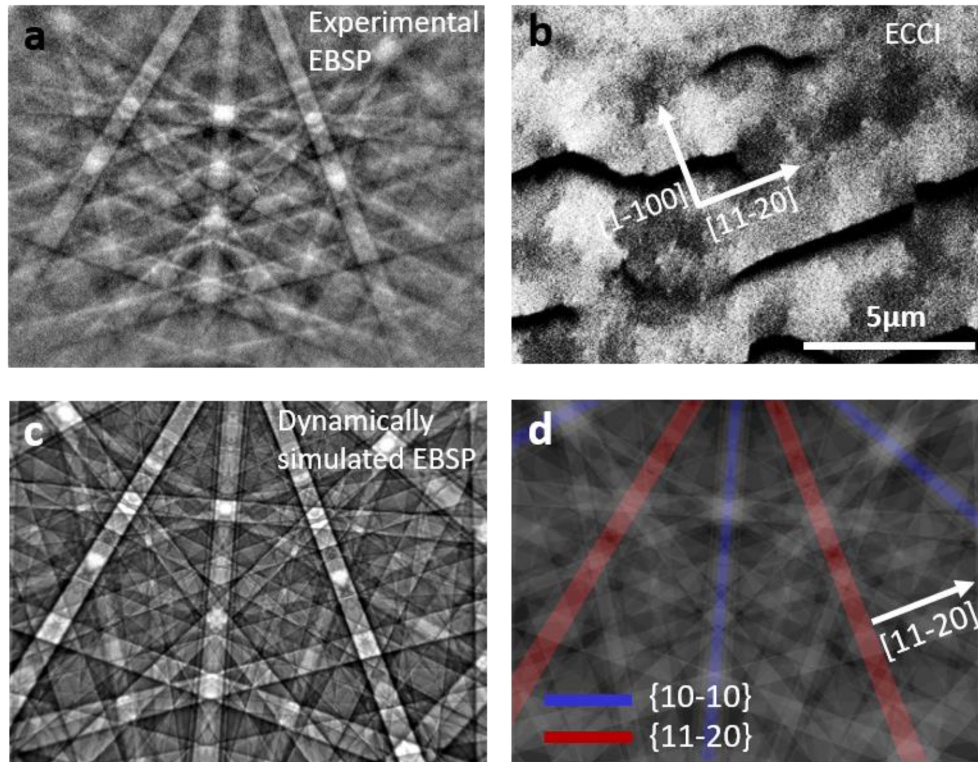

Figure 6. 10: Shows a) an experimental EBSP b) ECCI micrograph from sample B exhibiting step bunches and showing that they lie along the $[11\bar{2}0]$ direction. c) A dynamically simulated EBSP. d) indexed EBSP highlighting the Kikuchi bands for the $(10\bar{1}0)$, $(11\bar{2}0)$ planes and $[11\bar{2}0]$ direction.

Figure 6.11. a, b and c are the grain reference orientation deviation (GROD) maps for sample A, B and D respectively. It is clear from figure 6.11 that sample A has the highest misorientation followed by sample B then sample D. The maximum misorientations angle of the AlN epilayer is found to be around 0.5°, 0.3°, 0.2° for samples A, B, and D respectively, see figure 6.11.d which shows GROD angle distribution for sample A, B, and D. It is worth to mention that the average misorientation angle for all samples is measured to be ≈ 0.05°as the graph in figure 6.12.d clearly demonstrates. If we consider the density of TDs of all samples, a conclusion can be made that the density of TDs does not affect the average misorientation however, it affects the maximum misorientation angle. This conclusion can be related to the previous ECCI results. The dislocations located at the sub-grain

boundary highlighted by the dashed yellow boxes in figure 6.3.a, 6.3.b and figure 6.7.b. By comparing these three ECCI micrographs, it is clear that the density of TDs at the sub-grain boundary in sample A (inside yellow box in figure 6.3.a) is higher than the density of TDs at the sub-grain boundary highlighted by the dashed yellow box in sample B (figure 6.3.b) and sample D (figure 6.8.b). This result is consistent with the previous mention in 6.4, the sub-grain boundary misorientation angle increases proportionally with the density of aligned dislocations.

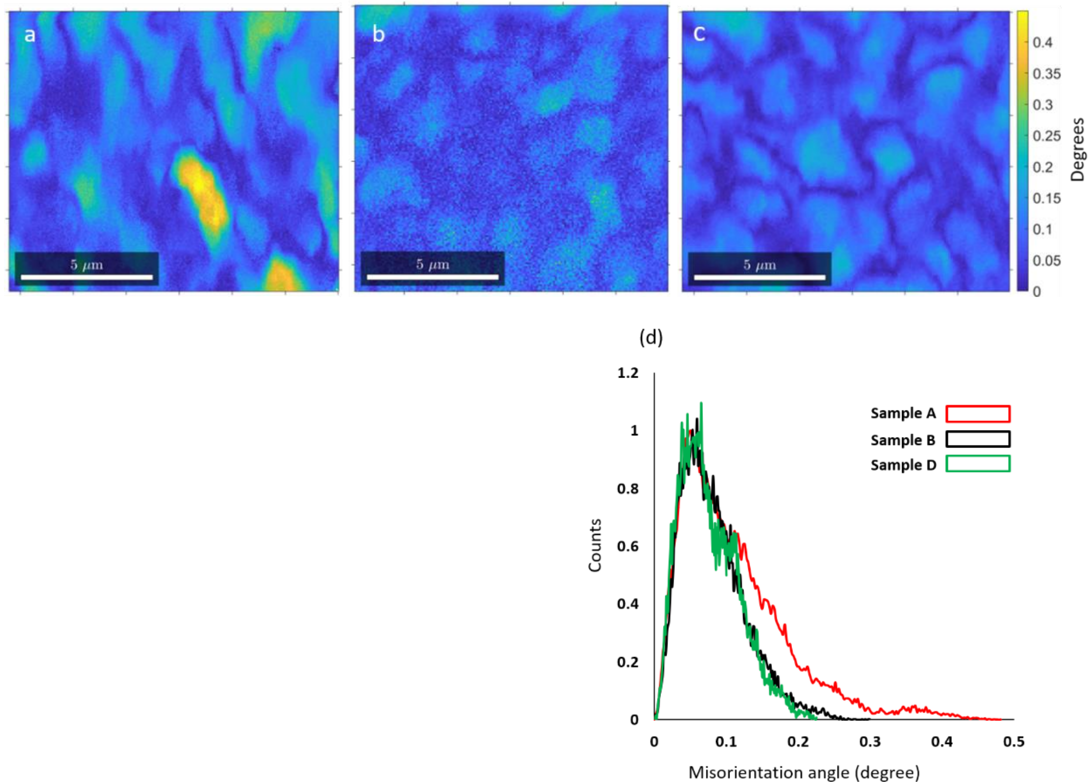

Figure 6. 11: Grain reference orientation deviation (GROD) maps for; a) sample A, b) sample B and c) sample D. d) GROD angle distribution for sample A, B, and D.

Coincident ECCI and EBSD

An ECCI micrograph and an EBSD map were obtained from the same part of sample D under the same diffraction condition. Firstly an ECCI micrograph was obtained then an EBSD map, see figure 6.12. The ECCI micrograph in figure 6.12.a shows clearly that the deviation in grayscale (or sub-grain contrast). Where figure 6.12.b is the ECCI micrograph with the reversed contrast. The EBSD maps in figure 6.12.d and e are GROD -X and GROD-Y maps that illustrate the rotation around X and Y directions respectively. While the EBSD map in figure 6.12.f is a GROD-Z map that illustrates the in-plane rotation around the c-axis as shown previously in figure 6.9.c. Finally, figure 6.12.g shows the GROD-AXIS map that shows all rotations in the sample, where the figure 6.12.h is the colour key for this map.

Comparison between 6.12.a and 6.12.f, reveals that the red sub-grains in the EBSD map correspond to the sub-grains exhibiting a lighter greyscale in the ECCI micrograph, while the blue sub-grains in the EBSD map correspond to the darker sub-grains in the ECCI micrograph (the deviation in grayscale is consistent with the in-plane rotation). Hence, an ECCI micrograph obtained at this geometry can give us information about the direction of the sub-grains rotation is combined with EBSD.

On inspection of the map of figure 6.12.g, which shows the GROD-AXIS map, note that the black and white regions are those exhibiting a purely in-plane rotation, and note the correlation with the blue and red regions in the GROD-Z map. The GROD maps d-g indicate that the dominant misorientation is in-plane rotation around the Z-axis (c-axis); the GROD-Z axis map show greater misorientation than the GROD-X and the GROD-Y maps and significant areas of the GROD-AXIS map shows significant areas of purely in-plane rotation.

The reverse contrast ECCI micrograph in figure 6.12.b is to show the dislocations that are invisible in figure 6.12.a. It is clear from this image, the majority of TDs are on sub-grain boundaries (inside the yellow box in figure 6.12.b) and are more likely pure edge, as revealed previously in the high-resolution ECCI micrograph in figure 6.7.b. Figure 6.12.c shows the directions in III-nitrides.

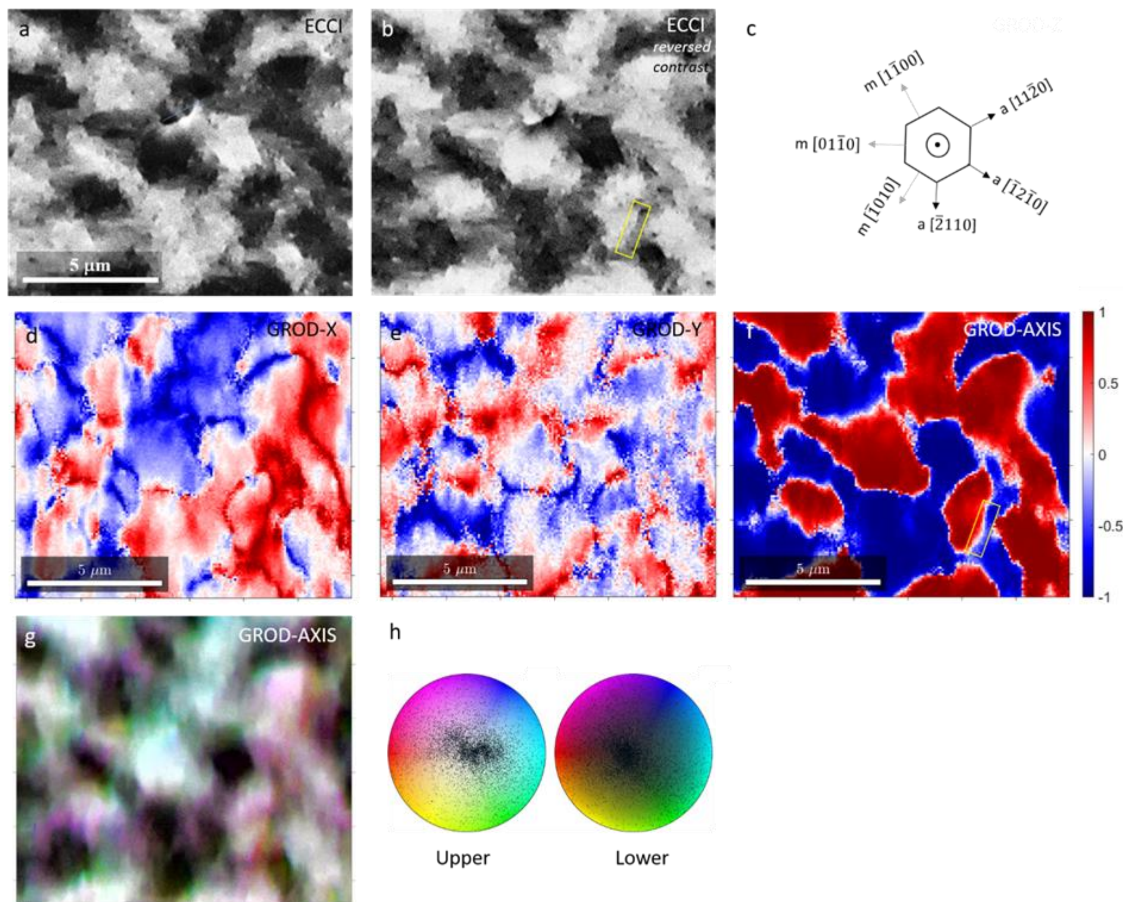

Figure 6. 12: Illustrates coincident EBSD and ECCI micrographs acquired simultaneously under the same diffraction condition from sample D a) ECCI micrograph with deviation in greyscale related to the deviation in sub-grain orientation, b) the ECCI micrograph with the reversed contrast, c) directions (derived from EBSP) d) GROD-X map that shows the out-of-plane rotation around the *x*-axis (approximately in an *a*-direction), e) GROD-Y map that shows the out-of-plane rotation around the *y*- axis (approximately in an *m*-direction), f) GROD-Z map that shows the in-plane rotation around z-axis (c-direction). In maps d to f, red and blue indicate opposite directions of rotation g) GROD-axis map, the colours (see colour key) indicate the rotation axis, where the black and white regions are those exhibiting a purely in-plane rotation, note the correlation with f. h) colour key for g).

In addition, it is possible to reproduce multiple micrographs by using the EBSD screen itself as a virtual diode. [193] It can be used as a virtual forescatter/backscatter detector. Figure 6.13.a is the EBSD pattern and the dashed yellow box is the area of interest for which the total intensity was calculated for each EBSP. While the image in figure 6.13.b is the image that is produced on plotting the intensity, an image is produced which is very similar to the ECCI micrographs of figure 6.12 with dislocations and the sub-grains revealed. This contrast is understandable if we think about the different forescatter diodes that are mounted around the EBSD screen, the diodes located below the EBSD screen produce the best diffraction/structural contrast. [193] The image in figure 6.13.b is obtained used software that is written by Aimo Winkelmann and it was provided to me by Kieran Hiller.

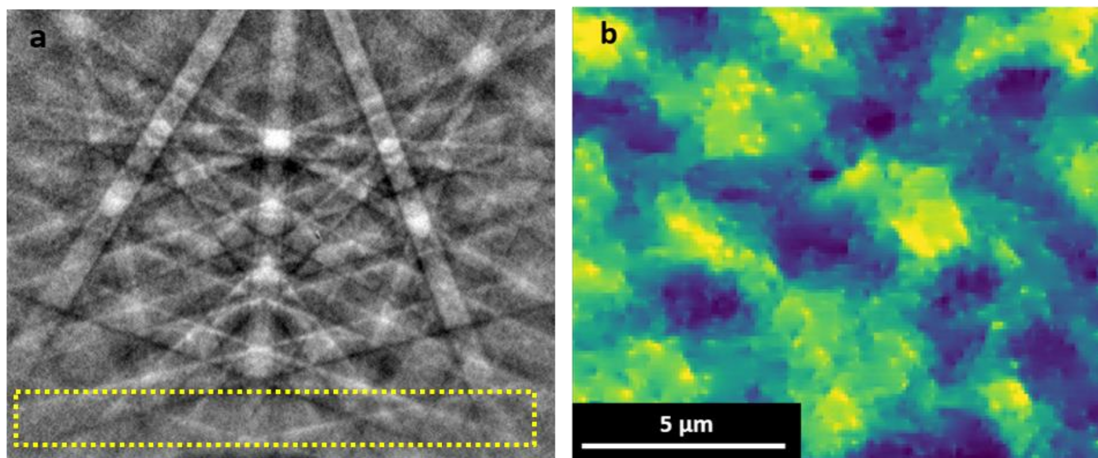

Figure 6. 13: a) The experimental EBSP, b) BSE signal from the bottom area of EBSP in a (surrounded by the dashed yellow box) diffraction contrast dominates revealing dislocations. Images here are exactly from the same area that the ECCI micrograph and EBSD map have acquired in figure 6.12.

6.7 Summary

In conclusion, this chapter demonstrates the utilization of ECCI and EBSD as complementary techniques to study AlN thin films produced by MOVPE overgrowth on nano patterned sapphire substrates (nPSS): AlN/nPSS thin films. In particular, it reports on the effect of two parameters on the structural properties of the AlN/nPSS thin films. These parameters are the substrate miscut and the nano patterned substrate dimensions. In the case of the first parameter, by increasing the substrate miscut from 0.1° to 0.2°, SEM and ECCI revealed the step bunch density in the AlN/nPSS increased from 5×10^2 cm^{-1} to 1.5×10^3 cm^{-1} and the TDD was reduced from 1.5×10^9 cm^{-2} to 8×10^8 cm^{-2}. While in the second case, the influence of the nanopillar dimensions, specifically pillar diameter, was explored through three samples. The step bunch density was also observed in sample C ≈ $4\times10^3 cm^{-1}$, in sample D ≈1×10^3 cm^{-1} and sample D ≈ 5×10^2 cm^{-1}. In addition, the density of dislocations found to 0.5×10^9 cm^{-2} for sample C, 1×10^9 cm^{-2} for sample D and 1.5×10^9 cm^{-2} for sample E. It is confirmed through ECCI measurements that the relationship between the density of step bunch and the density of TDs, as the step bunch density increase the density of TDs decrease. See Table 6.2 which briefly shows the result from all samples (A, B, C, D and E). In addition, an EBSD was required to obtain the misorientation through sample A, B, and D. From the GROD-Z map the dominate sub-grain orientation was in-plane rotation around the c-axis, for all three samples (A, B, and C). The maximum of the sub-grain misorientation angle was proportional to the density of TDs. The sub-grains maximum misorientation angles have been measured to be ≈ 0.5°, 0.3°, 0.2° for samples A, B and D respectively. Also, the ECCI and EBSD were combined simultaneously under the same diffraction condition from sample D, thus the contrast in ECCI micrograph at the forescatter geometry was related to sub-grains in-plane rotation as the EBSD result illustrated. Finally, this chapter revealed the possibility of using EBSD as a virtual diode to produce an ECCI-like micrograph.

Samples	Dislocation Density × 10^9 cm^{-2}	Percentage *a*-type dislocations	Density of step bunches ×10^3 cm^{-1}	Average misorientation	Maximum misorientation
A	1.5	90	0.5	≈ 0.05°	≈ 0.5°
B	0.8	70	1.7	≈ 0.05°	≈ 0.3°
C	0.5	--	4	Future work	Future work
D	1	80	1	≈ 0.05°	≈ 0.2°
E	1.2	--	0.5	Future work	Future work

Table 6. 2: Shows the result summary of all three samples.

Chapter 7

Conclusions and future work

7.1 Techniques and samples:

This thesis presents experimental work on the characterisation of III-nitride materials using the scanning electron microscope. Two complementary techniques were used in this study to explore the material's structural properties; electron channelling contrast imaging (ECCI) and electron backscatter diffraction (EBSD). In addition, other techniques were combined with ECCI, such as atomic force microscopy (AFM) measurements which were provided by Dr. Tom O'Hanlon from the University of Cambridge and the etching pits method provided by Dr. Sebastian Walde from the Ferdinand-Braun-Institute, Leibniz-Institut fuer Hoechstfrequenztechnik (FBH) in Berlin. A number of samples grown using different techniques were investigated in this thesis. The GaN sample in chapter 4, 'Using ECCI and AFM to study ELOG GaN', demonstrated the capability of ECCI in resolving inclined dislocations. In order to better examine insulating samples such AlN, chapter 5 "ECCI in a variable pressure scanning electron microscope'' describes the benefits of using a gaseous secondary detector to obtain ECCI micrographs. In Chapter 6, "Characterisation of AlN/nPSS thin films in a SEM'', a series of AlN samples grown on nano patterned (nanopillars) sapphire substrates (nPSS) were investigated to study the impact of the substrate miscut and the nano pattern dimensions on structural defects and the sample morphology.

7.2 Coincident ECCI and AFM of threading dislocations in ELOG GaN

In chapter 4 "ECCI and AFM were both used to reveal threading dislocations in ELOG GaN'', a GaN sample grown on sapphire using an ELOG stripe pattern, where the stripes were parallel to the GaN $[1\bar{1}00]$ direction. The ELOG stripe pattern introduced open and closed regions to the sample (referred to here as window and wing regions respectively), which are used to filter the threading dislocations (TD) and reduce their density, as TDs are blocked under the wing region and propagate through the window. There was one to one correlation of the dislocations revealed independently by AFM and ECCI. The density of dislocations was reduced in the wing area in comparison to the window region. The average density of TDs in the seed region is $4.2 \pm 0.7\times10^{8}$ cm^{-2} while in the wing region it is $1.3 \pm 0.1\times10^{8}$ cm^{-2}.

ECCI analysis was also able to reveal inclined dislocations in these samples. ECCI micrographs show that the inclination direction of the inclined dislocations in the window region (opening region of mask) was perpendicular to the stripes, in the $[11\bar{2}0]$ direction as expected. An inclination angle of order 45°- 63° was tentatively estimated for these TDs. The inclination direction of the TDs in the wing region (closed region of the mask) is towards the $[0\bar{1}10]$ direction; that is at 60° degrees to the stripe. In this case the inclination angle is thought to be driven by strain relaxation. A series of ECCI micrographs were also acquired to investigate the nature of the TDs at the coalescence region in the middle of the wing region. The majority of the TDs were found to be edge dislocations with a Burgers vector of $\frac{1}{3}[11\bar{2}0]$ or $\frac{1}{3}[\bar{1}\bar{1}20]$.

7.3 ECCI in the gaseous environment for characterization of insulating samples

Chapter 5 presents results which show for the first time that ECCI micrographs can be produced using gaseous secondary electron detectors (GSEDs) in a variable pressure scanning electron microscope [194], where ECCI micrographs were acquired at pressures ranging from 0.3 mbar to 1 mbar. This is done by detecting the amplified

secondary electron signal, indicating that the intensity of the detected secondary electrons are modulated as a result of the diffraction of the incident electron beam. This means that the charging problem, inherent when analysing non-conducting AlN, is eliminated and the quality of the ECCI micrograph is improved. The use of the GSEDs for acquiring ECCI micrographs allowed ECCI micrographs to be acquired over a wide range of angles. In this chapter, different parameters such as gas pressure, detector bias, sample geometry, and scan rate in terms of image quality are examined. In the present thesis, the best conditions for acquiring ECCI micrograph by off-axis GSED can be listed as follows; the gas pressure was around 0.5 mbar for ECCI micrographs (used in chapter 6). The detector bias should be kept large, not lower than 90% (≈ 230V). The use of the GSEDs for acquiring ECCI micrographs allowed ECCI micrographs to be acquired over a wide range of angles (from 0° to 70°). The long scan rate improved the signal to noise ratio in all acquired images in chapter 6 which by eliminating the noise. In addition to some of those parameters, the sample current (ion current) was also analysed with respect to these parameters.

7.4 Characterisation of AlN/nPSS thin films by SEM

In chapter 6 "Characterisation of AlN/nPSS thin films in a SEM'', the structural properties of two series of AlN samples grown on nPSS (patterned with nanopillars) by FBH and the University of Bath were studied. In section 6.4 the influence of the substrate's miscut on the structural and morphological properties were investigated. The substrate miscut led to the formation of step bunches. Their density increases as the substrate miscut increases. The impact of the step bunches on the density of TD was illustrated in section 2.4.3 and confirmed by the ECCI results presented in chapter 6. The density of dislocations decreases as the density of step bunches increases. The next series of samples studied the impact of pattern dimensions on the sample's structural and morphological properties. It included three samples with different nanopillar diameters. The samples with the smallest pillar diameter exhibited the highest density of step bunches and the lowest density of TDs, the higher the pillar diameter, the higher the density of step bunches and the lower the density of TDs. In sections 6.4 and 6.5 the ECCI micrographs reveal sub-grains that result from

misorientation throughout each sample. As ECCI micrographs only provide qualitative information, EBSD was used to study and quantify sub-grain misorientation. In section 6.6, EBSD data is shown for three samples; sample A was used as a reference, sample B had a different substrate miscut, and sample D had a different pillar height compared to sample A. EBSD data revealed that the dominant misorientation is a rotation around the z-axis because the GROD-Z map shows greater misorientation than the GROD-X and the GROD-Y maps. Sample A has the highest density of dislocations and exhibits higher misorientation in comparison to the other two samples as seen in the GROD maps. For all the samples, the average misorientation was ≈ 0.05°. The maximum misorientation angles for sample A was ≈ 0.5° while for sample B was ≈ 0.3° and for sample D was ≈ 0.2°. These angles are proportional to the measured density of TDs (edge dislocations).

Comparing EBSD and ECCI results from the same area of sample D, showed the sub-grains revealed in the ECCI micrograph correlated with the sub-grains revealed in the GROD-Z map extracted from EBSD data. Finally, ECCI-like micrographs showing sub-grains and dislocations were produced from the EBSD data where the EBSD screen was used as a virtual diode to obtain an orientation contrast image.

7.5 Future work:

The following lists of future work to extend the research reported in Chapters 4-6.

Chapter 4:

1. Cross-sectional TEM of the ELOG sample to confirm the inclination direction and angle of both wing and window regions.
2. EBSD may be used to quantify misorientation and strain. Comparing coincident ECCI micrographs with EBSD maps will allow the origin of greyscale contrast observed in the ECCI micrographs to be determined.

Chapter 5:

3. Explore the quality of ECCI micrographs obtained in a variable pressure scanning electron microscope when utilising other environmental gases such N_2, CO_2 , etc.

Chapter 6:

4. Study the sub-grain misorientation in AlN/nPSS samples by taking into account the substrate miscut angle. This can be accomplished by obtaining EBSPs from the substrate and the AlN epilayer and determining the relative misorientation of the epilayer with respect to the substrate. A previous study [195] has found that the misorientation in the GaN epilayer is smaller than in the substrate miscut.
5. Previously, an attempt was made to acquire ECCI micrographs and coincident EBSD maps under different diffraction conditions. However, this experiment failed as carbon contamination affected the quality of EBSD maps and ECCI micrographs. To overcome this issue, plasma cleaning is required after obtaining ECCI and EBSD.
6. As there are no extensive studies on the impact of the nPSS pattern dimensions on the structural properties of the overgrown epilayers, it would be useful to obtain EBSD data from samples C and E as described in Chapter 6 to provide misorientation data on a group of samples with a range of nPSS pillar diameters. Acquiring EBSD simultaneously with ECCI from sample C and E then comparing this data with the data obtained from sample D would also be a useful exercise.
7. Walde et al.[63] studied the optical properties of two AlGaN samples that were grown on samples A and B. A new research can be done on those AlGaN samples to investigate their structural and morphological properties by combining ECCI and EBSD. It will be worth to study the impact of step bunches in the substrate (AlN/nPSS layer) on the AlGaN epilayer structural properties.

List of figures

Figure 2. 1: Bandgap energy (E_g) versus lattice constant (a) of wurtzite III-nitrides 16

Figure 2. 2: a) The wurtzite structure of AlN, GaN and InN at room temperature adapted from [11], b) Illustrates the planes of the wurtzite crystal c-plane (0001), a-plane (1120), m-plane (1100) and r-plane (1122). 17

Figure 2. 3: Schematic shows the possible radiative and non-radiative recombination in semiconductor materials. a. free electron-hole, b. free exciton, c. donor-hole, d. acceptor-electron, e. donor-acceptor. f. nonradiative recombination via a defect. Adapted from [6] 19

Figure 2. 4 Schematic of the MOVPE reactor adapted from [17]. 22

Figure 2. 5: Schematic of the basic idea of the HVPE reactor adapted from [17] 23

Figure 2. 6: Shows the various point defects that can be formed in a crystal adopted from [27]. 26

Figure 2. 7: a) Edge dislocation as an inserted half plan to the crystal and b) The screw dislocation as the side of the crystal is sheared respect the other side in both images b indicate to burger vector adapted from [28]. 28

Figure 2. 8: The sub-grain boundaries with different coloured arrows represent the different directions of grain orientation. 30

Figure 2. 9: Shows a schematic of the behaviour of TDs in ELOG process adapted from [50]. 32

Figure 2. 10: Illustrates the behaviour of TDs in material grown on nPSS, a is the vertical dislocation above the unetched region, b is the bending dislocation near the voids toward the voids sidewall, and c is the dislocations at the coalescence zone, adapted from [58]. 34

Figure 2. 11: Schematic illustrates the mechanism of TDs reduction by their inclination toward step bunches and interact with other vertical TDs to annihilate each other and forming a dislocation loops. 37

Figure 2. 12: a) Cross-sectional TEM image from GaN sample shows TDs appear as vertical lines, the image is taken from ref. [61] , b) Plan-view TEM image from GaN sample TDs appear as dots with black and white contrast, this image is from ref. [72]. Note both images are from different samples. 39

Figure 2. 13: Shows a CL intensity map from GaN sample from ref.[74].TDs appear as black dots and their density estimated to be ≈ 5×10^{8} cm^{-2}. 40

Figure 2. 14: Shows the X-ray Gaussian peak at 2θ and the width at half maximum FWHM and the maximum intensity. 42

Figure 3. 1: Schematic diagram of the main parts of the scanning electron microscope. 43

Figure 3. 2: The generated signals of the electron- sample interaction. 47

Figure 3. 3: Depth of the generated signals in the scanning electron microscope. 48

Figure 3. 4: The distribution of SE and BSE energy. Regions I and II correspond to BSE energies, and region III to the SE energy. Adapted from reference[85] [82]. 50

Figure 3. 5: Schematic of an E-T detector used to detect SEs 51

Figure 3. 6: The Bloch waves that are used to describe the behavior of the electron beam in respect to the lattice atoms. Wave-I has a maximum intensity in the atom plane while wave-II has a maximum intensity in between the plane of the atoms. 53

Figure 3. 7:The relationship between the incident beam angle and the atomic site as it related to the generation of BSE. Blue arrows indicate the condition where the incident beam is lined up with the

crystal lattice, the orange arrow illustrates the case when the incident beam angle changes with respect to the lattice. The green arrow indicates the effect of a change of positions of atoms in the crystal with respect to the perfect lattice as might be produced by a defect. ... 54

Figure 3. 8: a) The variation of the incident beam with respect to the crystal planes b) The backscattered intensity difference as the incident beam angle θ either greater or smaller to the Bragg angle $\theta_{B.}$ figures adapted from Joy et al. [99] ... 56

Figure 3. 9: ECPs from ELOG GaN demonstrate overlapping bands. This image was acquired at a tilt of 47° and an accelerating voltage of 30 keV ... 56

Figure 3. 10: schematic of the ECCI experiment geometry a) is the forescattered geometry, b) is the backscattered geometry. ... 58

Figure 3. 11: ECCI micrograph from AlGaN thin film sample which shows various information from the crystal (grains, atomic steps, and threading dislocations). Threading dislocations (TD)s appear as black-white contrast. The image was acquired at an accelerating voltage of 30 keV and at a tilt 50° in the forescattered geometry. ... 58

Figure 3. 12: ECCI micrograph at diffraction condition where the edge have the weaker contrast in contrary to the screw component dislocations. The yellow circles are the edge dislocation where the pink circles are related to the screw component dislocations. The image acquired from the ELOG GaN sample from chapter 4. ... 60

Figure 3. 13: Illustrating the standard ECCI method that is used to classify TDs, a) shows the first diffraction condition where the arrows in the bottom image indicate the black-white contrast direction (yellow arrows for edge dislocation, green arrows for screw component dislocations) b) shows the second diffraction condition from the same area where the bottom image is the same image including the arrows that indicate the black-white contrast direction (yellow= edge, green= screw component dislocations). The dislocation images are extracted from a larger image acquired from AlN thin film sample (sample A in chapter 6). ... 61

Figure 3. 14: Schematic of the EBSD setup ... 66

Figure 3. 15: Schematic of an AFM setup adapted from [123]. ... 68

Figure 3. 16: A plot of the forces between the tip and the sample as a distance-dependent interaction adapted from Maghsoudy-Louyeh et al. [123] ... 69

Figure 3. 17: a) Demonstrating the method used for TDs identification in an AFM image (the red circle and inserted magnified image in the red box show a c/(a+c)-type dislocation terminating a step, the green circle and inserted magnified image green box is a-type dislocations located on the step. c/(a+c)-type dislocation (red box) is larger in size comparing to a-type dislocations (green box). b) Histograms from AFM measurements of TD pits depth and step edge terminations, the blue bar is a-type dislocations where the orange one is for c/(a+c)-type dislocation. This data is from ELOG GaN sample which is studied in chapter 4. ... 72

Figure 4. 1: a) Schematic diagram illustrating the growth stages of ELOG, the wing and seed regions are shown, b) Schematic diagram of surface of ELOG showing the direction of the stripes relative to the [1100] and [1120] directions. ... 75

Figure 4. 2: Large AFM image showing a number of wing and seed regions. The approximate location of the seed and wing regions are indicated and have an equal width of 5 µm. ... 77

Figure 4. 3: Large ECCI micrograph showing a number of wing and seed regions. The approximate location of the seed and wing regions are indicated and have an equal width of 5 µm. Red box in the right wing include array of TD that align up at the coalescence line. ... 78

Figure 4. 4: Enlarged ECCI micrograph of the coalescence line at the middle of the wing region the green arrows indicate to the array of dislocations that set at the boundary. The inserted simulated dislocation image is from Picard et al [102]. ... 79

Figure 4. 5: a) ECCI micrograph demonstrates the deviation in the grayscale across large area of the sample (parallel of dark and bright stripes) b) the first derivative of the intensity profile across the ECCI micrograph (notice it is overlapping). 80

Figure 4. 6: The correlated ECCI and AFM images from a seed region a) AFM image b) ECCI micrograph c) ECCI micrograph with coloured circles representing the TDs type d) ECCI micrograph showing the possible black-white contrast direction of pure edge e) distribution of dislocations determined from AFM overlaid with identification of dislocations in seed region. The wing and window stripes of the ELOG sample are readily seen. 82

Figure 4. 7: Correlated ECCI and AFM from a wing region a) AFM image b) ECCI micrograph at first diffraction condition c) ECCI under second diffraction condition, the <1120>and <1100> directions are shown, d) ECCI micrograph with colored circles representing the TDs types as described by the key e) Distribution of dislocations determined from a larger AFM image overlaid with the identification of dislocations in wing region. 83

Figure 4. 8: The behaviour of inclined a-type and (a+c)-type dislocations under different diffraction conditions with **g** vectors of approximately a) (1120), b) (1010) and c) (2110) d) ECCI micrograph from whole coalescence region showing all dislocations highlighted in a, b and c. In addition, the colour key of ECCI micrographs and some important hexagonal direction are demonstrating. 87

Figure 5. 1: The variable SEM parts, including three different regions in pressure P0, P1, and P2 besides series of PLAs (PLA1 and PLA2). 93

Figure 5. 2: The gaseous secondary detection mechanism, in the case of using the off-axis detector. Generated SEs from sample ionize the imaging gas molecules. Positive ions move to land on the sample surface and the amplification process of SEs continue and attracted by the positive bias detector. 96

Figure 5. 3: Shows that a) the on-axis GSED where the beam-gas path length (blue arrow) is equivalent to the sample-detectoe distance (green arrow), b) the off-axis GSED where the beam-gas path length (blue arrow) is not is not equivalent to the sample-detectoe distance (green arrow). 98

Figure 5. 4: ECC micrographs acquired at tilt 64.6° of AlN thin film from a) the large field detector LFD b) the forescattered solid-state detector that located under the EBSD detector. The accelerating voltage is 30 keV for both images, and the gas pressure is 0.6 mbar. 100

Figure 5. 5: Shows ECP that acquired using off-axis GSED, and the red circle is the pattern center. The ***g*** vector is (11-20) 101

Figure 5. 6: Shows the ECC micrographs of AlN thin film not from the same area obtained used the on-axis detector (the ring) located under the pole piece; the image acquired a) at tilt 0°, the dotted circle shows a cluster of TDs with the separation distance ≈ 30 nm. b) at tilt 65°. The accelerating voltage of 30 keV, gas pressure of 1 mbar. 102

Figure 5. 7: Shows the impact of changing the detector bias by changing the contrast setting of the gaseous secondary electron detector to (a) 100 %, (b) 75%, (c) 50 %, and (d) 25 %. The signal strength decreases as the bias voltage is decreased. All four ECCI micrographs are acquired with the same beam current and an acceleration voltage of 30 keV, dwell time of 100 µs, and a sample tilt of 64°. 104

Figure 5. 8: Shows the plots of the magnitude of the sample current (nA) as a function of the various accelerating voltages (keV) and the detector bias (%) for fixed gas pressure of 0.5 mbar and spot size of 6. 105

Figure 5. 9: ECCI micrographs of AlN thin film acquired at the same beam current and an acceleration voltage of 30 keV, of tilt of 52°, dwell time of 100µs, and of gas pressures (a) 0.3 mbar, (b) 0.5 mbar and (c) 0.8 mbar. The inset image in (a) shows two dislocations that can be resolved at a gas pressure of 0.3 mbar. However, on increasing the gas pressure to 0.8 mbar (inset in image c), the individual dislocations are no longer resolved. 106

Figure 5. 10: The impact of gas pressure in VP-SEM on the beam current. It significantly increased as the gas pressure increased. at 0.5 mbar, 0.7 mbar, and at 1 mbar for different beam accelerating voltage (5, 10, 20, 30 keV) for spot size of 6. 107

Figure 5. 11 ECCI micrographs of AlN thin film acquired at the same beam current and an acceleration voltage of 30 keV, tilt 52°, 11.4 mm working distance and at various dwell times of (a) 1 µs, (b) 10 µs, (c) 100 µs and (d) 1000 µs. The dark and bright horizontal lines observed when the scan time is long (c and d) are due to fluctuations in the gas pressure. (e-f) show the images after FFT band-pass filtering to remove the horizontal lines. All images were taken with an image resolution of 1024 × 884. 108

Figure 5. 12: ECCI micrographs of AlN thin film acquired at the same beam current and an acceleration voltage of 30 keV, of tilt of 0°, dwell time of 100 µs and various of working distance between the sample and the pole piece to (a) 6 mm, (b) 8 mm, (c) 11 mm and (d) 14 mm. 109

Figure 5. 13: Shows the plots of the magnitude of the sample current (nA) as a function of the various accelerating voltages (keV) and the spot size for fixed gas pressure, at working distance = 13.8 mm and 10.2mm and the information obtained under the gas pressure of 0.5 mbar and spot size of 6. The influence of increasing working distance, as well as the beam-gas path length increases, the current increased as shown from graphs. 110

Figure 5. 14: ECCI micrographs of AlN thin film acquired at the same beam current and an acceleration voltage of 30 keV, dwell time of 100 µs and sample tilt at (a) 0° tilt, ideally used in the backscatter geometry and (b) 70° tilt, often used in the forescatter geometry. 111

Figure 6. 1: a) Shows the process of nPSS fabrication (original from[63]), b) shows the SE image of nanopillars sapphire, c) scheme of the epitaxial growth of AlN on nPSS. b and c provided from the University of Bath and FBH. 116

Figure 6. 2: Shows ECCI micrographs of sample A and B to illustrate the different surface morphologies, a) ECCI micrograph of sample A reveals small step bunches (indicated by yellow arrows), hillocks (inside the pink box), and sub-grains, b) ECCI micrograph of sample B demonstrates a higher density of step bunches compared to sample A. All images are acquired in the variable pressure SEM using off-axis GSED and under a beam of energy 25 keV, a gas pressure of 0.5 mbar and tilt of ≈50° 119

Figure 6. 3: Show ≈6 × 6 µm² ECCI micrographs of the sample A and B, a) high magnification image of the sample A that shows a closer look at the TDs (dots with black-white contrast) and sub-grains, b) high magnification image of the sample B that show TDs, sub-grains and step bunches. Both images were acquired in the variable pressure SEM using off-axis GSED and under a beam of energy 25 keV, a gas pressure of 0.5 mbar and dwell time 100µs, and tilt ≈ 50°. The yellow rectangles highlight TDs that align with sub-grain boundaries. 121

Figure 6. 4: Demonstrating the selective defect etching method image. The image was obtained from sample B, where the yellow rectangle surrounds the dislocations that align with the step bunch...... 121

Figure 6. 5:Illustrates the identification of TDs by a selective defect etching method. The right image is marked to indicate the types of dislocations. Yellow small circles indicate edge dislocations while the big green circles indicate screw component dislocations. This image was acquired from sample B. 123

Figure 6. 6:Shows 10×10 µm² ECCI micrographs of the samples C, D and E a) sample C exhibits continuous step bunches across the sample b) sample D exhibits small step bunches covering the sample surface c) sample E has a lower density of step bunches in comparison to sample C and D. All images were acquired in the variable pressure SEM using off-axis GSED and under a beam of energy 25 keV, a gas pressure of 0.5 mbar and dwell time 100µs, and tilt ≈ 50°. 126

Figure 6. 7: Shows ≈6 × 6 µm² ECCI micrographs of the samples C, D and E a) high magnification image of sample C that shows a closer look at the TDs (dots with black-white contrast), sub-grains, atomic steps and step bunches b) high magnification image of sample D that show TDs, atomic steps and sub-grains. c) high magnification image of the sample D that show TDs, sub-grains and atomic steps. All images acquired in the variable pressure SEM using off-axis GSED and under a beam of

energy 25 keV, a gas pressure of 0.5 mbar and dwell time 100µs, and tilt ≈ 50°. The yellow rectangles highlight TDs that align with sub-grain boundaries. 126

Figure 6. 8: ECCI micrograph from sample C that shows the spiral growth in this sample, the yellow box surrounds the spiral. 127

Figure 6. 9: The grain reference orientation deviation (GROD) maps with respect to the sample normal (Z-axis) which is the c-axis/[0001] direction. That is GROD-Z maps obtained from a) sample A, b) sample B and c) sample D. The colours indicate rotations of the opposite direction. These maps were extracted from EBSD data using MTEX software. 129

Figure 6. 10: Shows a) an experimental EBSP b) ECCI micrograph from sample B exhibiting step bunches and showing that they lie along the [1120] direction. c) A dynamically simulated EBSP. d) indexed EBSP highlighting the Kikuchi bands for the (1010), (1120) planes and [1120] direction.. 130

Figure 6. 11: Grain reference orientation deviation (GROD) maps for; a) sample A, b) sample B and c) sample D. d) GROD angle distribution for sample A, B, and D. 131

Figure 6. 12: Illustrates coincident EBSD and ECCI micrographs acquired simultaneously under the same diffraction condition from sample D a) ECCI micrograph with deviation in greyscale related to the deviation in sub-grain orientation, b) the ECCI micrograph with the reversed contrast, c) directions (derived from EBSP) d) GROD-X map that shows the out-of-plane rotation around the *x*-axis (approximately in an *a*-direction), e) GROD-Y map that shows the out-of-plane rotation around the *y*-axis (approximately in an *m*-direction), f) GROD-Z map that shows the in-plane rotation around z-axis (c-direction). In maps d to f, red and blue indicate opposite directions of rotation g) GROD-axis map, the colours (see colour key) indicate the rotation axis, where the black and white regions are those exhibiting a purely in-plane rotation, note the correlation with f. h) colour key for g). 133

Figure 6. 13: a) The experimental EBSP, b) BSE signal from the bottom area of EBSP in a (surrounded by the dashed yellow box) diffraction contrast dominates revealing dislocations. Images here are exactly from the same area that the ECCI micrograph and EBSD map have acquired in figure 6.12.. 134

List of Tables

Table 2. 1: The properties of GaN, AlN and the foreign substrates utilized in the growth of III-nitride devices. [20, 21] 24

Table 2. 2:Shows the comparison between the ELOG and nPSS on GaN.[47] [56] [53] 35

Table 3. 1: Summarizing the information that is provided by EBSD and brief descriptions 64

Table 4. 1: Show the comparison between AFM and ECCI from seed and wing regions. 85

Table 4. 2: Summary of the calculated visibility criterion in different diffraction conditions and the experimental observation through ECCI micrographs in figure 4.8 for *a*-type and mixed ((*a*+*c*)-type) dislocations... 88

Table 6. 1: The description of the samples studied in this chapter. 117

Table 6. 2: Shows the result summary of all three samples. 136

References

1. World Healt Organization. *Drinking-water*. 2019; Available from: https://www.who.int/news-room/fact-sheets/detail/drinking-water.
2. World Health Organazation. *Save Lives - clean your hands*. 2020; Available from: https://www.who.int/campaigns/save-lives-clean-your-hands.
3. Kneissl, M., T.-Y. Seong, J. Han, and H. Amano, *The emergence and prospects of deep-ultraviolet light-emitting diode technologies.* Nature Photonics, 2019. **13**(4): p. 233-244.
4. Chang, H.-M., W.-C. Lai, W.-S. Chen, and S.-J. Chang, *GaN-based ultraviolet light-emitting diodes with AlN/GaN/InGaN multiple quantum wells.* Optics Express, 2015. **23**(7): p. A337-A345.
5. Ferreyra, R.A., C. Zhu, A. Teke, and H. Morkoç, *Group III Nitrides*, in *Springer Handbook of Electronic and Photonic Materials*, S. Kasap and P. Capper, Editors. 2017, Springer International Publishing.
6. Schubert, E.F., *Light-Emitting Diodes*. 2 ed. 2006, Cambridge: Cambridge University Press.
7. Takahashi, K., A. Yoshikawa, and A. Sandhu, *Wide Bandgap Semiconductors [internet resource] : Fundamental Properties and Modern Photonic and Electronic Devices*. 1st ed. 2007.. ed. 2007: Berlin, Heidelberg : Springer Berlin Heidelberg.
8. Zhou, C., A. Ghods, V. Saravade, P. Patel, K. Yunghans, C. Ferguson, Y. Feng, B. Kucukgok, N. Lu, and I. Ferguson, *Review—The Current and Emerging Applications of the III-Nitrides.* ECS Journal of Solid State Science and Technology, 2017. **6**: p. Q149-Q156.
9. Acharya, A., *Group III – Nitride Semiconductors: Preeminent Materials for Modern Electronic and Optoelectronic Applications.* Himalayan Physics, 2015. **5**: p. 22.
10. Acharya, A.R., *Group III – Nitride Semiconductors: Preeminent Materials for Modern Electronic and Optoelectronic Applications.* The Himalayan Physics, 2014. **5**: p. 5.
11. Cosendey, G., *(In,Al)N-based blue microcavity lasers.* 2013.
12. Kumar, A.s., *Solid-State Lighting:Technologies and Global Markets.* BCC Research Report Overview, 2019.
13. Ferreyra, R.A., C. Zhu, A. Teke, and H. Morkoç, *Group III Nitrides*, in *Springer Handbook of Electronic and Photonic Materials*, S. Kasap and P. Capper, Editors. 2017, Springer International Publishing: Cham. p. 1-1.
14. Hemmingsson, C., B. Monemar, Y. Kumagai, and A. Koukitu, *Growth of III-Nitrides with Halide Vapor Phase Epitaxy (HVPE)*, in *Springer Handbook of Crystal Growth*, G. Dhanaraj, et al., Editors. 2010, Springer Berlin Heidelberg: Berlin, Heidelberg. p. 869-896.
15. Ryou, J.-H. and W. Lee, *GaN on sapphire substrates for visible light-emitting diodes*, in *Nitride Semiconductor Light-Emitting Diodes (LEDs)*. 2018. p. 43-78.
16. Pohl, U.W., *Epitaxy Of Semiconductors.* Springer, 2013.
17. Nasser N.M, Y.Z.z., Li Jiawei and Xu Ya bou *GaN Hetetoepitaxial Growth Techniques.* Journal of Microwaves and Optoelectronics, 2001. **Vol. 2**.
18. Collazo, R. and N. Dietz, *CHAPTER 8 The Group III-Nitride Material Class: from Preparation to Perspectives in Photoelectrocatalysis*, in *Photoelectrochemical Water*

Splitting: Materials, Processes and Architectures. 2013, The Royal Society of Chemistry. p. 193-222.

19. Paskova, T., D.A. Hanser, and K.R. Evans, *GaN Substrates for III-Nitride Devices.* Proceedings of the IEEE, 2010. **98**(7): p. 1324-1338.
20. Akiyama, T., *Fundamental Properties of III-Nitride Compounds.* 2018. **269**: p. 35-53.
21. Yam, F.K., L. Low, S. Oh, and Z. Hassan, *Gallium Nitride: An Overview of Structural Defects*. 2011.
22. Strite, S., *THE PREPARATION AND PROPERTIES OF VAPOR-DEPOSITED SINGLE-CRYSTAL-LINE GaN.* Journal of Vacuum Science & Technology B: Microelectronics and Nanometer Structures, 1992. **10**(4).
23. Amano, H., N. Sawaki, I. Akasaki, and Y. Toyoda, *Metalorganic vapor phase epitaxial growth of a high quality GaN film using an AlN buffer layer.* Applied Physics Letters, 1986. **48**(5): p. 353-355.
24. Nakamura, S., *GaN Growth Using GaN Buffer Layer.* Japanese Journal of Applied Physics, 1991. **Jpn. J. Appl. Phys. 30 L1705**.
25. Li, H., T.C. Sadler, and P.J. Parbrook, *AlN heteroepitaxy on sapphire by metalorganic vapour phase epitaxy using low temperature nucleation layers.* Journal of Crystal Growth, 2013. **383**: p. 72-78.
26. Paskov, P.P. and B. Monemar, *2 - Point defects in group-III nitrides*, in *Defects in Advanced Electronic Materials and Novel Low Dimensional Structures*, J. Stehr, I. Buyanova, and W. Chen, Editors. 2018, Woodhead Publishing. p. 27-61.
27. Smallman, R.E. and A.H.W. Ngan, *Chapter 6 - Point Defect Behaviour*, in *Modern Physical Metallurgy (Eighth Edition)*, R.E. Smallman and A.H.W. Ngan, Editors. 2014, Butterworth-Heinemann: Oxford. p. 251-285.
28. Hong, S.K. and H.K. Cho, *Structural Defects in GaN and ZnO*, in *Oxide and Nitride Semiconductors: Processing, Properties, and Applications*, T. Yao and S.-K. Hong, Editors. 2009, Springer Berlin Heidelberg: Berlin, Heidelberg. p. 261-310.
29. Ruvimov, S., Z. Liliental-Weber, T. Suski, J.W.A. III, J. Washburn, J. Krueger, C. Kisielowski, E.R. Weber, H. Amano, and I. Akasaki, *Effect of Si doping on the dislocation structure of GaN grown on the A-face of sapphire.* Applied Physics Letters, 1996. **69**(7): p. 990-992.
30. Neily, S., S. Dhouibi, and R. Bonnet, *Threading Dislocations Piercing the Free Surface of an Anisotropic Hexagonal Crystal: Review of Theoretical Approaches.* Advances in Condensed Matter Physics, 2018. **2018**: p. 3038795.
31. Bennett, S., *Dislocations and their reduction in GaN.* Materials Science and Technology, 2010. **26**: p. 1017-1028.
32. Kwon, Y.B., J. Je, P. Ruterana, and G. Nouet, *On the origin of a-type threading dislocations in GaN layers.* Journal of Vacuum Science & Technology A - J VAC SCI TECHNOL A, 2005. **23**.
33. McMahon, W.E., M. Vaisman, J.D. Zimmerman, A.C. Tamboli, and E.L. Warren, *Perspective: Fundamentals of coalescence-related dislocations, applied to selective-area growth and other epitaxial films.* APL Materials, 2018. **6**(12): p. 120903.
34. Moram, M.A., C.S. Ghedia, D.V.S. Rao, J.S. Barnard, Y. Zhang, M.J. Kappers, and C.J. Humphreys, *On the origin of threading dislocations in GaN films.* Journal of Applied Physics, 2009. **106**(7): p. 073513.
35. Dadgar, A., R. Ravash, P. Veit, G. Schmidt, M. Müller, A. Dempewolf, F. Bertram, M. Wieneke, J. Christen, and A. Krost, *Eliminating stacking faults in semi-polar GaN by AlN interlayers.* Applied Physics Letters, 2011. **99**(2): p. 021905.
36. Hull, D., *Introduction to dislocations*. 5th ed.. ed, ed. D.J. Bacon. 2011: Oxford England Boston : Butterworth-Heinemann.

37. Tochigi, E., A. Nakamura, N. Shibata, and Y. Ikuhara, *Dislocation Structures in Low-Angle Grain Boundaries of α-Al2O3.* Crystals, 2018. **8**: p. 133.
38. Manasreh, O.O. and M.O. Manasreh, *III-Nitride Semiconductors: Electrical, Structural and Defects Properties*. 2000, Oxford, NETHERLANDS, THE: Elsevier Science & Technology.
39. Liliental-Weber, Z., *TEM studies of GaN layers grown in non-polar direction: Laterally overgrown and pendeo-epitaxial layers.* Journal of Crystal Growth, 2008. **310**(17): p. 4011-4015.
40. Banal, R., M. Imura, and Y. Koide, *Formation Mechanism and Elimination of Small-Angle Grain Boundary in AlN Grown on (0001) Sapphire Substrate*. 2017. p. 43-58.
41. Murr, L.E., *Volume Defects: 3D Imperfections in Crystals*, in *Handbook of Materials Structures, Properties, Processing and Performance*, L.E. Murr, Editor. 2015, Springer International Publishing: Cham. p. 313-324.
42. Lee, K. and K. Auh, *Dislocation Density of GaN Grown by Hydride Vapor Phase Epitaxy.* MRS Internet journal of nitride semiconductor research, 2001. **6**.
43. Hiramatsu, K., T. Detchprohm, and I. Akasaki, *Relaxation Mechanism of Thermal Stresses in the Heterostructure of GaN Grown on Sapphire by Vapor Phase Epitaxy.* Japanese Journal of Applied Physics, 1993. **32**(Part 1, No. 4): p. 1528-1533.
44. Tanikawa, T., K. Ohnishi, M. Kanoh, T. Mukai, and T. Matsuoka, *Three-dimensional imaging of threading dislocations in GaN crystals using two-photon excitation photoluminescence.* Applied Physics Express, 2018. **11**(3): p. 031004.
45. Hiramatsu, K., *Epitaxial lateral overgrowth techniques used in group III nitride epitaxy.* Journal of Physics: Condensed Matter, 2001. **13**(32): p. 6961-6975.
46. Nakamura, S., *The blue laser diode : GaN based light emitters and lasers*, ed. G. Fasol. 1997, Berlin: Springer.
47. Gibart, P., *Metal organic vapour phase epitaxy of GaN and lateral overgrowth.* Reports on Progress in Physics, 2004. **67**(5): p. 667-715.
48. Vennéguès, P., B. Beaumont, V. Bousquet, M. Vaille, and P. Gibart, *Reduction mechanisms for defect densities in GaN using one- or two-step epitaxial lateral overgrowth methods.* Journal of Applied Physics, 2000. **87**(9): p. 4175-4181.
49. Hiramatsu, K., K. Nishiyama, A. Motogaito, H. Miyake, Y. Iyechika , and T. Maeda, *Recent Progress in Selective Area Growth and Epitaxial Lateral Overgrowth of III-Nitrides: Effects of Reactor Pressure in MOVPE Growth.* phys. stat. sol. , 1999. **176**: p. 535.
50. Bennett, S., D. Holec, M. Kappers, C. Humphreys, and R. Oliver, *Imaging dislocations in gallium nitride across broad areas using atomic force microscopy.* The Review of scientific instruments, 2010. **81**: p. 063701.
51. Ashby, C.I.H., C.C. Mitchell, J. Han, N.A. Missert, P.P. Provencio, D.M. Follstaedt, G.M. Peake, and L. Griego, *Low-dislocation-density GaN from a single growth on a textured substrate.* Applied Physics Letters, 2000. **77**(20): p. 3233-3235.
52. Chen, Z., J. Li, Y. Chen, C. Li, J. Zhan, T.J. Yu, X. Kang, F. Jiao, S.F. Li, G. Zhang, B. Shen, and Y.F. Chen, *Study on GaN nucleation and coalescence in the initial growth stages on nanoscale patterned sapphire substrates by MOCVD.* CrystEngComm, 2018. **20**.
53. Gao, H., F. Yan, Y. Zhang, J. Li, Y. Zeng, and G. Wang, *Fabrication of nano-patterned sapphire substrates and their application to the improvement of the performance of GaN-based LEDs.* Journal of Physics D: Applied Physics, 2008. **41**(11): p. 115106.

54. Su, Y.K., J.J. Chen, C.L. Lin, S.M. Chen, W.L. Li, and C.C. Kao, *Pattern-size dependence of characteristics of nitride-based LEDs grown on patterned sapphire substrates.* Journal of Crystal Growth, 2009. **311**(10): p. 2973-2976.
55. Gao, H., F. Yan, Y. Zhang, J. Li, Y. Zeng, and G. Wang, *Enhancement of the light output power of InGaN/GaN light-emitting diodes grown on pyramidal patterned sapphire substrates in the micro- and nanoscale.* Journal of Applied Physics, 2008. **103**: p. 014314-014314.
56. Seong, T.-Y., J. Han, H. Amano, and H. Morkoç, *III-nitride based light emitting diodes and applications / [internet resource]*. Second edition.. ed. 2017: Singapore : Springer.
57. Coulon, P.-M., B. Damilano, B. Alloing, P. Chausse, S. Walde, J. Enslin, R. Armstrong, S. Vézian, S. Hagedorn, T. Wernicke, J. Massies, J. Zúñiga-Pérez, M. Weyers, M. Kneissl, and P.A. Shields, *Displacement Talbot lithography for nano-engineering of III-nitride materials.* Microsystems & Nanoengineering, 2019. **5**(1): p. 52.
58. Zhang, L., F. Xu, J. Wang, C. He, W. Guo, M. Wang, B. Sheng, L. Lu, Z. Qin, X. Wang, and B. Shen, *High-quality AlN epitaxy on nano-patterned sapphire substrates prepared by nano-imprint lithography.* Scientific Reports, 2016. **6**(1): p. 35934.
59. Shen, X.-Q., H. Matsuhata, T. Ide, and M. Shimizu, *Direct measurement of lateral macrostep velocity on an AlN vicinal surface by transmission electron microscopy.* Journal of Applied Physics, 2012. **111**.
60. Huang, X.R., J. Bai, M. Dudley, R.D. Dupuis, and U. Chowdhury, *Epitaxial tilting of GaN grown on vicinal surfaces of sapphire.* Applied Physics Letters, 2005. **86**(21): p. 211916.
61. Shen, X.-Q., H. Matsuhata, and H. Okumura, *Reduction of the threading dislocation density in GaN films grown on vicinal sapphire (0001) substrates.* Applied Physics Letters, 2005. **86**: p. 021912-021912.
62. Holmes, J., S. Conroy, V. Zubialevich, H. Li, N. Petkov, and P. Parbrook, *Epitaxial Lateral Overgrowth of AlN on Self-Assembled Patterned Nanorods.* J. Mater. Chem. C, 2014. **3**.
63. Walde, S., S. Hagedorn, P.M. Coulon, A. Mogilatenko, C. Netzel, J. Weinrich, N. Susilo, E. Ziffer, L. Matiwe, C. Hartmann, G. Kusch, A. Alasmari, G. Naresh-Kumar, C. Trager-Cowan, T. Wernicke, T. Straubinger, M. Bickermann, R.W. Martin, P.A. Shields, M. Kneissl, and M. Weyers, *AlN overgrowth of nano-pillar-patterned sapphire with different offcut angle by metalorganic vapor phase epitaxy.* Journal of Crystal Growth, 2020. **531**.
64. Enslin, J., A. Knauer, A. Mogilatenko, F. Mehnke, M. Martens, C. Kuhn, T. Wernicke, M. Weyers, and M. Kneissl, *Determination of Sapphire Off-Cut and Its Influence on the Morphology and Local Defect Distribution in Epitaxially Laterally Overgrown AlN for Optically Pumped UVC Lasers.* physica status solidi (a), 2019. **216**(24): p. 1900682.
65. Hagedorn, S., A. Knauer, A. Mogilatenko, E. Richter, and M. Weyers, *AlN growth on nano-patterned sapphire: A route for cost efficient pseudo substrates for deep UV LEDs.* physica status solidi (a), 2016. **213**(12): p. 3178-3185.
66. Lewerenz, H.-J., *Photoelectrochemical water splitting : materials, processes and architectures*. 2013, Cambridge: RSC Publishing.
67. Shen, X.-Q. and H. Okumura, *Surface step morphologies of GaN films grown on vicinal sapphire (0 0 0 1) substrates by rf-MBE.* Journal of Crystal Growth - J CRYST GROWTH, 2007. **300**: p. 75-78.

68. Bryan, I., Z. Bryan, S. Mita, A. Rice, J. Tweedie, R. Collazo, and Z. Sitar, *Surface kinetics in AlN growth: A universal model for the control of surface morphology in III-nitrides.* Journal of Crystal Growth, 2016. **438**: p. 81-89.
69. Someya, T., K. Hoshino, and Y. Arakawa, *Misorientation-angle dependence of GaN layers grown on a-plane sapphire substrates by metalorganic chemical vapor deposition.* Applied Physics Letters, 2001. **79**(13): p. 1992-1994.
70. Kueller, V., A. Knauer, U. Zeimer, M. Kneissl, and M. Weyers, *Controlled coalescence of MOVPE grown AlN during lateral overgrowth.* Journal of Crystal Growth, 2013. **368**: p. 83-86.
71. Kusch, G., H. Li, P.R. Edwards, J. Bruckbauer, T.C. Sadler, P.J. Parbrook, and R.W. Martin, *Influence of substrate miscut angle on surface morphology and luminescence properties of AlGaN.* Applied Physics Letters, 2014. **104**(9): p. 092114.
72. Follstaedt, D., N.A. Missert, D. Koleske, C. Mitchell, and K. Cross, *Plan-view image contrast of dislocations in GaN.* Applied Physics Letters, 2003. **83**: p. 4797-4799.
73. Bruckbauer, J., P.R. Edwards, T. Wang, and R.W. Martin, *High resolution cathodoluminescence hyperspectral imaging of surface features in InGaN/GaN multiple quantum well structures.* Applied Physics Letters, 2011. **98**(14): p. 141908.
74. Naresh-Kumar, G., J. Bruckbauer, P.R. Edwards, S. Kraeusel, B. Hourahine, R.W. Martin, M.J. Kappers, M.A. Moram, S. Lovelock, R.A. Oliver, C.J. Humphreys, and C. Trager-Cowan, *Coincident electron channeling and cathodoluminescence studies of threading dislocations in GaN.* Microsc Microanal, 2014. **20**(1): p. 55-60.
75. Edwards, P.R. and R.W. Martin, *Cathodoluminescence nano-characterization of semiconductors.* 2011.
76. Trager-Cowan, C., A. Alasmari, W. Avis, J. Bruckbauer, P.R. Edwards, B. Hourahine, S. Kraeusel, G. Kusch, R. Johnston, G. Naresh-Kumar, R.W. Martin, M. Nouf-Allehiani, E. Pascal, L. Spasevski, D. Thomson, S. Vespucci, P.J. Parbrook, M.D. Smith, J. Enslin, F. Mehnke, M. Kneissl, C. Kuhn, T. Wernicke, S. Hagedorn, A. Knauer, V. Kueller, S. Walde, M. Weyers, P.M. Coulon, P.A. Shields, Y. Zhang, L. Jiu, Y. Gong, R.M. Smith, T. Wang, and A. Winkelmann, *Scanning electron microscopy as a flexible technique for investigating the properties of UV-emitting nitride semiconductor thin films.* Photonics Research, 2019. **7**(11): p. B73-B82.
77. Nath, D., F. Singh, and R. Das, *X-ray diffraction analysis by Williamson-Hall, Halder-Wagner and size-strain plot methods of CdSe nanoparticles- a comparative study.* Materials Chemistry and Physics, 2020. **239**: p. 122021.
78. Bishnoi, A., S. Kumar, and N. Joshi, *Wide-Angle X-ray Diffraction (WXRD)*. 2017. p. 313-337.
79. Kopp, V.S., V.M. Kaganer, M.V. Baidakova, W.V. Lundin, A.E. Nikolaev, E.V. Verkhovtceva, M.A. Yagovkina, and N. Cherkashin, *X-ray determination of threading dislocation densities in GaN/Al2O3(0001) films grown by metalorganic vapor phase epitaxy.* Journal of Applied Physics, 2014. **115**(7): p. 073507.
80. Hawkes, P.W. and J.C.H. Spence, *Springer Handbook of Microscopy [internet resource]*. 1st ed. 2019.. ed. 2019: Cham : Springer International Publishing.
81. Thompson, J.M.T. and D.J. Stokes, *Recent advances in electron imaging, image interpretation and applications: environmental scanning electron microscopy.* Philosophical Transactions of the Royal Society of London. Series A: Mathematical, Physical and Engineering Sciences, 2003. **361**(1813): p. 2771-2787.
82. Stokes, D., *Principles and Practice of Variable Pressure/Environmental Scanning Electron Microscopy (VP-ESEM).* Principles and Practice of Variable Pressure/Environmental Scanning Electron Microscopy (VP-ESEM), 2008: p. 1-221.

83. Goldstein, J., D.E. Newbury, J.R. Michael, N.W.M. Ritchie, J.H.J. Scott, and D.C. Joy, *Scanning electron microscopy and x-ray microanalysis / [internet resource]*. Fourth edition.. ed. 2018: New York, NY : Springer.
84. Kyser, D.F., *Monte Carlo Simulation in Analytical Electron Microscopy*, in *Introduction to Analytical Electron Microscopy*, J.J. Hren, J.I. Goldstein, and D.C. Joy, Editors. 1979, Springer US: Boston, MA. p. 199-221.
85. Kriaa, H., A. Guitton, and N. Maloufi, *Fundamental and experimental aspects of diffraction for characterizing dislocations by electron channeling contrast imaging in scanning electron microscope.* Scientific Reports, 2017. **7**(1): p. 9742.
86. Pang, B., I.P. Jones, Y.-L. Chiu, J.C.F. Millett, and G. Whiteman, *Electron channelling contrast imaging of dislocations in a conventional SEM.* Philosophical Magazine, 2017. **97**(5): p. 346-359.
87. Naresh-Kumar, G., D. Thomson, M. Nouf-Allehiani, J. Bruckbauer, P.R. Edwards, B. Hourahine, R.W. Martin, and C. Trager-Cowan, *Electron channelling contrast imaging for III-nitride thin film structures.* Materials Science in Semiconductor Processing, 2016. **47**: p. 44-50.
88. Zaefferer, S. and N.-N. Elhami, *Theory and application of electron channelling contrast imaging under controlled diffraction conditions.* Acta Materialia, 2014. **75**: p. 20-50.
89. Kamaladasa, R.J., W. Jiang, and Y.N. Picard, *Imaging Dislocations in Single-Crystal SrTiO3 Substrates by Electron Channeling.* Journal of Electronic Materials, 2011. **40**(11): p. 2222.
90. Wilkinson, A.J. and P.B. Hirsch, *Electron diffraction based techniques in scanning electron microscopy of bulk materials.* Micron, 1997. **28**(4): p. 279-308.
91. Twigg, M.E., Y.N. Picard, J.D. Caldwell, C.R. Eddy, M.A. Mastro, R.T. Holm, P.G. Neudeck, A.J. Trunek, and J.A. Powell, *Diffraction Contrast of Threading Dislocations in GaN and 4H-SiC Epitaxial Layers Using Electron Channeling Contrast Imaging.* Journal of Electronic Materials, 2010. **39**(6): p. 743-746.
92. Trager-Cowan, C., F. Sweeney, P.W. Trimby, A.P. Day, A. Gholinia, N.H. Schmidt, P.J. Parbrook, A.J. Wilkinson, and I.M. Watson, *Electron backscatter diffraction and electron channeling contrast imaging of tilt and dislocations in nitride thin films.* Physical Review B, 2007. **75**(8).
93. Deitz, J.I., S.D. Carnevale, S.A. Ringel, D.W. McComb, and T.J. Grassman, *Electron Channeling Contrast Imaging for Rapid III-V Heteroepitaxial Characterization.* Journal of visualized experiments : JoVE, 2015(101): p. e52745-e52745.
94. Carnevale, S.D., J.I. Deitz, J.A. Carlin, Y.N. Picard, D.W. McComb, M.D. Graef, S.A. Ringel, and T.J. Grassman, *Applications of Electron Channeling Contrast Imaging for the Rapid Characterization of Extended Defects in III–V/Si Heterostructures.* IEEE Journal of Photovoltaics, 2015. **5**(2): p. 676-682.
95. Ashida, K., T. Aiso, M. Okamoto, H. Seki, M. Kitabatake, and T. Kaneko. *Low energy electron channeling contrast imaging from 4H-SiC surface by SEM and its comparison with CDIC-OM and PL imaging*. in *2016 European Conference on Silicon Carbide & Related Materials (ECSCRM)*. 2016.
96. Picard, Y., M. Twigg, J. Caldwell, C. Eddy, P. Neudeck, A. Trunek, and J. Powell, *Electron channeling contrast imaging of atomic steps and threading dislocations in 4H-SiC.* Applied Physics Letters, 2007. **90**: p. 234101-234101.
97. Gutierrez-Urrutia, I. and D. Raabe, *Dislocation density measurement by electron channeling contrast imaging in a scanning electron microscope.* Scripta Materialia, 2012. **66**(6): p. 343-346.

98. Joy, D.C., D.E. Newbury, and D.L. Davidson, *Electron channeling patterns in the scanning electron microscope.* Journal of Applied Physics, 1982. **53**(8): p. R81-R122.
99. Newbury, D.E., *Advanced scanning electron microscopy and X-ray microanalysis*. 1986, New York: New York : Plenum Press.
100. Joy, D.C. and D.B. Holt, *SEM microcharacterization of semiconductors*. 1989, London: London : Academic Press.
101. Picard, Y.N., M. Liu, J. Lammatao, R. Kamaladasa, and M. De Graef, *Theory of dynamical electron channeling contrast images of near-surface crystal defects.* Ultramicroscopy, 2014. **146**: p. 71-78.
102. Pascal, E., B. Hourahine, G. Naresh-Kumar, K. Mingard, and C. Trager-Cowan, *Dislocation contrast in electron channelling contrast images as projections of strain-like components.* Materials Today: Proceedings, 2018. **5**(6, Part 3): p. 14652-14661.
103. Romanitan, C., R. Gavrila, and M. Danila, *Comparative study of threading dislocations in GaN epitaxial layers by nondestructive methods.* Materials Science in Semiconductor Processing, 2017. **57**: p. 32-38.
104. Zhu, T. and R.A. Oliver, *Unintentional doping in GaN.* Phys Chem Chem Phys, 2012. **14**(27): p. 9558-73.
105. Trager-Cowan, C., A. Alasmari, W. Avis, J. Bruckbauer, P.R. Edwards, G. Ferenczi, B. Hourahine, A. Kotzai, S. Kraeusel, G. Kusch, R.W. Martin, R. McDermott, G. Naresh-Kumar, M. Nouf-Allehiani, E. Pascal, D. Thomson, S. Vespucci, M.D. Smith, P.J. Parbrook, J. Enslin, F. Mehnke, C. Kuhn, T. Wernicke, M. Kneissl, S. Hagedorn, A. Knauer, S. Walde, M. Weyers, P.M. Coulon, P.A. Shields, J. Bai, Y. Gong, L. Jiu, Y. Zhang, R.M. Smith, T. Wang, and A. Winkelmann, *Structural and luminescence imaging and characterisation of semiconductors in the scanning electron microscope.* Semiconductor Science and Technology, 2020. **35**(5): p. 054001.
106. Ledig, J., F. Steib, J. Hartmann, S. Fündling, H.-H. Wehmann, and A. Waag, *Correlative ECCI and CL of single GaN microstructures obtained using ECP by beam rocking on small areas*, in *European Microscopy Congress 2016: Proceedings*. 2016. p. 1043-1044.
107. Gutierrez-Urrutia, I., S. Zaefferer, and D. Raabe, *Coupling of Electron Channeling with EBSD: Toward the Quantitative Characterization of Deformation Structures in the SEM.* JOM, 2013. **65**(9): p. 1229-1236.
108. Tripathi, A. and S. Zaefferer, *On the resolution of EBSD across atomic density and accelerating voltage with a particular focus on the light metal magnesium.* Ultramicroscopy, 2019. **207**: p. 112828.
109. Trager-Cowan, C., F. Sweeney, A.J. Wilkinson, I.M. Watson, P.G. Middleton, K.P. O'Donnell, D. Zubia, S.D. Hersee, S. Einfeldt, and D. Hommel, *Determination of the Structural and Luminescence Properties of Nitrides Using Electron Backscattered Diffraction and Photo- and Cathodoluminescence.* physica status solidi (c), 2003. **n/a**(1): p. 532-536.
110. Schwartz, A., M. Kumar, and B. Adams, *Electron Backscatter Diffraction in Material Science*. 2000.
111. Laigo, J., F. Christien, R. Le Gall, F. Tancret, and J. Furtado, *SEM, EDS, EPMA-WDS and EBSD characterization of carbides in HP type heat resistant alloys.* Materials Characterization, 2008. **59**(11): p. 1580-1586.
112. Lin, H.-P., T.-S. Ng, J.-C. Kuo, Y.-C. Chen, C.-L. Chen, and S.-X. Ding, *EBSD study on crystallographic texture and microstructure development of cold-rolled FePd alloy.* Materials Characterization, 2014. **93**: p. 163-172.

113. Gubicza, J., *Chapter 2 - Characterization Methods of Lattice Defects*, in *Defect Structure and Properties of Nanomaterials (Second Edition)*, J. Gubicza, Editor. 2017, Woodhead Publishing. p. 27-57.
114. Reed, B.W. and C.A. Schuh, *Grain Boundary Networks*, in *Electron Backscatter Diffraction in Materials Science*, A.J. Schwartz, et al., Editors. 2009, Springer US: Boston, MA. p. 201-214.
115. Small, J.A. and J.R. Michael, *Phase identification of individual crystalline particles by electron backscatter diffraction.* Journal of Microscopy, 2001. **201**(1): p. 59-69.
116. El-Dasher, B. and A. Deal, *Application of Electron Backscatter Diffraction to Phase Identification*, in *Electron Backscatter Diffraction in Materials Science*, A.J. Schwartz, et al., Editors. 2009, Springer US: Boston, MA. p. 81-95.
117. Wilkinson, A.J. and T.B. Britton, *Strains, planes, and EBSD in materials science.* Materials Today, 2012. **15**(9): p. 366-376.
118. Vilalta-Clemente, A., G. Naresh-Kumar, M. Nouf-Allehiani, P. Gamarra, M.A. di Forte-Poisson, C. Trager-Cowan, and A.J. Wilkinson, *Cross-correlation based high resolution electron backscatter diffraction and electron channelling contrast imaging for strain mapping and dislocation distributions in InAlN thin films.* Acta Materialia, 2017. **125**: p. 125-135.
119. Britton, T.B. and A.J. Wilkinson, *High resolution electron backscatter diffraction measurements of elastic strain variations in the presence of larger lattice rotations.* Ultramicroscopy, 2012. **114**: p. 82-95.
120. Wallis, D., L.N. Hansen, T.B. Britton, and A.J. Wilkinson, *High-Angular Resolution Electron Backscatter Diffraction as a New Tool for Mapping Lattice Distortion in Geological Minerals.* Journal of Geophysical Research: Solid Earth, 2019. **124**(7): p. 6337-6358.
121. Wells, O.C., *Comparison of different models for the generation of electron backscattering patterns in the scanning electron microscope.* Scanning, 1999. **21**(6): p. 368-371.
122. Maghsoudy-Louyeh, S., M. Kropf, and B.R. Tittmann, *Review of Progress in Atomic Force Microscopy.* The Open Neuroimaging Journal, 2018. **12**(1): p. 86-104.
123. Jalili, N. and K. Laxminarayana, *A review of atomic force microscopy imaging systems: application to molecular metrology and biological sciences.* Mechatronics, 2004. **14**(8): p. 907-945.
124. Liu, S. and Y. Wang, *A Review of the Application of Atomic Force Microscopy (AFM) in Food Science and Technology.* Advances in food and nutrition research, 2011. **62**: p. 201-40.
125. Watkins, S.P., R. Arès, G. Soerensen, W. Zhong, C.A. Tran, J.E. Bryce, and C.R. Bolognesi, *Atomic force microscopy study of morphology and dislocation structure of InAs and GaSb grown on highly mismatched substrates.* Journal of Crystal Growth, 1997. **170**(1): p. 788-793.
126. Bennett, S.E., D. Holec, M.J. Kappers, C.J. Humphreys, and R.A. Oliver, *Imaging dislocations in gallium nitride across broad areas using atomic force microscopy.* Review of Scientific Instruments, 2010. **81**(6): p. 063701.
127. Besendörfer, S., E. Meissner, A. Lesnik, J. Friedrich, A. Dadgar, and T. Erlbacher, *Methodology for the investigation of threading dislocations as a source of vertical leakage in AlGaN/GaN-HEMT heterostructures for power devices.* Journal of Applied Physics, 2019. **125**(9): p. 095704.
128. Tian, Y., L. Zhang, Y. Wu, Y. Shao, Y. Dai, H. Zhang, R. Wei, and X. Hao, *Characterization of dislocations in MOCVD-grown GaN using a high temperature annealing method.* CrystEngComm, 2014. **16**(11).

129. Oliver, R.A., M.J. Kappers, J. Sumner, R. Datta, and C.J. Humphreys, *Highlighting threading dislocations in MOVPE-grown GaN using an in situ treatment with SiH4 and NH3.* Journal of Crystal Growth, 2006. **289**(2): p. 506-514.
130. Wzorek, M., A. Czerwinski, J. Ratajczak, A. Lui, E. Iacob, and J. Katcki, *Depth measurements of etch-pits in GaN with shape reconstruction from SEM images.* J Microsc, 2010. **237**(3): p. 242-5.
131. Manasreh, O.O. and M.O. Manasreh, *III-Nitride Semiconductors : Electrical, Structural and Defects Properties*. 2000, Oxford, NETHERLANDS: Elsevier Science & Technology.
132. GmbH, R.L. *UV Photodiodes* ; Available from: http://www.roithner-laser.com/pd_uv.html.
133. Bennett, S.E., *Dislocations and their reduction in GaN.* Materials Science and Technology, 2010. **26**(9): p. 1017-1028.
134. Shih, H.-Y., M. Shiojiri, C.-H. Chen, S.-F. Yu, C.-T. Ko, J.-R. Yang, R.-M. Lin, and M.-J. Chen, *Ultralow threading dislocation density in GaN epilayer on near-strain-free GaN compliant buffer layer and its applications in hetero-epitaxial LEDs.* Scientific reports, 2015. **5**: p. 13671-13671.
135. Le Boulbar, E.D., J. Priesol, M. Nouf-Allehiani, G. Naresh-Kumar, S. Fox, C. Trager-Cowan, A. Šatka, D.W.E. Allsopp, and P.A. Shields, *Design and fabrication of enhanced lateral growth for dislocation reduction in GaN using nanodashes.* Journal of Crystal Growth, 2017. **466**: p. 30-38.
136. Hiramatsu, K., *Epitaxial lateral overgrowth techniques used in group III nitride epitaxy.* J. Phys.: Condens. Matte, 2001. **13**: p. 6961.
137. Takeya, M., T. Mizuno, T. Sasaki, S. Ikeda, T. Fujimoto, Y. Ohfuji, K. Oikawa, Y. Yabuki, S. Uchida, and M. Ikeda, *Degradation in AlGaInN lasers.* physica status solidi (c), 2003. **0**(7): p. 2292-2295.
138. Smart, J.A., E.M. Chumbes, A.T. Schremer, and J.R. Shealy, *Single step process for epitaxial lateral overgrowth of GaN on SiC and sapphire substrates.* Applied Physics Letters, 1999. **75**(24): p. 3820-3822.
139. Picard, Y.N., M.E. Twigg, J.D. Caldwell, C.R. Eddy, M.A. Mastro, and R.T. Holm, *Resolving the Burgers vector for individual GaN dislocations by electron channeling contrast imaging.* Scripta Materialia, 2009. **61**(8): p. 773-776.
140. O'Hanlon, T., *Development of Multi-Microscopy Techniques for the Characterisation of Nitride Semiconductors*. 2018.
141. Gutierrez-Urrutia, I., S. Zaefferer, and D. Raabe, *Coupling of Electron Channeling with EBSD: Toward the Quantitative Characterization of Deformation Structures in the SEM*. Vol. 65. 2013. 1229-1236.
142. Naresh-Kumar, G., B. Hourahine, P.R. Edwards, A.P. Day, A. Winkelmann, A.J. Wilkinson, P.J. Parbrook, G. England, and C. Trager-Cowan, *Rapid Nondestructive Analysis of Threading Dislocations in Wurtzite Materials Using the Scanning Electron Microscope.* Physical Review Letters, 2012. **108**(13): p. 135503.
143. Datta, R. and C.J. Humphreys, *Mechanisms of bending of threading dislocations in MOVPE-grown GaN on (0001) sapphire.* physica status solidi c, 2006. **3**(6): p. 1750-1753.
144. Oliver, R., S. Bennett, J. Sumner, M. Kappers, and C. Humphreys, *Scanning capacitance microscopy studies of GaN grown by epitaxial layer overgrowth.* Journal of Physics: Conference Series, 2010. **209**.

145. Romanov, A.E. and J.S. Speck, *Stress relaxation in mismatched layers due to threading dislocation inclination.* Applied Physics Letters, 2003. **83**(13): p. 2569-2571.
146. Cantu, P., F. Wu, P. Waltereit, S. Keller, A.E. Romanov, U.K. Mishra, S.P. DenBaars, and J.S. Speck, *Si doping effect on strain reduction in compressively strained Al0.49Ga0.51N thin films.* Applied Physics Letters, 2003. **83**(4): p. 674-676.
147. Follstaedt, D.M., S.R. Lee, A.A. Allerman, and J.A. Floro, *Strain relaxation in AlGaN multilayer structures by inclined dislocations.* Journal of Applied Physics, 2009. **105**(8): p. 083507.
148. Wang, J.F., D.Z. Yao, J. Chen, J.J. Zhu, D.G. Zhao, D.S. Jiang, H. Yang, and J.W. Liang, *Strain evolution in GaN layers grown on high-temperature AlN interlayers.* Applied Physics Letters, 2006. **89**(15): p. 152105.
149. Cantu, P., F. Wu, P. Waltereit, S. Keller, A.E. Romanov, S.P. DenBaars, and J.S. Specka, *Role of inclined threading dislocations in stress relaxation in mismatched layers.* Journal of Applied Physics,, 2005. **97**: p. 103534
150. Wu, Z., K. Nonaka, Y. Kawai, T. Asai, F.A. Ponce, C. Chen, M. Iwaya, S. Kamiyama, H. Amano, and I. Akasaki, *Strain Relaxation Mechanisms in AlGaN Epitaxy on AlN Templates.* Applied Physics Express, 2010. **3**(11): p. 111003.
151. Liliental-Weber, Z. and D. Cherns, *Microstructure of laterally overgrown GaN layers.* Journal of Applied Physics, 2001. **89**(12): p. 7833-7840.
152. Follstaedt, D.M., S.R. Lee, P.P. Provencio, A.A. Allerman, J.A. Floro, and M.H. Crawford, *Relaxation of compressively-strained AlGaN by inclined threading dislocations.* Applied Physics Letters, 2005. **87**(12): p. 121112.
153. Mansour, H., M.A. Crimp, N. Gey, and N. Maloufi, *Accurate electron channeling contrast analysis of a low angle sub-grain boundary.* Scripta Materialia, 2015. **109**: p. 76-79.
154. Gradečak, S., P. Stadelmann, V. Wagner, and M. Ilegems, *Bending of dislocations in GaN duing epitaxial lateral overgrowth.* Applied Physics Letters, 2004. **85**: p. 4648-4650.
155. Kneissl, M., T. Kolbe, C. Chua, V. Kueller, N. Lobo, J. Stellmach, A. Knauer, H. Rodriguez, S. Einfeldt, Z. Yang, N.M. Johnson, and M. Weyers, *Advances in group III-nitride-based deep UV light-emitting diode technology.* Semiconductor Science and Technology, 2010. **26**(1): p. 014036.
156. Ban, K., J.-i. Yamamoto, K. Takeda, K. Ide, M. Iwaya, T. Takeuchi, S. Kamiyama, I. Akasaki, and H. Amano, *Internal Quantum Efficiency of Whole-Composition-Range AlGaN Multiquantum Wells.* Applied Physics Express, 2011. **4**(5): p. 052101.
157. Danilatos, G.D., *An atmospheric scanning electron microscope (ASEM).* Scanning, 1980. **3**(3): p. 215-217.
158. Danilatos, G.D., *Design and construction of an atmospheric or environmental SEM (part 3).* Scanning, 1985. **7**(1): p. 26-42.
159. Newbury, D.E., *Imaging deep holes in structures with gaseous secondary electron detection in the environmental scanning electron microscope.* Scanning, 1996. **18**(7): p. 474-482.
160. Thiel, B.L. and A.M. Donald, *The study of water in heterogeneous media using environmental scanning electron microscopy.* Journal of Molecular Liquids, 1999. **80**(2): p. 207-230.
161. Mohan, A., N. Khanna, J. Hwu, and D.C. Joy, *Secondary electron imaging in the variable pressure scanning electron microscope.* Scanning, 1998. **20**(6): p. 436-441.

162. FARLEY, A.N. and J.S. SHAH, *High-pressure scanning electron microscopy of insulating materials: A new approach.* Journal of Microscopy, 1991. **164**(2): p. 107-126.
163. Danilatos, G., *The examination of fresh or living plant material in an environmental scanning electron microscope.* Journal of Microscopy, 2011. **121**: p. 235-238.
164. Stokes, D., *Investigating Biological Ultrastructure using Environmental Scanning Electron Microscopy (ESEM).* Science, 2006.
165. Danilatos, G.D., *Implications of the figure of merit in environmental SEM.* Micron, 2013. **44**: p. 143-149.
166. Danilatos, G., *Foundations of Environmental Scanning Electron Microscopy.* Advances in Electronics and Electron Physics, 1988. **71**: p. 109-250.
167. Thiel, B., *Variable Pressure Scanning Electron Microscopy*, in *Springer Handbook of Microscopy*, P.W. Hawkes and J.C.H. Spence, Editors. 2019, Springer International Publishing: Cham. p. 2-2.
168. Fletcher, A.L., B.L. Thiel, and A.M. Donald, *Amplification measurements of alternative imaging gases in environmental SEM.* Journal of Physics D: Applied Physics, 1997. **30**(15): p. 2249-2257.
169. Thiel, B.L. and M. Toth, *Secondary electron contrast in low-vacuum∕environmental scanning electron microscopy of dielectrics.* Journal of Applied Physics, 2005. **97**(5): p. 051101.
170. Danilatos, G.D., *Design and construction of an environmental SEM (part 4).* Scanning, 1990. **12**(1): p. 23-27.
171. Danilatos, G.D., *Environmental scanning electron microscopy and microanalysis.* Microchimica Acta, 1994. **114**(1): p. 143-155.
172. Toth, M., B.L. Thiel, and A.M. Donald, *On the role of electron–ion recombination in low vacuum scanning electron microscopy.* Journal of Microscopy, 2002. **205**(1): p. 86-95.
173. Xing, Q., *Information or resolution: Which is required from an SEM to study bulk inorganic materials?* Scanning, 2016. **38**(6): p. 864-879.
174. Hirayama, H., N. Maeda, S. Fujikawa, S. Toyoda, and N. Kamata, *Recent progress and future prospects of AlGaN-based high-efficiency deep-ultraviolet light-emitting diodes.* Japanese Journal of Applied Physics, 2014. **53**: p. 100209.
175. Khan, A., B. Krishnan, and T. Katona, *Ultraviolet Light-Emitting Diodes Based on Group Three Nitrides.* Nature Photonics, 2008. **2**: p. 77-84.
176. Tasi, C.-T., W.-K. Wang, S.-L. Ou, S.-Y. Huang, R.-H. Horng, and D.-S. Wuu, *Structural and Stress Properties of AlGaN Epilayers Grown on AlN-Nanopatterned Sapphire Templates by Hydride Vapor Phase Epitaxy.* Nanomaterials, 2018. **8**: p. 704.
177. Tasi, C.-T., W.-K. Wang, T.-Y. Tsai, S.-Y. Huang, R.-H. Horng, and D.-S. Wuu, *Reduction of Defects in AlGaN Grown on Nanoscale-Patterned Sapphire Substrates by Hydride Vapor Phase Epitaxy.* Materials (Basel, Switzerland), 2017. **10**(6): p. 605.
178. Gkanatsiou, A., C.B. Lioutas, N. Frangis, E. Polychroniadis, P. Prystawko, M. Leszczynski, T. Altantzis, and G. Tendeloo, *Influence of 4H-SiC substrate miscut on the epitaxy and microstructure of AlGaN/GaN heterostructures.* Materials Science in Semiconductor Processing, 2019. **91**: p. 159-166.
179. Hiscocks, J. and R. Hielscher, *Getting started with MTEX for EBSD analysis*. 2017.
180. Hull, D. and D.J. Bacon, *Chapter 9 - Dislocation Arrays and Crystal Boundaries*, in *Introduction to Dislocations (Fifth Edition)*, D. Hull and D.J. Bacon, Editors. 2011, Butterworth-Heinemann: Oxford. p. 171-204.
181. Niehle, M., J.-B. Rodriguez, L. Cerutti, E. Tournié, and A. Trampert, *The Interaction of Extended Defects as the Origin of Step Bunching in Epitaxial III–V Layers on*

Vicinal Si(001) Substrates. physica status solidi (RRL) – Rapid Research Letters, 2019. **13**(10): p. 1900290.
182. Weyher, J.L., *Characterization of wide-band-gap semiconductors (GaN, SiC) by defect-selective etching and complementary methods.* Superlattices and Microstructures, 2006. **40**(4): p. 279-288.
183. Shen, X.Q., H. Okumura, and H. Matsuhata, *Studies of the annihilation mechanism of threading dislocation in AlN films grown on vicinal sapphire (0001) substrates using transmission electron microscopy.* Applied Physics Letters, 2005. **87**(10): p. 101910.
184. Gradečak, S., P. Stadelmann, V. Wagner, and M. Ilegems, *Bending of dislocations in GaN during epitaxial lateral overgrowth.* Applied Physics Letters, 2004. **85**(20): p. 4648-4650.
185. Laurent, M.A., S. Keller, and U.K. Mishra, *Comprehensive Analysis of Surface Morphology and Growth Mode of AlInGaN Films.* physica status solidi (a), 2019. **216**(1): p. 1800523.
186. Smereka, P., *Spiral crystal growth.* Physica D: Nonlinear Phenomena, 2000. **138**(3): p. 282-301.
187. Winkelmann, A., C. Trager-Cowan, F. Sweeney, A.P. Day, and P. Parbrook, *Many-beam dynamical simulation of electron backscatter diffraction patterns.* Ultramicroscopy, 2007. **107**(4): p. 414-421.
188. Winkelmann, A., *Dynamical Simulation of Electron Backscatter Diffraction Patterns*, in *Electron Backscatter Diffraction in Materials Science*, A.J. Schwartz, et al., Editors. 2009, Springer US: Boston, MA. p. 21-33.
189. Bachmann, F., R. Hielscher, and H. Schaeben, *Texture Analysis with MTEX–Free and Open Source Software Toolbox.* Solid State Phenomena, 2010. **160**.
190. Wright, S.I., M.M. Nowell, and D.P. Field, *A Review of Strain Analysis Using Electron Backscatter Diffraction.* Microscopy and Microanalysis, 2011. **17**(3): p. 316-329.
191. Bryan, I., Z. Bryan, S. Mita, A. Rice, J. Tweedie, R. Collazo, and Z. Sitar, *Surface kinetics in AlN growth: A universal model for the control of surface morphology in III-nitrides.* Journal of Crystal Growth, 2016. **438**: p. 81.
192. Shen, X.-Q., K. Furuta, N. Nakamura, H. Matsuhata, M. Shimizu, and H. Okumura, *Quality improvement of III-nitride epilayers and their heterostructures grown on vicinal substrates by rf-MBE.* Journal of Crystal Growth - J CRYST GROWTH, 2007. **301**: p. 404-409.
193. Wright, S.I., M.M. Nowell, R. de Kloe, P. Camus, and T. Rampton, *Electron imaging with an EBSD detector.* Ultramicroscopy, 2015. **148**: p. 132-145.
194. Naresh-Kumar, G., A. Alasmari, G. Kusch, P.R. Edwards, R.W. Martin, K.P. Mingard, and C. Trager-Cowan, *Metrology of crystal defects through intensity variations in secondary electrons from the diffraction of primary electrons in a scanning electron microscope.* Ultramicroscopy, 2020. **213**: p. 112977.
195. Liu, H., L. Zhang, S. Chua, and D.Z. Chi, *Crystallographic tilt in GaN-on-Si (111) heterostructures grown by metal–organic chemical vapor deposition.* Journal of Materials Science, 2014. **49**.